

Computational Studies of Liquid Droplet on Liquid Infused Surfaces

Muhammad Subkhi Sadullah



Department of Physics
Durham University

*Thesis submitted in partial fulfilment of the requirements for the degree of
Doctor of Philosophy in Durham University*

· 2020 ·

Computational Studies of Liquid Droplet on Liquid Infused Surfaces

Muhammad Subkhi Sadullah

Department of Physics
Durham University

*Thesis submitted in partial fulfilment of the requirements for the degree of
Doctor of Philosophy in Durham University*

· 2020 ·

ABSTRACT

Surfaces that can repel any liquid are highly desired in various aspect of life for their wide range of beneficial applications. They can be utilised to enhance production processes, to simplify maintenance processes, to preserve surfaces from fouling, and many more. Ironically, one effective way to repel a liquid from a surface is by infusing the surface with another liquid which acts as a lubricant. Such surfaces are called liquid infused surfaces (LIS). The presence of the lubricant introduces rich interplay between the interfacial properties of the solid surface and the other fluid phases, which leads to many new interfacial phenomena.

We employ two numerical methods for studying the behaviour of a liquid droplet on a LIS. First, we use the lattice Boltzmann method, which is powerful for studying the dynamic evolution of the system. Second, we use the phase field energy minimisation method, which is efficient for finding the equilibrium states of the system. In this thesis, we show how these numerical methods can be exploited to explore a wide range of LIS parameters and to confirm our theoretical predictions.

We start by examining the equilibrium properties of the LIS system and demonstrate that the droplet morphology strongly depends on the choice of liquids used for the droplet-lubricant combination. The droplet morphology, in turn, affects the translational and rotational dynamics of the droplet under the influence of an external body force. Interestingly, we found a complex interplay between contact line pinning and viscous dissipation at the lubricant ridge, which become dominant at large and small apparent angles, respectively. Our investigations further demonstrate that the relative importance of viscous dissipation at the lubricant ridge depends on the drop to lubricant viscosity ratio, as well as on the shape of the wetting ridge.

Next, we demonstrate spontaneous bidirectional motion of droplets on liquid infused surfaces in the presence of a topographical gradient, in which the droplets can move either toward the denser or the sparser solid fraction area. We show that the key factor determining the direction of motion is the preferential wetting of the droplet on the solid surface and on the lubricant film, which depends on the choice of the droplet-lubricant combination.

Finally, we study how the pinning force of droplet on LIS is controlled by the solid surface fraction, the lubricant wetting angles, and the various fluid surface tensions. We derive an analytical prediction for contact angle hysteresis and numerically test the theory. We also discuss why a droplet on a liquid infused surface with partially wetting lubricants typically experiences stronger pinning compared to a droplet on a classical superhydrophobic surface.

CONTENTS

Acknowledgments	iv
Declaration	v
Contributions	vi
Publications	vii
1 Introduction	1
1.1 Surface Tension and Surface Free Energy	1
1.2 Wetting Phenomena	3
1.3 Three Fluid Phases System	5
1.4 Wetting and Roughness	7
1.4.1 Contact Angle Hysteresis	7
1.4.2 Wenzel and Cassie States	9
1.4.3 Wetting Gradient	11
1.5 Liquid Repellent Surfaces	12
1.6 Liquid Infused Surfaces	14
1.6.1 Origin and Important Features	14
1.6.2 Fabrication Method	16
1.6.3 Wetting States	17
1.6.4 Parameters of Liquid Infused Surfaces	19
1.7 Summary of the Thesis	21
2 Methods	23
2.1 Ternary Free Energy Model	23
2.1.1 Bulk Potential	24
2.1.2 Interface Potential	25
2.1.3 Wetting Potential	27
2.2 Lattice Boltzmann Method	31
2.2.1 Solving the Hydrodynamic Equations	31
2.2.2 Body Force	38
2.2.3 Cahn-Hilliard Equation	38
2.2.4 Boundary Conditions	39
2.3 The Phase Field Energy Minimisation Method	42
2.3.1 The Total Free Energy Calculation	42
2.3.2 Calculating the Gradient of the Total Free Energy	44
2.4 Benchmark	46
2.5 Discussion	49

3	Droplet Morphology and Droplet Mobility on Liquid Infused Surfaces	51
3.1	Simulation Setup	52
3.2	Droplet Morphologies in Mechanical Equilibrium	53
3.3	Droplet Mobility Under Influence of the Fluid Viscosities	58
3.4	Discussion	61
4	Translational and Rotational Dynamics of Droplets on Liquid Infused Surfaces	63
4.1	Translational Dynamics	64
4.2	Rotational Dynamics	71
4.3	Discussion	75
5	Bidirectional Motion of Droplets on Gradient Liquid Infused Surfaces	77
5.1	The Origin of the Driving Force	78
5.2	Small Meniscus Case	81
5.3	Demonstration of Bidirectional Motion Using Simulations and Experiments	83
5.3.1	Simulations	84
5.3.2	Experiments	85
5.3.3	Phase Diagram	89
5.3.4	The 2D Cases	90
5.4	Droplet Dynamics under Different Surface Textures	93
5.5	Potential Applications	95
5.6	Discussion	96
6	Factors Controlling the Pinning Force of Droplets on Liquid Infused Surfaces	98
6.1	Derivation of Pinning Force and Contact Angle Hysteresis	99
6.1.1	Depinning Mechanisms	101
6.1.2	The Advancing and the Receding Angles	104
6.2	The Effect of Changing Fluid and Solid Properties	105
6.3	The Relationship Between Contact Angle Hysteresis, Sliding Angle and Pinning Force	107
6.4	Discussion	110
7	Concluding Remarks	112
7.1	Conclusions	112
7.2	Further Development of the Simulation Methods	113
7.3	Open Questions and Project Outlook	114
7.3.1	Lubricant Depletion	114
7.3.2	Lubricant Dynamics	115
7.3.3	Applications of Liquid Infused Surfaces	116
7.4	Epilogue	119
	Bibliography	120

ACKNOWLEDGMENTS

First of all, I would like to thank my supervisor, Dr Halim Kusumaatmaja, for welcoming me to his research group, teaching me his knowledge, and guiding and motivating me throughout my PhD training. He has become my source of inspirations for becoming a good supervisor and a good scientist. I also would like to thank Dr Ciro Semprebon who has introduced me to the computational methods. He also provided me with many interesting discussions, whether or not related to our research. I also thank Dr Yonas Gizaw, Dr Kislou Voitchovsky, Prof. Suzanne Fielding and Prof. Colin Bain for providing me useful feedbacks in my research. I also thank Dr Aidan Hindmarch, Dr Budhika Mendis, Dr Richard Wilman, Dr Richard Wilson, Prof. Del Atkinson and Prof. Ifan Hughes for involving me in undergraduate teaching. I also thank the rest of the Soft Matter Community at Durham University, especially Jack Panter and Ethan Miller for sharing their views and aiding me in my research. Lastly, I would like to acknowledge Indonesia Endowment Fund for Education (LPDP) for supporting me with a scholarship to pursue a doctoral degree at Durham University.

On a personal note, I would like to thank residents of Keenan House, Indonesian society and Islamic society in Durham, Ustinov College and Durham University for making a wonderful and memorable UK life experience for me and my family. I also thank Mrs Lusi Widyastuti for helping me and looking after my family when they were in Italy. I will always be indebted. Also, I want to thank my family and relatives, especially my mother, father, brother, and sister for their love and constant support. I am sorry for being away from home for so long. May they always be healthy.

I sincerely apologise to my children, Alice and Isa, who were born during my PhD. I am sorry for the time I lost, the attentions I could not give, and the moments I missed. Daddy always loves you. I pray that you will always be healthy, strong, blessed and happy. I also hope you will achieve your dreams and goals in the future. And finally, a great special thanks to my wife, Khusna Amalia, for everything. I will not be able to achieve all of these if you were not by my side. Thank you . . .

DECLARATION

The work presented in this thesis has been developed by the author under the supervision of Dr Halim Kusumaatmaja of the Department of Physics at Durham University. All text and figures are the work of the author unless otherwise stated.

A part of Fig. 5.6 in this thesis has been presented for a Level 4 Project submitted by Jayne Parle, co-supervised by Dr Halim Kusumaatmaja and I, for the qualification of MPhys at Durham University. The specific contributions of other researchers are detailed in the next section.

Copyright © 2020 Muhammad Subkhi Sadullah

The copyright of this thesis rests with the author. No quotation from it should be published without the author's prior written consent and information derived from it should be acknowledged.

CONTRIBUTIONS

The work presented in this thesis has been developed by the author under the supervision of Dr Halim Kusumaatmaja of the Department of Physics at Durham University. The work presented in Chapter 5 is a collaborative work between our group and an experimentalist group led by Dr Gary Wells of the Northumbria University. The author led the work by developing the main theory and perform the numerical confirmation of the theory. Our collaborators then worked on the experimental confirmation of the theory.

- Figure 5.1. Gaby Launay performed the droplet motion experiments.
- Figure 5.4. Gaby Launay performed the sample imaging using Scanning Electron Microscope and created the figure.
- Figure 5.5. Gaby Launay performed the data collection for the figure.
- Table 5.1. Gaby Launay performed the droplet motion experiments.
- Figure 5.6. Gaby Launay collected the experimental data points. Jayne Parle collected the 2-D simulation data points. The author collected the full 3-D and the quasi 3-D simulation data points and then constructed the phase diagram.

PUBLICATIONS

Most of the work presented in Chapter 3, 4, 5, 6 have been submitted for journal articles:

- M. S. Sadullah, C. Semperebon, and H. Kusumaatmaja, “Drop Dynamics on Liquid-Infused Surfaces: The Role of the Lubricant Ridge”, *Langmuir* **34**, 8112–8118 (2018).
- M. S. Sadullah, G. Launay, J. Parle, R. Ledesma-Aguilar, Y. Gizaw, G. McHale, G. G. Wells, and H. Kusumaatmaja “Bidirectional motion of droplets on gradient liquid infused surfaces”, *Commun. Phys* **3**, 116, (2020).
- M. S. Sadullah, J. R. Panter, and H. Kusumaatmaja, “Factors controlling the pinning force of liquid droplets on liquid infused surfaces”, *Soft Matter* **16**, 8114–8121, (2020).

I also have been involved in the following publications:

- M. A. Gondal, M. S. Sadullah, T. F. Qahtan, M. A. Dastageer, U. Baig, and G. H. McKinley, “Fabrication and Wettability Study of WO₃ Coated Photocatalytic Membrane for Oil-Water Separation: A Comparative Study with ZnO Coated Membrane”, *Sci. Rep.* **7**, 1686 (2017).
- G. Launay, M. S. Sadullah, G. McHale, R. Ledesma-Aguilar, H. Kusumaatmaja, and G. G. Wells, “Self-Propelled Droplet Transport on Shaped-Liquid Surfaces”, *Sci. Rep.* **10**, 14987 (2020).

CHAPTER 1

Introduction

1.1 Surface Tension and Surface Free Energy

When a faucet is carefully opened, the shape of a small water droplet dripping out of it is almost perfectly spherical. The same phenomenon is present in a floating soap bubble, whose shape is also spherical. The governing physics in these phenomena is the tension at the surface of the liquid called surface tension (it has the dimension of force per unit length, N/m). Surface tension manifests because the molecules at the surface are surrounded by fewer molecules compared to the molecules in the bulk of the liquid [1], as illustrated in Fig. 1.1. Since the cohesive force at the surface is shared with fewer molecules, the intermolecular attraction at the surface is stronger. This strong interaction between the surface molecules creates tension at the surface of the liquid. The surface tension also makes the surface of the liquid behaves like an elastic film which can support a small weight [1].

The direction of the force due to surface tension is tangent to the surface. In the absence of confinement, the net force due to the surface tension is to the inside of the liquid body [1]. Consequently, liquid droplets form spherical shape when at rest and under no influence of any external force. The molecule at the surface is also attracted to the inside of the liquid due to imbalance intermolecular interaction so that the surface is minimised. This attraction is balanced by short-range repulsive forces due to the compression resistance which maintains the volume of the liquid [1].

It is also useful to describe this phenomenon in terms of surface free energy, defined as energy per unit area (J/m^2), which is dimensionally equivalent to surface tension. Surface free energy is the excess of binding energy since the molecules at the surface interact with fewer

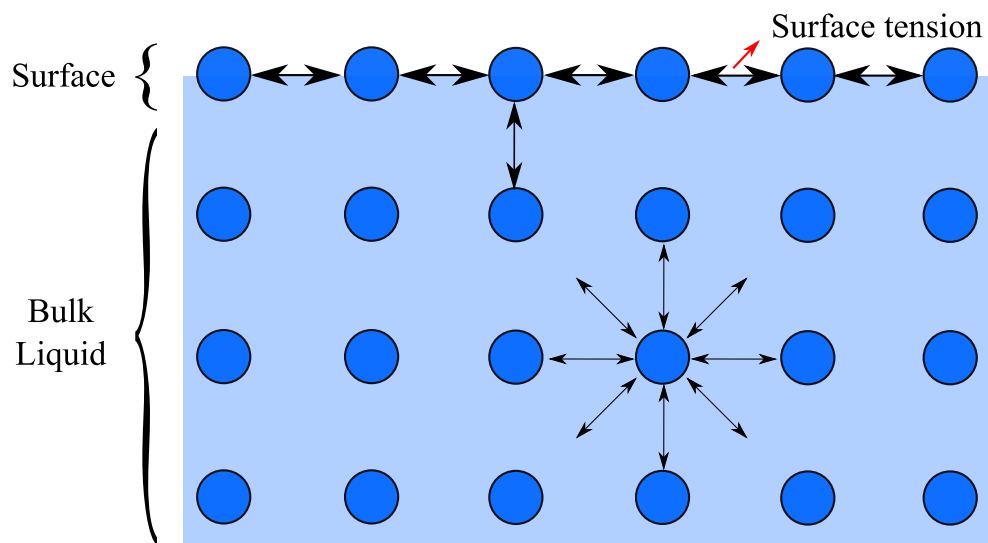


Figure 1.1: Molecules at the surface of the liquid are surrounded by fewer molecules, resulting in the stronger intermolecular attraction between the molecules at the surface. This strong attraction manifests as surface tension.

molecules than the inner molecules [1]. The total free energy of the system is the surface free energy integrated over the surface area. To achieve equilibrium, the droplet evolves into a spherical shape to minimise its total free energy [1].

Surface tension and surface free energy are technically the same quantity under two different point of views, mechanics and thermodynamics. When discussing the force due to surface tension, the surface tension is to be integrated over the contact line to obtain capillary force. Whereas when discussing surface thermodynamics, the surface free energy is integrated over the surface area to obtain the total free energy.

Surface energy is also present in the solid phase and has a similar origin to the liquid phase. Here it is useful to consider the surface energy as the energy required to create a unit of surface area. One way to create a surface is by cutting a bulk solid into two. Using this example, we can see that the energy required to make a surface from metal is higher than that of from a wax. This is why metallic substances have larger surface energy compared to other solids. The solid phase cannot change its shape to minimise the total free energy since the constituting molecules or atoms are densely packed. However, the total energy can be minimised by having an interface with other substances, for example with a liquid phase. The phenomenon where a liquid phase spreads on a solid surface to minimise the total free energy is called wetting [1].

1.2 Wetting Phenomena

When a droplet of liquid is in contact with a solid surface, the liquid droplet will spread on the solid surface if it can decrease the total free energy of the system [1], which is given by

$$E_{tot} = \gamma_{sg}A_{sg} + \gamma_{sl}A_{sl} + \gamma_{lg}A_{lg}, \quad (1.1)$$

where subscripts sg , sl , lg indicate solid-gas, solid-liquid, and liquid-gas interface respectively, while γ and A are their corresponding surface free energy and total interfacial area respectively. For the case when γ_{sg} is sufficiently high such that $\gamma_{sg} > \gamma_{sl} + \gamma_{lg}$, the solid will make an interface with the liquid as much as possible to decrease A_{sg} . Hence, the liquid droplet spreads completely on the solid surface. This case is called perfect wetting. An example of this case is a droplet of methanol on a clean glass slide. Inversely, when $\gamma_{sg} < \gamma_{sl} + \gamma_{lg}$, the droplet will remain spherical to minimise A_{sl} and A_{lg} . This case is called perfect non-wetting. An example of this case can be seen in almost all metallic liquid on a non-metallic surface. Most of the time, the wetting situation for a flat smooth surface is between these two extreme cases, which is called partial wetting.

Quantifying and controlling wettability are important for a wide range of applications. For instance, in oil industries, surfactants that can reduce oil wettability to the rock formation is of interest for enhanced oil recovery (EOR) because this can increase the efficiency of the extraction process [2,3]. In agriculture, an effective pesticide needs to have a composition that wets the surface of the leaf [4]. In the manufacturing industry, the product packaging that is non-wettable by the liquid product can minimise the product leftover, which is beneficial for consumers [5].

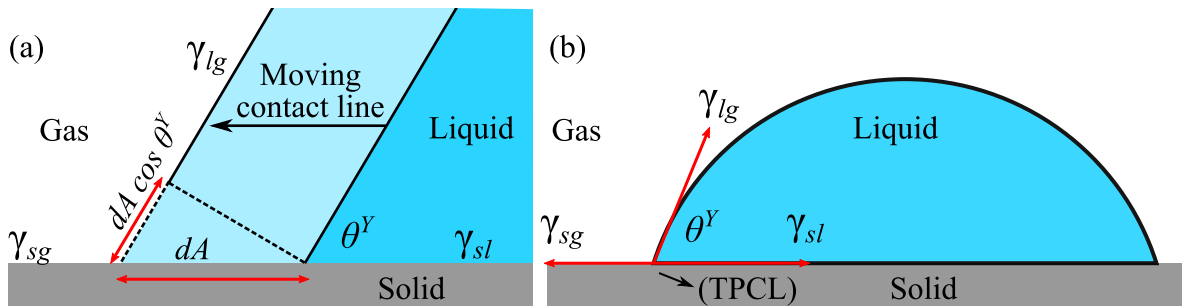


Figure 1.2: Two views of Young's contact angle θ^Y . (a) Energy point of view sees θ^Y as the angle formed when the total energy is minimised. (b) Force point of view sees θ^Y as the angle when the surface tension force is balanced. The two views are equivalent.

The wettability of a liquid on a solid surface is often quantified by means of the contact angle θ^Y of a liquid droplet on a solid surface at equilibrium. The contact angle is measured at the point where the three interfaces meet, often called the three-phase-contact-line (TPCL) [1], as illustrated in Fig. 1.2. The contact angle can be viewed in two ways. From the point of view of the energy of the system, as illustrated in Fig. 1.2(a), it corresponds to the angle formed when the total free energy is minimised. This can be understood by evaluating the energy change dE when the contact line is moved by a unit of surface area dA , which is given by $dE = \gamma_{sl}dA - \gamma_{sg}dA + \gamma_{lg}dA \cos\theta^Y$ [1, 6]. Then, the total free energy is minimised when $dE/dA = 0$. From the point of view of force balance, as shown in Fig. 1.2(b), the contact angle represents the angle formed when the surface tension force at the TPCL is balanced parallel to the surface, such that $\gamma_{lg} \cos\theta^Y + \gamma_{sl} - \gamma_{sg} = 0$ [1, 6]. Both views lead to the Young's contact angle equation [7],

$$\cos\theta^Y = \frac{\gamma_{sg} - \gamma_{sl}}{\gamma_{lg}}. \quad (1.2)$$

From Eq. (1.2) we notice that the contact angle does not depend on the volume of the droplet. However, in experiment, we can see that two droplets of the same liquid can have different shapes depending on their volumes, even when the surface is perfectly smooth and homogenous. There are two reasons for such variation in shapes. Firstly, if the volume is large enough, the droplet shape will be sagged (for pendant droplet) or flatten (for sessile droplet). However, the contact angle at the TPCL remains the same. This is because the effect of gravity becomes more apparent as the droplet volume is bigger. By comparing the force due to surface tension, $R\gamma_{la}$, and the force due to gravity, $R^3\rho g$, where R and g are the length scale of the liquid droplet and the gravitational acceleration, we can obtain a characteristic length l_c called the capillary length, which is defined as $l_c = \sqrt{\gamma_{lg}/(\rho g)}$ [1]. Gravity becomes dominant if $R > l_c$. For water, l_c is around 2.7 mm. In this thesis, we concentrate on cases where gravity does not play a major role. In real life, this corresponds to cases with length scale below l_c where the assumption is valid. In nature, an example where surface tension dominates gravity can be seen in trees where they absorb water from underground and transport it up to the leaves where the photosynthesis takes place. This process is possible because the diameter of the plant transport vessel is smaller than l_c so that the pulling force due to surface tension is dominant compared to gravity.

Secondly, while the contact angle at the TPCL at macroscopic scale remains constant, this is not the case for ultrasmall droplets where the contact angle appears larger or smaller than what is predicted by Young's equation. This effect is caused by line tension, which is an additional free energy component from the molecules near the TPCL [8]. The origin of the line tension is similar to the origin of the surface tension. In this case, the molecules at the TPCL are surrounded by even fewer molecules compared to the molecules at the interface. The effect of the line tension becomes stronger as the droplet becomes smaller. By considering the contribution from the line tension, the Young's equation can be written as [8]

$$\cos \theta(R_B) = \cos \theta^Y - \frac{\gamma_{slg}}{R_B \gamma_{lg}}, \quad (1.3)$$

where γ_{slg} and R_B are the line tension and the droplet base radius respectively. The estimated magnitude of γ_{slg} is in the order of $10^{-12} - 10^{-10}$ N [9]. Thus, the effect of line tension becomes apparent when R_B is in the order smaller than 100 nm. Numerous articles in the literature suggest that γ_{slg} can be either negative (< 0) or positive (> 0) [9]. As such, the effect of the line tension can either increase or decrease the contact angle compared to the Young's angle in Eq. (1.2).

1.3 Three Fluid Phases System

The wetting system does not necessarily have to happen in a dry environment. The liquid droplet can also be found on a solid surface while surrounded by another liquid that is immiscible to the droplet, such as oil droplet in water as illustrated in Fig. 1.3. This case is quite common in nature, such as crude oil trapped in a rock formation and lubricating oil layer on the skin of some marine fishes [10, 11]. This situation is also relevant in many industrial applications, such as oil removal from textile or other hard surfaces by washing process [12], or oil removal from wastewater [13, 14]. In this case, the contact angle is given by $\cos \theta_{ow} = (\gamma_{sw} - \gamma_{so})/\gamma_{ow}$, where the subscripts w and o represent the water and oil phases respectively. This equation can also be written as

$$\gamma_{ow} \cos \theta_{ow} = \gamma_{sw} - \gamma_{so}. \quad (1.4)$$

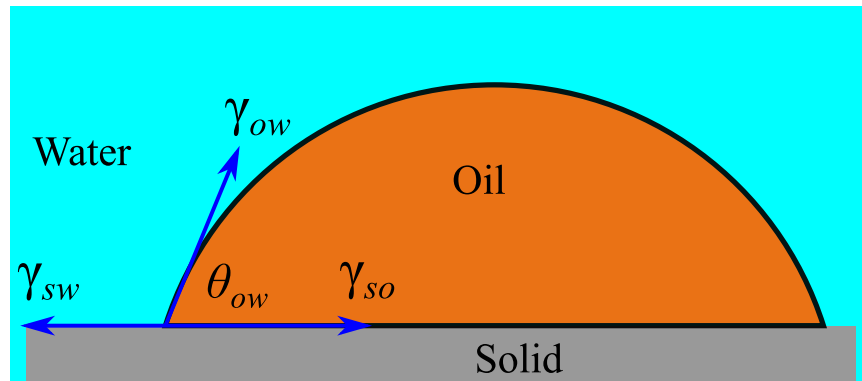


Figure 1.3: Illustration of an oil droplet sticking on a solid surface in the water environment.

As suggested in Eq. (1.4), the difference between surface energies when in two different fluids can be measured via contact angle. However, the solid surface energy γ_{sx} , where x is any fluid phase, is difficult to measure. Alternatively, we can use the definition of the contact angle of a liquid (surrounded by air) on solid using Eq. (1.2) to obtain

$$\gamma_{sw} = \gamma_{sa} - \gamma_{wa} \cos \theta_{wa}, \quad (1.5)$$

for solid-water surface tension, and

$$\gamma_{so} = \gamma_{sa} - \gamma_{oa} \cos \theta_{oa}, \quad (1.6)$$

for solid-oil surface tension. The subscript a represents the air phase. By substituting Eqs. (1.5) and (1.6) to Eq. (1.4), we obtain

$$\gamma_{wa} \cos \theta_{wa} + \gamma_{ao} \cos \theta_{ao} + \gamma_{ow} \cos \theta_{ow} = 0. \quad (1.7)$$

This equation is called the Girifalco-Good relation [15], which allows us to determine the contact angle of three fluid phases system when two out of three contact angles θ_{wa}, θ_{oa} or θ_{ow} are known. The Girifalco-Good relation is also an important thermodynamic consistency relation that we have to satisfy in our modelling approach (Chapter 2).

Another important concept when studying three fluid phase system is illustrated in Fig. 1.4, where a liquid droplet is floating on an immiscible liquid bath to form a liquid lens. Unlike the solid surface, the surface morphology of the liquid bath is elastic and can deform in the presence of an external force. In this case, the TPCL is the meeting point of the water-air,

oil-water and oil-air interfaces. At equilibrium, the forces from the interfacial tensions are balanced. Using geometrical analysis we can find the relation between the interfacial tensions and the angles that are formed between any two interfaces as the following [1]

$$\frac{\gamma_{oa}}{\sin \theta_w} = \frac{\gamma_{ow}}{\sin \theta_a} = \frac{\gamma_{wa}}{\sin \theta_o}. \quad (1.8)$$

These angles are called the Neumann's angles of three fluid phases. We can see that the morphology of the liquid lens is determined by the magnitude of the interfacial tensions.

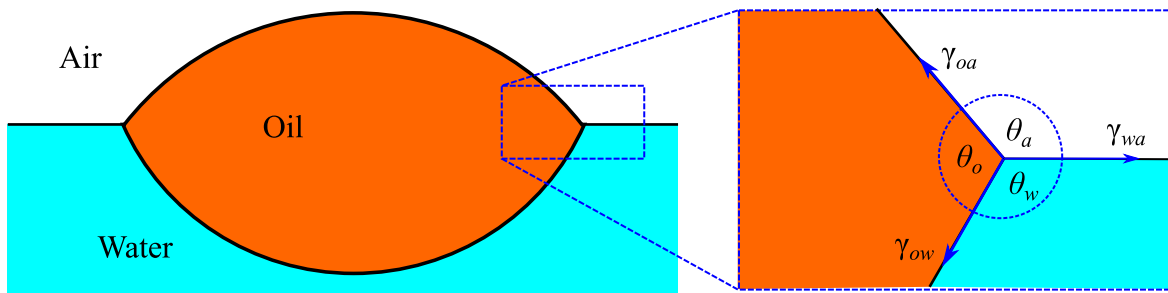


Figure 1.4: Oil droplet on a water bath creates a liquid lens. At equilibrium, the angles formed are determined by the balance of the interfacial tensions.

1.4 Wetting and Roughness

1.4.1 Contact Angle Hysteresis

The Young's contact angle formulation is obtained using the assumption that the solid surface is perfectly flat [7]. However, such surface is rare to occur in daily practice. For many reasons, the presence of roughness on the solid surface is inevitable [16]. Two important consequences of surface roughness are contact line pinning and contact angle hysteresis. Consider a model surface inhomogeneity as two connected planes as illustrated in Fig. 1.5. Based on the surface tensions of the system, the system has Young's contact angle θ^Y . If the TPCL is located on the flat part of the surface (case 1), the apparent contact angle θ_{app} is equal to the Young's angle, θ^Y . However, the apparent contact angle is different if the TPCL is located on the tilted part of the surface (case 2). In this case, the apparent angle is $\theta^Y + \phi$. Moreover, if the TPCL is at the edge (case 3), the apparent contact angle can be at any value between θ^Y and $\theta^Y + \phi$ [16]. As a result, the contact angle for most surfaces may be observed at various values, even if the same liquid and the same solid sample are used.

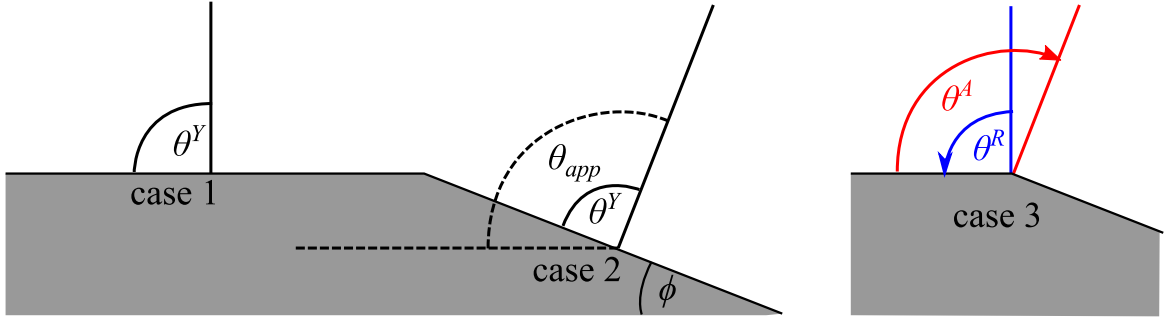


Figure 1.5: Due to surface inhomogeneity, the apparent contact angle θ_{app} of a liquid droplet can be different depending on the location of the TPCL [16].

One can consider a thought experiment where one carefully increases the droplet volume and record the increase of the contact angle and observe where the contact line is pinned. At a certain value of contact angle, the contact line starts to advance. This maximum contact angle is called the advancing contact angle, θ^A . In the example shown in Fig. 1.5, this happens when the contact line is at the edge and the increase of the contact angle no longer satisfies Young's contact angle. Hence, the contact line advances.

Similarly, when the droplet volume is reduced, the contact line may not immediately recede as the contact angle decreases. Once the contact angle reaches the minimum value, the contact line begins to recede. This minimum contact angle is called the receding contact angle θ^R . For some surfaces, the difference between θ^A and θ^R values is negligible. For some others, the difference can be extremely large. For this reason, some researchers argue that the observed contact angle θ_{app} cannot be used to quantify the wettability of a surface unless the θ^A and θ^R are also reported.

The difference between θ^A and θ^R is called the contact angle hysteresis (CAH), $\Delta\theta = \theta^A - \theta^R$. The cosine of the two angles, $\Delta \cos \theta = \cos \theta^R - \cos \theta^A$, is directly related to the resisting force when a liquid droplet is about to move on a surface [16]. The droplet front contact line will not move until it reaches θ^A . At the same time, the rear contact line is not moving until it reaches θ^R . The corresponding resisting force is called the pinning force, where per unit length, it is defined as [16, 17]

$$f_{pinning} = \gamma(\cos \theta^R - \cos \theta^A), \quad (1.9)$$

where γ is the fluid surface tension. For many applications, such as liquid repellent surfaces, CAH is desired to be as low as possible so that liquid can be eliminated from the surface using a small perturbation.

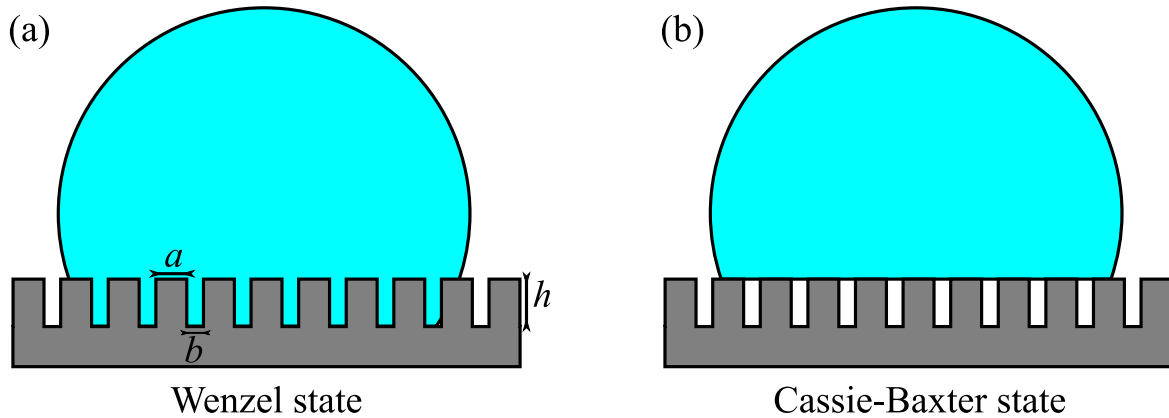


Figure 1.6: Two possible wetting states as the result of surface roughness. (a) At Wenzel state, the liquid is exploring the surface roughness such that the real solid surface area in contact with the liquid is larger than the apparent surface area. a , b , and h are the post width, spacing and height respectively. (b) At Cassie state, the liquid droplet is suspended on the surface roughness and has a smaller contact area with the solid surface.

The pinning-depinning phenomenon and CAH have been studied extensively in the literature [18–20]. In general, it is concluded that the simple thermodynamic argument is often insufficient for many cases since this does not incorporate the geometrical factor and the metastable states [21]. Systematic studies reveal that pinning-depinning mechanism is sensitive to the details of the surface patterning [22]. The contact line pinning is also associated with stick-jump-slip motion when the droplet volume is decreased or increased [23]. In addition, the hysteresis does not grow monotonically with the number of pinning points [24, 25]. Therefore, a careful study is needed when assessing the contact angle hysteresis.

1.4.2 Wenzel and Cassie States

Surface roughness is also associated with two possible wetting states, the collapsed and the suspended state. These wetting states are also known as the Wenzel and the Cassie states respectively. In the Wenzel state (Fig. 1.6(a)), the liquid droplet imbibes the surface roughness such that the real solid-liquid interfacial area is larger than the apparent or projected area [16, 26]. We can introduce a roughness parameter r as a ratio of the real surface area to the projected surface area. For substrate of square posts with post width a , post spacing b , and height h , r can be calculated as

$$r = \frac{\text{real solid surface area}}{\text{projected surface area}} = \frac{(a+b)^2 + 4ah}{(a+b)^2}. \quad (1.10)$$

The effective solid-air and solid-liquid surface tensions then can be written as $r\gamma_{sg}$ and $r\gamma_{sl}$. Plugging in these expressions to Eq. (1.2), we obtain

$$\cos \theta^W = \frac{r\gamma_{sg} - r\gamma_{sl}}{\gamma_{lg}} = r \cos \theta^Y. \quad (1.11)$$

The value of r is always larger than unity because the real surface area is larger than the projected surface area. From Eq. (1.11), we can see that the surface roughness increases the observed contact angle if θ^Y is larger than 90° , and decreases the observed contact angle if θ^Y is smaller than 90° . The Wenzel state is characterised by a large CAH since the liquid droplet is trapped by the surface roughness. An example of this state is a water droplet on a rose petal [27].

In the second wetting state, the Cassie-Baxter state (Fig. 1.6(b)), the liquid droplet is assumed to be sitting on top of the surface roughness such that only a fraction of solid is actually in contact with the liquid [16, 28]. Using this assumption, the surface can be approximated as a composite of solid and air, where the liquid occupy φ_s fraction of the total solid surface area. For square posts as in Fig. 1.6(b), φ_s is defined as

$$\varphi_s = \frac{\text{solid surface in contact with liquid}}{\text{projected surface area}} = \frac{a^2}{(a+b)^2}. \quad (1.12)$$

The effective solid-air and solid-liquid surface tensions then can be written as

$$\gamma_{sg}^{eff} = \varphi_s \gamma_{sg} + (1 - \varphi_s) \gamma_{gg} \quad \text{and} \quad \gamma_{sl}^{eff} = \varphi_s \gamma_{sl} + (1 - \varphi_s) \gamma_{lg} \quad (1.13)$$

respectively. Here, γ_{gg} is the surface tension of the gas-gas interface, which is 0. Substituting these expressions to Eq. (1.2), we obtain

$$\cos \theta^{CB} = \frac{\gamma_{sg}^{eff} - \gamma_{sl}^{eff}}{\gamma_{lg}} = \frac{\varphi_s \gamma_{sg} - (\varphi_s \gamma_{sl} + (1 - \varphi_s) \gamma_{lg})}{\gamma_{lg}}, \quad (1.14)$$

$$= \varphi_s \cos \theta^Y - (1 - \varphi_s). \quad (1.15)$$

Since in this Cassie-Baxter state the effect of roughness reduces the effective solid-air and solid-liquid surface tensions, the observed angle appears to be larger. Also, since the bottom of the liquid droplet is only partially in contact with solid, the Cassie-Baxter state is characterised by its low CAH. An example of this wetting state is a water droplet on a lotus leaf [29]. A

water droplet on a lotus leaf is very mobile and exhibits a very large contact angle, as if the leaf is non-wettable by water.

1.4.3 Wetting Gradient

In principle, one can vary the geometry of the post in one direction to create a topographical gradient. For example, the post width in the x -direction can be increased such that the value of φ_s increases with x . If the droplet is in the Cassie state, the contact angle of a liquid droplet placed on lower x will be higher than when placed on higher x . The effect of such wetting gradient allows a liquid droplet to self-transport from the high contact angle part to the low contact angle part of the substrate.

Various examples of surface structures which create wetting gradient can be found in nature. The silk fibres of the cribellate spiders consist of spindle-knots and joints of different roughness, which allow the web to collect water from humid air [30]. Cactus barbs have both conical shape and surface roughness gradient to help the plant collect water from fog and transport it to the absorbing organ [31].

The effect of wetting gradient has been extensively studied and implemented for various applications including liquid transport [32], inkjet printing [33] and water harvesting [34]. For example, Fig. 1.7 shows a man-made example of wetting gradient achieved by varying the solid fraction φ_s in one direction [35]. The driving force due to this wetting gradient propels the droplet to move towards higher φ_s area. In addition, it is worth noting that wetting gradients can be created not just by textural variations, but also via chemical treatments.

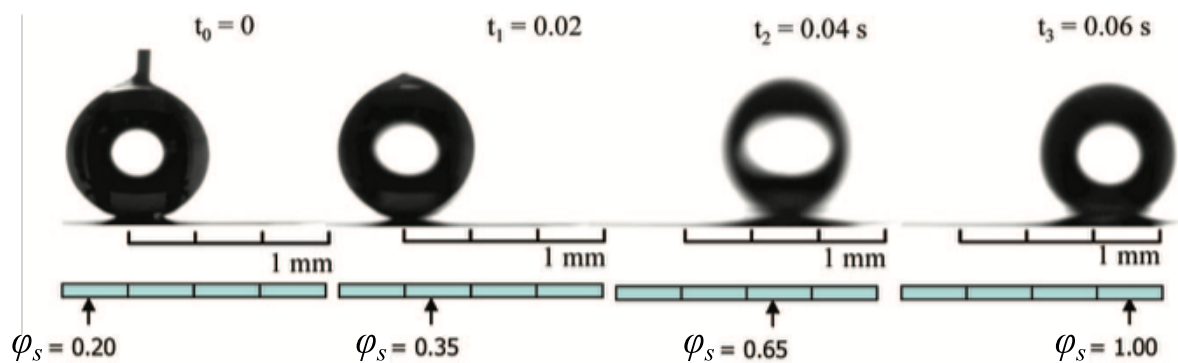


Figure 1.7: Droplet motion due to topographical gradient. The droplet moves from low φ_s toward higher φ_s area [35].

1.5 Liquid Repellent Surfaces

Surfaces which possess the ability to repel liquid are termed as liquid repellent surfaces. An example of naturally occurred liquid repellent surfaces is the lotus leaf [29, 36]. One exciting feature of the lotus leaf is that it always appears clean and dry because water cannot wet the surface of the leaf. Instead, water droplet collects dirt as it rolls on the surface of the leaf. This self-cleaning effect has inspired many applications. For example, it can be used to simplify the cleaning process for dust or dirt related fouling for photovoltaic cells [37], to protect electronic devices from water damage [38], to increase the efficiency of the water circulation system [39], and to preserve metallic surfaces from corrosion [40].

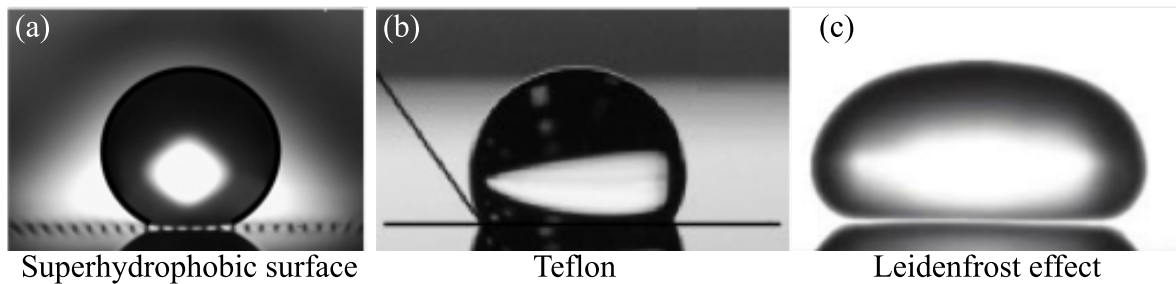


Figure 1.8: Droplet shapes on liquid repellent surfaces observed using a goniometer: (a) A droplet on superhydrophobic surface. The air pockets underneath the droplet are visible [41]. (b) A droplet on a hydrophobic surface obtained from Teflon coating which demonstrates a relatively high contact angle [42]. (c) Levitating droplet on a metallic surface exhibiting the Leidenfrost effect [43].

Fig. 1.8 shows examples of liquid repellent surfaces. Liquid repellent surfaces based on the lotus effect are often called superhydrophobic surfaces (Fig. 1.8(a)). They are characterised by high contact angle ($\theta \geq 150^\circ$) and low CAH ($\Delta\theta < 5^\circ$). To fabricate superhydrophobic surfaces, there are two ingredients: low surface energy, and surface roughness [44]. These can be achieved either by texturing the surface of low surface energy materials or by lowering the surface energy of rough surfaces. The fabrication methods can be as simple as burning glass slide using candle soot [45]. The most widely used method is spray deposition of nanoparticle suspensions [46]. The latter method can be used to cover a large area in relatively little time. Advanced fabrication methods such as photolithography, 3D printing, and chemical etching are also utilised to achieve extremely ordered nanostructures, which is useful for studying the effect of a certain parameter in a more systematic and cleaner way [47–49].

When very high contact angle and facile droplet mobility are not required, one can use low surface energy materials to reduce the surface adherence of liquid. An example of this type of

material is a fluorinated polymer called polytetrafluoroethylene (PTFE), which is also known as Teflon Fig. 1.8(b) [50]. PTFE has been widely used for sealing tape in the water circulation system. Furthermore, due to its durability against high temperature, this material serves as the main agent in the non-sticking pan. Although PTFE is good enough for preventing liquids to stick to its surface, the repellency is nowhere near that of a lotus leaf. Therefore, standalone PTFE cannot be used for applications which require high liquid repellency.

Liquid repellency can also happen when a droplet of liquid is in contact with solid whose temperature is larger than the boiling point of the liquid. Upon contact, an insulating film of vapour is formed which allows the liquid droplet to levitate above the hot solid, as shown in Fig. 1.8(c). This phenomenon is called the Leidenfrost effect [43]. The corresponding temperature at which vapour film is formed is called the Leidenfrost temperature T_L . For water, T_L is about 150°C [43]. The presence of the insulating vapour film makes the droplet highly mobile such that small perturbations are enough to cause a frictionless motion [43]. Interestingly, by introducing asymmetric texture at the solid surface, one can create a device to self-propel a liquid droplet into a certain direction [51].

Such Leidenfrost device is quite robust to sustain mechanical damage since its working principle mainly relies on the formation of the insulating vapour and it is insensitive to surface texturing [43]. In fact, hard materials such as metals and glass are often used to exploit the Leidenfrost effect for their excellent thermal conductivity. However, the Leidenfrost device is limited, due to the need for continuous energy supply to maintain the surface temperature above T_L . In addition, T_L can be quite high so that more care is required when working with the device. This effect is ideally applied in applications which constantly produce high heat. For example, in food preparation devices, the Leidenfrost effect could be used to protect the heating element from fouling. Droplet motion due to Leidenfrost effect could also be utilised to mobilise a rotor to generate electricity [52].

Among the types of liquid repellent surfaces mentioned above, Teflon is the only type that has penetrated the market widely and is commercially available. Superhydrophobic surfaces, on the other hand, still have very limited applications. One of the limitations of superhydrophobic surfaces is that they usually only repel water, as suggested by the name. This is because the liquid droplets on the superhydrophobic surfaces are in the Cassie-Baxter state, which is easy for water but difficult for most liquids due to their surface tensions. In particular, the droplets can undergo a wetting transition to the Wenzel state [53]. Once this happens, the

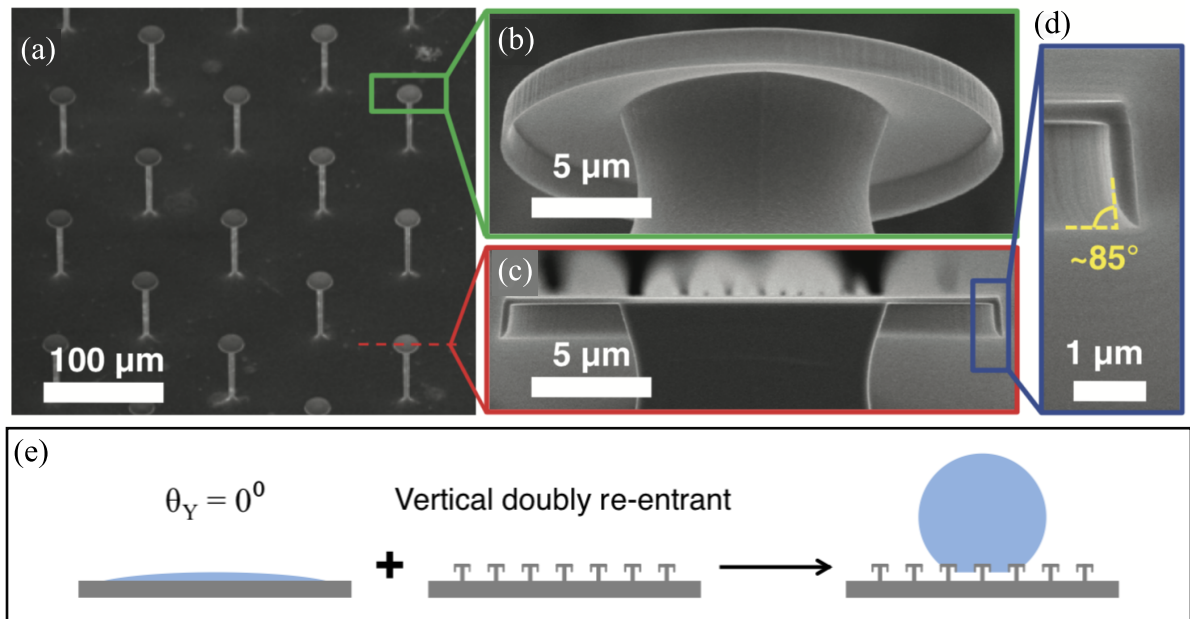


Figure 1.9: (a-d) Scanning electron micrographs of a textured surface with reentrant geometries. (e) The reentrant geometry significantly increases the energy barrier which prevent the droplet to collapse into the surface porosity, event for a complete wetting fluid [48].

surface will lose its advantageous properties. This wetting transition is likely to occur since the energy barrier is relatively low for simple geometries. Reentrant geometries, as shown in Fig. 1.9, are often incorporated to increase the energy barrier so that superhydrophobic surfaces are less susceptible to wetting transition and hence maintain their water repellency [54]. These reentrant geometries have been reported to increase the repellency such that not only it can repel water but also some oils [48], which is not possible for simple superhydrophobic surfaces because of the oils' low surface tensions. However, fabricating such textures requires an advanced lithographic method, which is extremely costly, and prevents large scale fabrication of such surfaces [47].

1.6 Liquid Infused Surfaces

1.6.1 Origin and Important Features

As discussed above, for many applications, liquid repellent surfaces are desired to not only be able to repel water but also other liquids such as alcohols or hydrocarbons. Complex surface texturing such as reentrant geometries can help to increase the liquid repellency (Fig. 1.9).

Another solution to prevent the liquid droplet from collapsing into the porosity is to imbibe the surface roughness with a lubricating liquid that is immiscible with the liquid that needs

to be repelled [55,56], as illustrated in Fig. 1.10. This type of surface is called Liquid Infused Surfaces (LIS) [57]. This type of surface is also known as SLIPS which stand for Slippery Lubricant Infused Porous Surfaces [58].

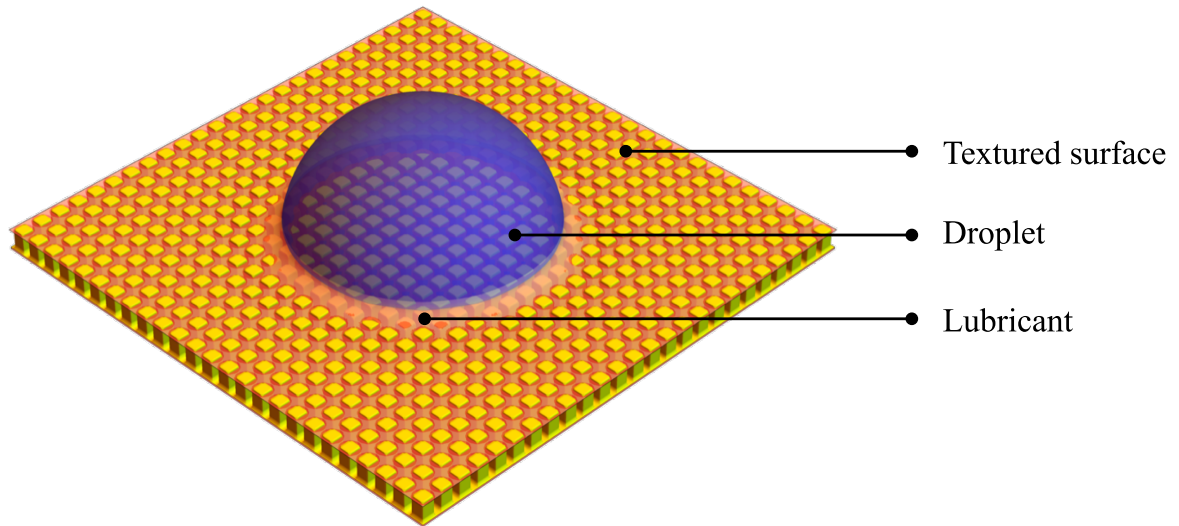


Figure 1.10: Illustration of a droplet on a textured surface infused with lubricant. This composite surface is termed as liquid infused surface (LIS).

The inspiration for LIS comes from carnivorous plants called the pitcher plants [59]. These plants have a specialised leaf used as an insect trap as shown in Fig. 1.11(a). These plants use nectar to attract insects and small animals and use the slippery surface of the peristome (the mouth of the trap) to make the prey fall into the trap. The secret of the slipperiness of the peristome is the hydrophilic (water-loving) textured surface (Fig. 1.11(b)), which allows it to maintain water from the rain. The presence of water at the peristome makes insects to slip and fall into the trap [59].

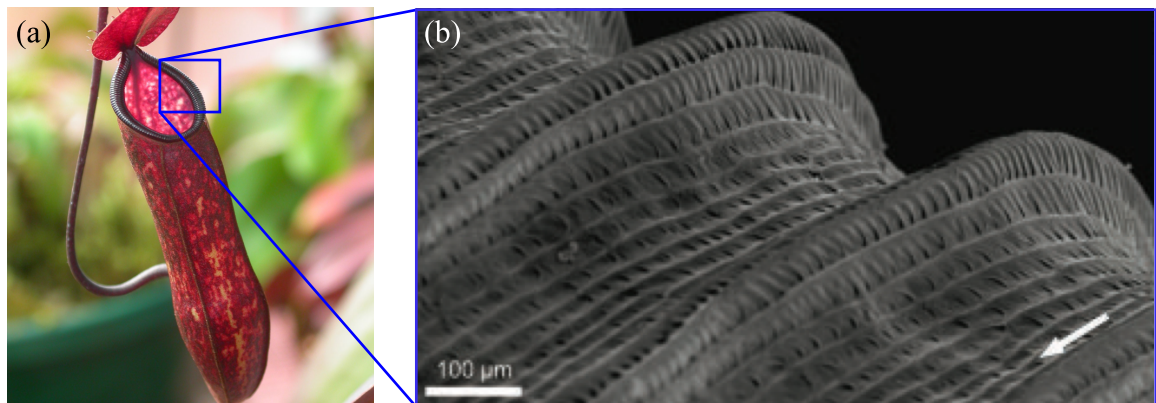


Figure 1.11: (a) The trap organ of pitcher plants. The blue square highlight the peristome. (b) The micrograph of the peristome reveals its microtexture [59].

LIS have many interesting features which make this type of surfaces superior compared to other types of liquid repellent surfaces. As long as the lubricant is immiscible to the droplet and the lubricant has a stronger affinity towards solid surface compared to the droplet, LIS can repel any liquid regardless of its surface tension [58]. In certain conditions, the pinning force is very small. As such, a liquid droplet placed on LIS moves very easily under small perturbations and it will shed away at a small tilting angle [58,60]. Moreover, these surfaces can also be designed to withstand high pressure and self-heal from physical damages [58], which distinguish them from other liquid repellent surfaces such as superhydrophobic surfaces. These advantageous features have given rise to many potential industrial applications, such as to reduce energy consumption in fluid transports [39], to simplify cleaning and maintenance processes [61], to prevent damage due to fouling [62], and to annihilate product leftover for smart liquid packaging.

1.6.2 Fabrication Method

The primary requirements for fabricating LIS are a rough solid substrate and a lubricating liquid which wets the solid but is immiscible to the droplet [63]. These requirements can be achieved using various materials and methods. One simple method is by infusing a lubricant to a commercially available Teflon microfibre filtration sheet (Fig. 1.12.(a)) [58].

Another approach is to use the inverse opal method which is done by depositing a dispersion of polystyrene microbeads and silica nanoparticles onto a glass substrate [64]. The sample is then heated in a furnace so that the polystyrene microbeads are removed while the silica nanoparticles are sintered, creating a sponge-like structure (Fig. 1.12.(b)). Lithographic methods can also be used to obtain regular surface textures and hence can be used for more controllable studies. One example is using soft lithography by creating a polydimethylsiloxane (PDMS) mould and then casting polymer or metal precursor and then curing it to form sub-micron posts [58]. Similarly, photolithographic process can be used to produce a regular surface texturing (Fig. 1.12.(c)) [57]. This is done by masking a substrate with a patterned photoresist and then etch the uncoated area. Additionally, a secondary roughness may also be created by plasma etching (Fig. 1.12.(d)) or by nanoparticle coating. This has been proven to increase the performance of LIS when the lubricant is not perfectly wetting the substrate [57]. However, it has been reported that when the lubricant perfectly wets the substrate, the performance of LIS is insensitive to the surface texturing [58,63].

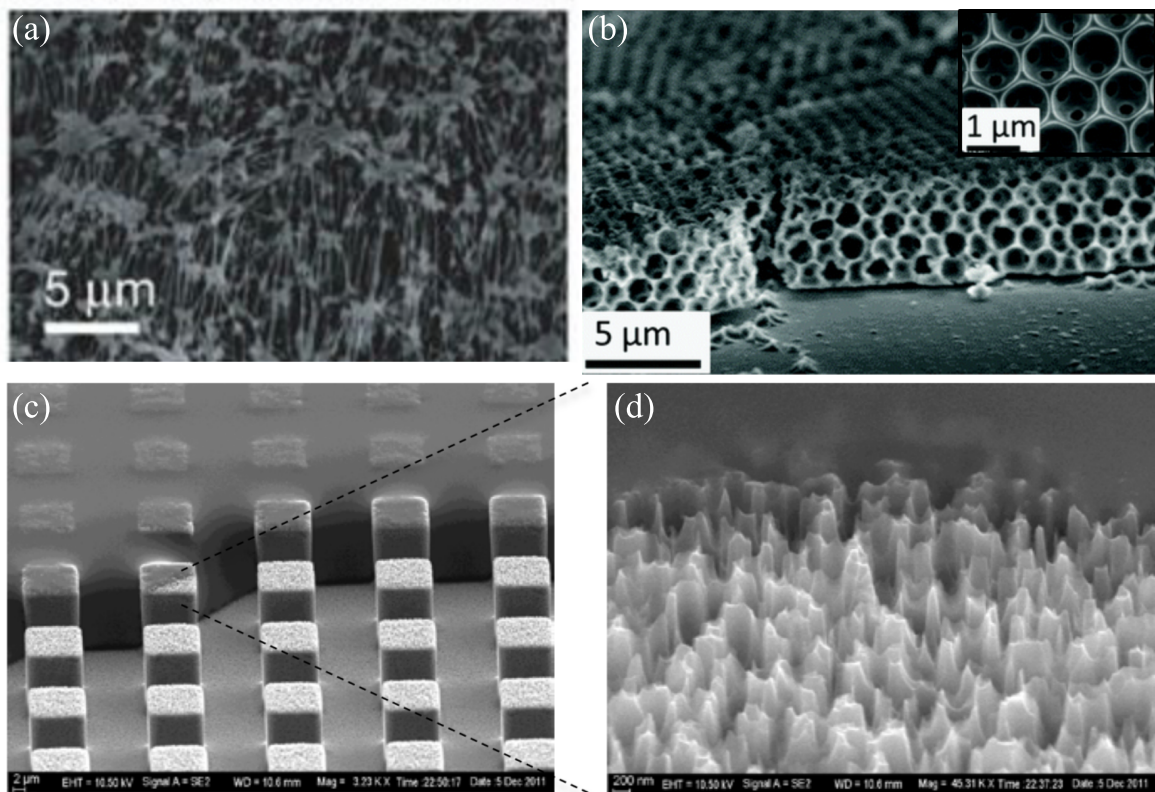


Figure 1.12: Examples of surface textures for LIS: (a) commercially available Teflon microfibre membrane [58], (b) inverse opal [64], and (c) microposts with (d) secondary roughness in form of nanograss [57].

Once the surface texturing is created, the samples need to be infused with lubricant. In many studies, the lubricant phase is usually oil while the droplet is water. This choice of liquid combination can also be reversed if the surface is strongly hydrophilic, such as the one in the peristome of the pitcher plants. The condition of immiscibility may limit the potential applications since this means oil or hydrocarbon-based lubricant can only be used for water or aqueous-based droplet and vice versa. However, there are some liquids that are immiscible for both hydrocarbon and aqueous substances. One of them is DuPont Krytox oils which are non-volatile liquids and have very low surface tension [58]. It can be used as a lubricant to repel droplets from both hydrocarbon and aqueous liquids.

1.6.3 Wetting States

In order to maintain the repellency of LIS, the surface texturing need to be imbided with a lubricant. This can happen naturally if the total free energy when the texture is filled with the lubricant is smaller than when the texture is dry or free from lubricant imbibition (see

Fig. 1.13). Thermodynamically, this can be expressed as

$$r\gamma_{sg} > (r - \varphi_s)\gamma_{sl} + \varphi_s\gamma_{sg} + (1 - \varphi_s)\gamma_{lg}, \quad (1.16)$$

where r and φ_s are the roughness parameter and fraction of solid, which are also used in Eqs. (1.11) and (1.15) respectively. This leads to a requirement on the lubricant-gas contact angle for infusion to happen

$$\frac{\gamma_{sg} - \gamma_{sl}}{\gamma_{lg}} > \frac{(1 - \varphi_s)}{(r - \varphi_s)}, \quad (1.17)$$

$$\cos \theta_{lg} > \frac{(1 - \varphi_s)}{(r - \varphi_s)}. \quad (1.18)$$

Therefore the lubricant wetting angle, must be smaller than $\theta_c = \cos^{-1}((1 - \varphi_s)/(r - \varphi_s))$. This θ_c is the critical wetting angle [16, 57]. When the wetting angle of liquid is lower than θ_c , the surface texture or porosity will guide the lubricant to wet and fill the roughness of the solid. This process is also called hemiwicking. For stable lubricant infusion, in fact, the lubricant wetting angle must be lower than θ_c both when in air, θ_{lg} , and when it is submerged in the other liquid phase used as droplet, θ_{ld} . Otherwise, the droplet may collapse into the surface texture and displace the lubricant, which corresponds to the failure of LIS.

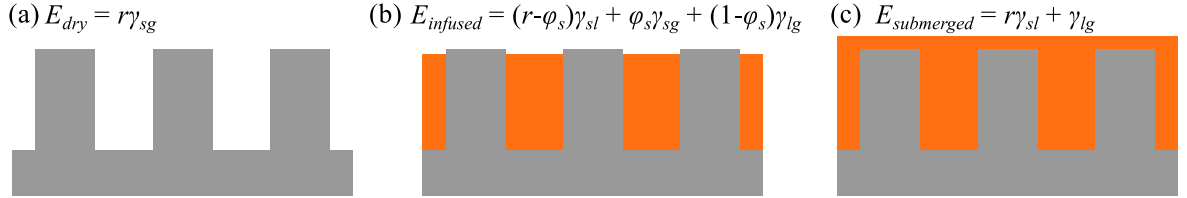


Figure 1.13: Illustrations of three possible surface-lubricant configuration and their associated free energies per unit area. (a) Surface texture without lubricant imbibition. (b) Surface texture imbibed with a partially wetting lubricant. (c) Surface texture imbibed with a fully wetting lubricant.

The lubricant can also wet the surface further and submerge the surface texture (Fig. 1.13.(c)). The total free energy associated with this condition is $E_{submerged} = r\gamma_{sl} + \gamma_{lg}$. The submerged configuration can only happen if $E_{infused} > E_{submerged}$,

$$(r - \varphi_s)\gamma_{sl} + \varphi_s\gamma_{sg} + (1 - \varphi_s)\gamma_{lg} > r\gamma_{sl} + \gamma_{lg}, \quad (1.19)$$

which leads to

$$\frac{\gamma_{sg} - \gamma_{sl}}{\gamma_{lg}} = \cos \theta_{lg} > 1. \quad (1.20)$$

The submerged configuration occurs when the lubricant is perfectly wetting the solid surface [57].

Since θ_{lg} and θ_{ld} can have any value, the lower part of the LIS system can be categorised into one of four different wetting states, which is a combination of infused and submerged states, as illustrated in Fig. 1.14. Smith *et al.* showed that the minimum force required to mobilise the droplet on LIS depends on the wetting states [57].

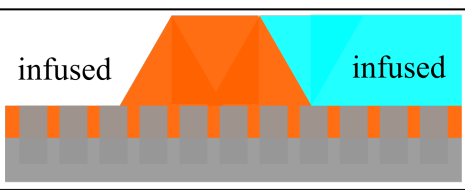
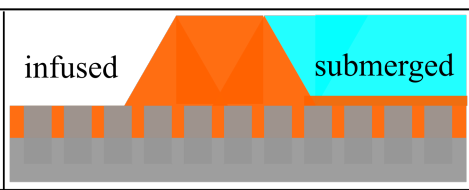
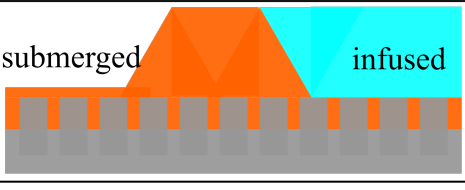
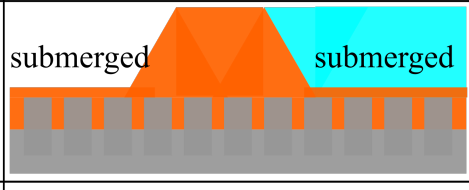
$\frac{(\gamma_{sg} - \gamma_{sl})}{\gamma_{lg}} > \frac{(1 - \varphi_s)}{(r - \varphi_s)}$		
$\frac{(\gamma_{sg} - \gamma_{sl})}{\gamma_{lg}} > 1$		
	$\frac{(\gamma_{sd} - \gamma_{sl})}{\gamma_{ld}} > \frac{(1 - \varphi_s)}{(r - \varphi_s)}$	$\frac{(\gamma_{sd} - \gamma_{sl})}{\gamma_{ld}} > 1$

Figure 1.14: Illustrations of four possible wetting states for the lower part of LIS system.

Another aspect that needs to be considered is the surface tension of the liquids. Some lubricant may encapsulate the droplet if this configuration can reduce the total free energy of the system. This lubricant encapsulation happens when creating the droplet-gas interface is energetically more expensive than creating the droplet-lubricant and lubricant-gas interfaces [65, 66]. Mathematically, this can be expressed as $\gamma_{dg} > \gamma_{dl} + \gamma_{lg}$. Therefore the upper part of the LIS system can fall into 2 wetting states (Fig. 1.15), either the lubricant encapsulates the droplet when $\gamma_{dg} - (\gamma_{dl} + \gamma_{lg}) > 0$, or no lubricant encapsulation when $\gamma_{dg} - (\gamma_{dl} + \gamma_{lg}) < 0$ [57].

1.6.4 Parameters of Liquid Infused Surfaces

To understand the static properties of LIS system, the following parameters play a role. At the wetting ridge, there are three fluid-fluid interfaces, and hence there are three interfacial tensions: droplet-gas γ_{dg} , lubricant-gas γ_{lg} , and lubricant-droplet γ_{ld} interfacial tensions, as shown in Fig. 1.16. In addition, the meniscus to droplet size ratio is related to the ratio of the

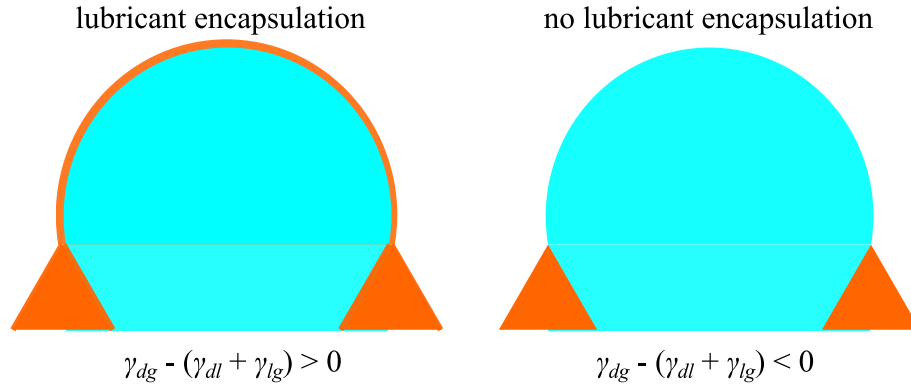


Figure 1.15: Illustrations of two possible wetting states for the upper part of LIS system. When $\gamma_{dg} > \gamma_{dl} + \gamma_{lg}$, the lubricant will encapsulate the droplet to minimise the total free energy.

Laplace pressure of the lubricant-gas interface to the droplet-gas interface [67]. Together, these parameters affect the overall droplet and meniscus shapes in the LIS system. In this thesis, we parameterise the droplet appearance using the apparent contact angle θ_{app} . Following Semprebon *et al.*, we define θ_{app} as the angle created by the droplet-gas interface with the horizontal line measured from the top of the meniscus, as indicated in Fig. 1.16.

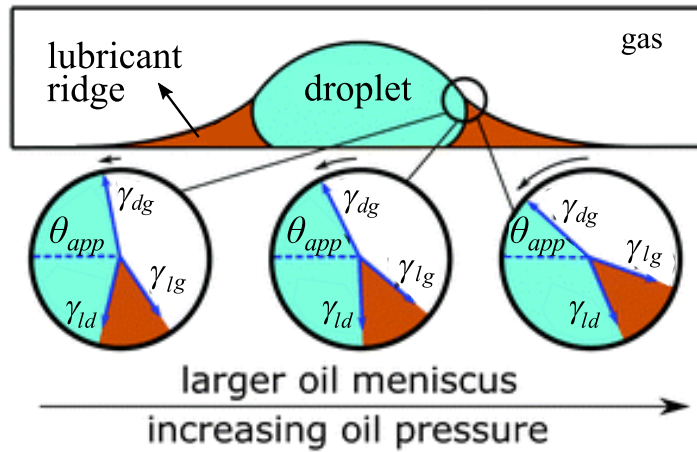


Figure 1.16: The effect of oil pressure and fluid-fluid interfacial tensions, γ 's, to the apparent contact angle θ_{app} [67]. θ_{app} is measured from the top of the lubricant meniscus. The increase in oil pressure causes the contact angle to appear lower.

The fluid-solid phase interactions are represented by the wetting angles. In this thesis, we parameterise the lubricant-gas contact angle (θ_{lg}) and the lubricant-droplet contact angle (θ_{ld}). The remaining droplet-gas contact angle (θ_{dg}) can be recovered from the Girifalco-Good relation as in Eq. (2.18). Since the surface is not flat, the effective wetting angles typically follow the Cassie-Baxter approximation as in Eq. (1.15). The wetting angles influence

LIS system in various aspects, ranging from the apparent contact angle to the generation of spontaneous motion in the presence of topographical gradient, which are extensively discussed in this thesis.

The surface geometry, in general, is an important aspect when studying wetting phenomena. The dimensions of the surface features are directly related to the ability of the lubricant to imbibe the corrugation as well as the apparent contact angle and contact angle hysteresis of droplets on LIS [17,67]. In this thesis, we are also interested to study the effect of topographical variations which create a wetting gradient and lead to a spontaneous droplet motion. While spontaneous motion due to such wetting gradient has been extensively studied for binary fluid systems [35,68], this effect has not been considered for the LIS system.

We are also interested in exploring dynamic effects, which bring the fluid viscosities into relevance. Smith *et al.* suggest that when a droplet is moving on LIS, the energy dissipates mainly in the wetting ridge [57]. Later, Keiser *et al.* show that this is only true when the droplet viscosity η_d is smaller than approximately three times of the lubricant viscosity η_l [69]. Otherwise, the dominant dissipation channel switches from the wetting ridge to the droplet body. In this thesis, we further show that the viscous dissipation at the wetting ridge is not solely determined by lubricant viscosity but also the shape of the wetting ridge, which is affected by the lubricant wetting angles θ_{ld} and θ_{lg} .

1.7 Summary of the Thesis

This thesis focuses on the computational study of the behaviour of a liquid droplet on a LIS. In Chapter 2, we start by describing the two computational methods employed, the lattice Boltzmann and the phase field energy minimisation methods. The former method solves the hydrodynamics equations which can be used to study both statics and dynamics properties of the system. The latter method is powerful to seek the minimum energy states, and it is more effective for capturing the equilibrium properties of the system. These two methods are benchmarked to demonstrate their performance in simulating fluid systems. Further, to confirm the ability of our simulation methods for simulating LIS systems, in Chapter 3, we compare the static droplet morphology and the droplet mobility from our simulations with theoretical prediction and experimental results respectively.

In Chapter 4, we investigate how the lubricant wetting angles modulate the contact line

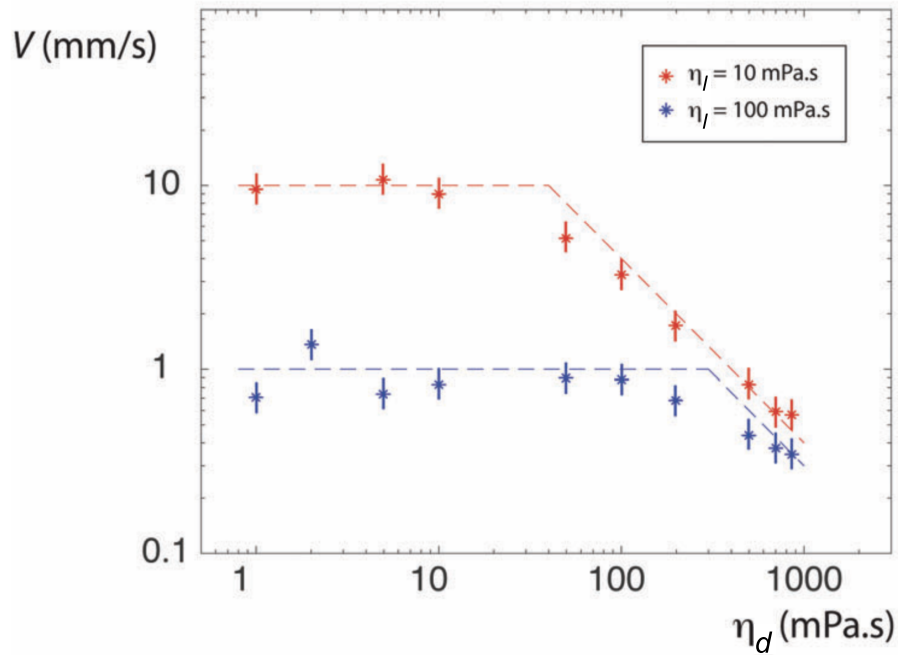


Figure 1.17: Experimental observation of droplet velocity V for various droplet viscosities η_d and lubricant viscosities η_l [69]. The V appears to depend to η_d when $\eta_d > 3\eta_l$ but not when otherwise. This indicates the main dissipation channel switches from the lubricant to the droplet when η_d is increased to be larger than $3\eta_l$.

pinning and the viscous dissipation, and hence influence the droplet mobility. We also assess the fluid flow inside the droplet to quantify the rotational motion of the droplet. We then investigate the contribution of the rotational motion to the overall droplet translational motion in relation to the droplet morphology and viscosity of the droplet and the lubricant.

Next in Chapter 5, we study the effect of a topographical gradient in LIS system. We show that having a topographical gradient can result in bidirectional spontaneous droplet motion. We derive the origin of the force that is responsible for this effect. We show that this bidirectional property is unique to LIS system. Then in Chapter 6, we investigate CAH and the pinning force of a droplet on LIS. The effect of surface tensions, wetting angles, and the solid fraction are investigated. We show how droplets on LIS are prone to failure due to stronger pinning than on superhydrophobic surfaces.

We conclude this thesis in Chapter 7 and discuss the future development of our methods and possible research areas.

CHAPTER 2

Methods

In this thesis, droplet dynamics on liquid infused surfaces (LIS) are investigated using computer simulations. One of the advantages of computational methods is our ability to vary the physical parameters systematically. This allows us to provide insights, complementing experiments, as well as to access parameter regimes which are difficult to study experimentally. Furthermore, experimental errors which come from contaminations and impurities can be isolated and eliminated where necessary.

Our system of interest consists of three fluids and structured solid surfaces. Such ternary fluid system is commonly found in industrial and engineering applications, such as in oil refinery, phase separation, printing and coating [2, 3, 13, 14]. To study ternary fluid systems using computer simulations, we need the appropriate simulation tools which can capture the physics of the system.

We begin this chapter by explaining suitable free energy model for describing the ternary fluid system (section 2.1). We then discuss two simulation methods used in this project, namely the lattice Boltzmann method (section 2.2) and the phase field energy minimisation method (section 2.3). We also detail how the free energy model is implemented to the simulation methods and explain how to check or benchmark the simulation to know that the simulation can capture the physics of the system (section 2.4).

2.1 Ternary Free Energy Model

LIS system consists of three fluid phases (droplet, lubricant and gas phases) and a textured solid. To simulate such system, we need a free energy model which can describe (i) the

coexistence of the three fluid phases, (ii) their interfacial tensions, and (iii) the fluid-solid interactions which determine the contact angle [70]. In principle, there are other physical properties, such as temperature and electric field, which might be relevant for different studies. However, in the current study, we only focus on the interfacial properties of the fluids.

Based on the above requirements, the free energy model can be constructed by introducing potential or energy penalty for the presence or absence of the three fluid phases Ψ_{bulk} , for having an interface between fluid phases $\Psi_{interface}$, and for having an interface with solid surface $\Psi_{surface}$. The total free energy Ψ is defined as the integral of the three potentials over space, which is given by

$$\Psi = \int_V (\Psi_{bulk} + \Psi_{interface}) dV + \int_S \Psi_{surface} dS, \quad (2.1)$$

where V and S account for the volume and surface integral respectively. We shall now describe the potentials which model the three ingredients of the free energy.

2.1.1 Bulk Potential

The first ingredient, the coexistence of three fluid phases, can be modelled using a series of double well potentials of the form $C_m^2(1-C_m)^2$ which have minima at $C_m = 0$ and 1 [71]. Here, C_m is the concentration of a fluid phase m . Using this, when the simulation tool minimizes the energy, the value of C_m will fall into either 1 or 0 in the fluid bulk, which corresponds to the presence or absence of fluid phase m . Since we demand three fluid phases, the first term of the free energy model can be written as [72]

$$\Psi_{bulk} = \sum_{m=1}^3 \frac{\kappa_m}{2} C_m^2 (1 - C_m)^2. \quad (2.2)$$

Here, the κ_m 's are tunable parameters related to the interfacial tension which will be elaborated later.

Originally, Eq. (2.2) has $2^3 = 8$ minima. By introducing a constraint $\sum_m C_m = 1$ we can

force the system to have only 3 minima

$$\begin{aligned}
C_1 = 1, \quad C_2 = 0, \quad C_3 = 0; \\
C_1 = 0, \quad C_2 = 1, \quad C_3 = 0; \\
C_1 = 0, \quad C_2 = 0, \quad C_3 = 1.
\end{aligned} \tag{2.3}$$

This constraint is necessary in order to ensure that only one fluid phase present at a point in space in the fluid bulk.

2.1.2 Interface Potential

The second ingredient, to describe the interfacial tension between two fluid phases, can be modelled using an energy penalty for having a gradient in the concentration $(\nabla C_m)^2$, which happen at interfaces involving phase m . This energy penalty is necessary in order to represent interfacial phenomena [73]. When the system seeks the minimum energy configuration, the system will evolve to have the smallest contribution of the gradient terms, which is equivalent to minimising the interfacial energy. The free energy contribution for having interfaces for the three phases can be written as [72]

$$\Psi_{interface} = \sum_{m=1}^3 \frac{\kappa'_m}{2} (\nabla C_m)^2, \tag{2.4}$$

where the κ'_m 's are also tunable parameters whose values will determine the contribution of the gradient terms to the total free energy.

To compute the interfacial tension between phase m and n , we first can assume that the system only consists of phase m and n and without the presence of any solid surface, such that the total free energy in Eq. (2.1) can be expressed as

$$\Psi = \int_V \left[\frac{\kappa_m}{2} C_m^2 (1 - C_m)^2 + \frac{\kappa_n}{2} C_n^2 (1 - C_n)^2 + \frac{\kappa'_m}{2} (\nabla C_m)^2 + \frac{\kappa'_n}{2} (\nabla C_n)^2 \right] dV. \tag{2.5}$$

Using the constraint $\sum C_i = C_m + C_n = 1$, we can simplify Eq. 2.5 into

$$\Psi = \int_V \left[\frac{\kappa_m + \kappa_n}{2} C_m^2 (1 - C_m)^2 + \frac{\kappa'_m + \kappa'_n}{2} (\nabla C_m)^2 \right] dV. \tag{2.6}$$

We then need to obtain $C_m(x)$ which is the density profile of phase m across the interface at

equilibrium. We can solve $C_m(x)$ from Eq. (2.6) by employing the definition of μ_m which is the chemical potential of phase m as

$$\mu_m = \frac{\delta\Psi}{\delta C_m} = (\kappa_m + \kappa_n) \left(2C_m^3 - 3C_m^2 + C_m - \frac{\kappa'_m + \kappa'_n}{\kappa_m + \kappa_n} \nabla^2 C_m \right). \quad (2.7)$$

Here, we have used functional derivative to obtain μ_m from the integral in Eq. (2.6). From Eq. (2.7), we can see that the chemical potential inside a bulk fluid ($C_m = 1$ or 0) is zero at thermodynamic equilibrium. Since the chemical potential has to be the same everywhere in space at equilibrium, then Eq. (2.7) can be written as

$$\frac{\kappa'_m + \kappa'_n}{\kappa_m + \kappa_n} \nabla^2 C_m = 2C_m^3 - 3C_m^2 + C_m. \quad (2.8)$$

If the interface is assumed to be at $x = 0$, we expect $C_m = 1$ at $x = \infty$ and $C_m = 0$ at $x = -\infty$. Using these boundary conditions we can obtain the solution for Eq. (2.8) as the following

$$C_m(x) = \frac{1}{2} + \frac{1}{2} \tanh \left(\frac{x/2}{\sqrt{(\kappa'_m + \kappa'_n)/(\kappa_m + \kappa_n)}} \right). \quad (2.9)$$

By definition, the interfacial tension is the excess of free energy per unit area, $\gamma_{mn} = \Psi/A$, which implies

$$\gamma_{mn} = \int_{-\infty}^{+\infty} \left[\frac{\kappa_m + \kappa_n}{2} C_m^2 (1 - C_m)^2 + \frac{\kappa'_m + \kappa'_n}{2} (\nabla C_m)^2 \right] dx. \quad (2.10)$$

Substituting the profile in Eq. (2.9) to (2.10), we can obtain the expression for interfacial tension between phases m and n , which is given by

$$\gamma_{mn} = \frac{\alpha}{6} (\kappa_m + \kappa_n), \quad (2.11)$$

where $\alpha = \sqrt{(\kappa'_m + \kappa'_n)/(\kappa_m + \kappa_n)}$ is proportional to the interface width. This definition of α is useful to reduce the number of simulation parameters that need to be defined via $(\kappa'_m + \kappa'_n) = \alpha^2(\kappa_m + \kappa_n)$. Here we always set $\kappa'_m = \alpha^2 \kappa_m$. Therefore, we can rewrite the interface potential in Eq. 2.4 into

$$\Psi_{interface} = \sum_{m=1}^3 \frac{\alpha^2 \kappa_m}{2} (\nabla C_m)^2. \quad (2.12)$$

Since we have three fluid phases in our simulations, we need to define the values of κ_1 ,

κ_2 and κ_3 to set the interfacial tensions between the three fluid phases. For example, assume water, gas, and hexadecane are the fluids that are present in the system. We can then associate each phase with these fluids i.e. phase 1 = water, phase 2 = gas, phase 3, hexadecane. From literature [15], we know the values of the interfacial tensions of these fluids, i.e. $\gamma_{12} = 0.0722$ N/m, $\gamma_{32} = 0.0275$ N/m, and $\gamma_{13} = 0.0533$ N/m. Using Eq. (2.11) and setting $\alpha = 1$ for simplicity we have three equations with three unknowns as the following

$$\begin{aligned}\gamma_{12} &= (\kappa_1 + \kappa_2)/6 = 0.0722; \\ \gamma_{32} &= (\kappa_3 + \kappa_2)/6 = 0.0275; \\ \gamma_{13} &= (\kappa_1 + \kappa_3)/6 = 0.0533.\end{aligned}\tag{2.13}$$

Solving the above equations, we obtain $\kappa_1 = 0.294$, $\kappa_2 = 0.1392$, and $\kappa_3 = 0.0258$.

In general, the parameters κ can be calculated as the following

$$\begin{aligned}\kappa_1 &= 3(\gamma_{12} + \gamma_{13} - \gamma_{32}); \\ \kappa_2 &= 3(\gamma_{12} - \gamma_{13} + \gamma_{32}); \\ \kappa_3 &= -3(\gamma_{12} - \gamma_{13} - \gamma_{32}).\end{aligned}\tag{2.14}$$

We can see that κ_3 is negative when $(\gamma_{12} - \gamma_{13} - \gamma_{32}) > 0$. This condition is equivalent to the condition where fluid 1 (the droplet) is encapsulated by fluid 3 (the lubricant), as has been previously shown in Fig. 1.15. Since negative value of κ_3 flips the double well potential into double barrier potential, C_3 will go to $-\infty$ or ∞ and the simulation becomes unstable. Hence, this free energy model is not suitable for cases where the lubricant is encapsulating the droplet. The presence of lubricant encapsulation also requires long ranged attraction and short ranged repulsion between two interfaces [55]. These interactions are not incorporated in this free energy model. Therefore, the current free energy model cannot be used to capture the lubricant encapsulation condition. Recently, Wang *et al.* proposed a modification to the free energy model that allows lubricant encapsulation case to be captured correctly [74].

2.1.3 Wetting Potential

The third ingredient is to model solid-fluid interaction, which can be described by the wetting potential. To formulate this wetting potential, we can use an assumption proposed by Cahn and de Gennes [75,76], that the fluid concentration profile in the direction normal to the surface

$C_m(z)$ is continuous and the interaction can be expressed as a power series. Technically, there is no restriction in the number of terms in the power series that can be involved. In this thesis, we use two forms of $\Psi_{surface}$. In the first form, we involve only the linear term, which is called the linear wetting potential. In the second form, we consider up to the cubic terms, which is called the cubic wetting potential.

Linear wetting potential

For linear wetting potential, $\Psi_{surface}$ takes the following form [72, 73]

$$\Psi_{surface} = \sum_{m=1}^3 -h_m C_m|_s \quad (2.15)$$

where $C_m|_s$ is the concentration of phase m at solid boundary and h_m 's are simulation parameters which still need to be specified. The surface free energy of solid can be obtained by evaluating the excess of free energy per unit area, in a similar procedure to obtain the surface tension of fluid-fluid interface given in Eq. (2.11). In this case, the surface free energy of solid having interface with phase m γ_{sm} is given by [72]

$$\begin{aligned} \gamma_{sm} = & -h_m C_m|_s + \frac{\alpha}{12} \left(\kappa_m + \sqrt{1 + \frac{4h_m}{\alpha\kappa_m} \left(\frac{2h_m}{\alpha} - \kappa_m \right)} \right) \\ & + \sum_{n \neq m} -h_n C_n|_s + \frac{\alpha}{12} \left(\kappa_n - \sqrt{1 - \frac{4h_n}{\alpha\kappa_n} \left(\frac{2h_n}{\alpha} + \kappa_n \right)} \right). \end{aligned} \quad (2.16)$$

Using the definition of Young's contact angle of phase m in phase n environment, $\cos \theta_{mn} = (\gamma_{sn} - \gamma_{sm})/\gamma_{mn}$, the h_m parameters can be related to wetting contact angle via [72]

$$\cos \theta_{mn} = \frac{(\alpha\kappa_n + 4h_n)^{3/2} - (\alpha\kappa_n - 4h_n)^{3/2}}{2(\kappa_m + \kappa_n)(\alpha\kappa_n)^{1/2}} - \frac{(\alpha\kappa_m + 4h_m)^{3/2} - (\alpha\kappa_m - 4h_m)^{3/2}}{2(\kappa_m + \kappa_n)(\alpha\kappa_m)^{1/2}}. \quad (2.17)$$

We can obtain the values of the h_m parameters by specifying the desired values of the contact angles. For example, continuing the previous example in Eq. (2.11), we can choose the contact angle of hexadecane in air θ_{32} and in water θ_{31} to be 30° and 40° respectively. Using Girifalco-Good relation [15],

$$\gamma_{12} \cos \theta_{12} + \gamma_{23} \cos \theta_{23} + \gamma_{31} \cos \theta_{31} = 0, \quad (2.18)$$

we obtain $\theta_{12} = 103.6^\circ$. Here, we have used $\cos \theta_{23} = \cos(\pi - \theta_{32}) = -\cos \theta_{32}$. From Eq. (2.17),

using the values of θ_{mn} and the values of κ and α obtained earlier, we can have three equations with three unknowns. With the aid of a computer program, we can numerically solve for the h_m parameters and obtain $h_1 = -0.0351241$, $h_2 = -0.0179706$, and $h_3 = 0.00641307$.

It is also useful to determine the value of $C_m|_s$ at the solid boundary for implementing $\Psi_{surface}$ in the simulation. To do this, first we can write the change of the total energy with the change of density $C_m|_s$ [77].

$$\begin{aligned} \delta\Psi_m &= \int_V \kappa_m(2C_m^3 - 3C_m^2 + C_m)\delta C_m dV + \\ &\int_V \alpha^2 \kappa_m(\nabla C_m) \cdot (\nabla \delta C_m) dV + \int_S \frac{d\Psi_{surface}}{dC_m|_s} \delta C_m|_s dS \end{aligned} \quad (2.19)$$

$$\begin{aligned} &= \int_V \kappa_m(2C_m^3 - 3C_m^2 + C_m)\delta C_m dV + \\ &\int_V \alpha^2 \kappa_m(\nabla \cdot (\delta C_m \nabla C_m) - \nabla^2 C_m \delta C_m) dV + \int_S \frac{d\Psi_{surface}}{dC_m|_s} \delta C_m|_s dS \end{aligned} \quad (2.20)$$

$$\begin{aligned} &= \int_V [\kappa_m(2C_m^3 - 3C_m^2 + C_m) - \alpha^2 \kappa_m \nabla^2 C_m] \delta C_m dV + \\ &\int_V \alpha^2 \kappa_m(\nabla \cdot (\delta C_m \nabla C_m)) dV + \int_S \frac{d\Psi_{surface}}{dC_m|_s} \delta C_m|_s dS \end{aligned} \quad (2.21)$$

The integrand of the first volume integral is the definition of the chemical potential as in Eq. (2.7). The second volume integral can be expressed as the surface integral using the divergence theorem such that

$$\begin{aligned} \delta\Psi_m &= \int_V [\kappa_m(2C_m^3 - 3C_m^2 + C_m) - \alpha^2 \kappa_m \nabla^2 C_m] \delta C_m dV + \\ &\int_S \alpha^2 \kappa_m [(\delta C_m|_s \nabla C_m) \cdot \hat{\mathbf{n}}] dS + \int_S \frac{d\Psi_{surface}}{dC_m|_s} \delta C_m|_s dS \end{aligned} \quad (2.22)$$

$$\begin{aligned} &= \int_V [\kappa_m(2C_m^3 - 3C_m^2 + C_m) - \alpha^2 \kappa_m \nabla^2 C_m] \delta C_m dV + \\ &\int_S \left[\alpha^2 \kappa_m \nabla C_m \cdot \hat{\mathbf{n}} + \frac{d\Psi_{surface}}{dC_m|_s} \right] \delta C_m|_s dS, \end{aligned} \quad (2.23)$$

where $\hat{\mathbf{n}}$ is the unit vector normal to the surface. Minimisation of the total energy respect to $C_m|_s$ leads to a boundary condition

$$\alpha^2 \kappa_m \nabla C_m \cdot \hat{\mathbf{n}} = -\frac{d\Psi_{surface}}{dC_m|_s}. \quad (2.24)$$

For the linear wetting potential, this can be simplified into

$$\alpha^2 \kappa_m \nabla_{\perp} C_m|_s = h_m, \quad (2.25)$$

which means that the gradient of $C_m|_s$ normal to the surface is equal to $h_m/\alpha^2\kappa_m$.

The value of h_m itself controls the strength of the interaction of phase m with the surface. If $h_m > 0$, the surface favours to interact with phase m since adding more C_m reduces the total free energy. In contrast, if $h_m < 0$, the surface disfavour interaction with phase m . There will also be competition with other phases which is determined by the value of the corresponding h_m .

Cubic wetting potential

Another option for wetting potential is the cubic wetting potential, which involves the cubic term of the free energy. As described by Connington *et al.* the cubic wetting potential for binary fluid case is written as [78]

$$\Psi_{surface} = -6\gamma \cos \theta_e \left(\frac{1}{2}C_m|_s^2 - \frac{1}{3}C_m|_s^3 \right), \quad (2.26)$$

where γ and θ_e are the surface tension and the equilibrium contact angle respectively. The corresponding boundary condition given as

$$\nabla_{\perp} C_m|_s = -6\gamma \cos \theta_e (C_m|_s - C_m|_s^2). \quad (2.27)$$

Connington *et al.* have also used the same bulk and interface free energy construction as given in Eq. (2.6) [78], which means that the definition of the surface tension γ in Eq. (2.27) is the same as ours in Eq. (2.11).

In our simulation, we need to generalise the cubic wetting potential since there are two wetting angles that have to be specified. The remaining wetting angle is determined via the Gririfalco-Good relation. The choice of wetting angles that are specified is arbitrary. However, all of the three phases need to be involved e.g. θ_{12} and θ_{32} . In this case, the corresponding cubic wetting potential is expressed as

$$\Psi_{surface} = -\alpha(\kappa_1 + \kappa_2) \cos \theta_{12} \left(\frac{1}{2}C_1|_s^2 - \frac{1}{3}C_1|_s^3 \right) - \alpha(\kappa_3 + \kappa_2) \cos \theta_{32} \left(\frac{1}{2}C_3|_s^2 - \frac{1}{3}C_3|_s^3 \right). \quad (2.28)$$

It can be shown that Eq. (2.28) reduces to Eq. (2.26) when only any two of the three phases are considered.

Compared to the linear wetting potential, one of the advantages of using the cubic wetting

potential is to remove phase enrichment or depletion close to the surface [78]. The phase enrichment or depletion can cause inaccuracy when studying the static and dynamic properties of the system. Another strong point of using the cubic wetting potential is that the wetting angles can be specified directly without the need to solve equations to determine the simulation parameter as in for the linear wetting potential.

2.2 Lattice Boltzmann Method

One way to study dynamic wetting phenomena is by using the lattice Boltzmann (LB) method. The LB method is used to simulate the hydrodynamics of the system by solving the equations of motion of the fluid system. The free energy model that has been discussed earlier enters the simulation system as the thermodynamic force that drives the system toward the equilibrium. Dynamic properties of the system, such as the effect of the fluid viscosities and the applied body force, can also be specified easily and can be varied systematically.

2.2.1 Solving the Hydrodynamic Equations

The equations of motion for fluid system are given by the continuity and the Navier-Stokes equations:

$$\partial_t \rho + \partial_\gamma (\rho v_\gamma) = 0, \quad (2.29)$$

$$\partial_t (\rho v_\alpha) + \partial_\beta (\rho v_\alpha v_\beta) = -\partial_\beta P_{\alpha\beta} + \partial_\beta \eta (\partial_\beta v_\alpha + \partial_\alpha v_\beta). \quad (2.30)$$

Here, ρ, v, η , and P are the density, velocity and dynamic viscosity of the fluid and pressure tensor respectively, while indices α, β, γ are related to spatial coordinate. In our model, the density is the sum of the concentration of all fluid components $\rho = C_1 + C_2 + C_3$.

The derivation on how the LB scheme captures the continuity and Navier-Stokes equations are beyond the scope of this dissertation and can be found in a number of textbooks, such as in Ref. [77]. The starting point of the LB algorithm is the Boltzmann transport equation. When the Bhatnagar-Gross-Krook collision is employed, it can be written as

$$\frac{df}{dt} = -\frac{1}{\tau} (f - f^{eq}). \quad (2.31)$$

where f, f^{eq} , and τ are the particle distribution function, the local equilibrium distribution function and the relaxation time respectively. The particle distribution function f describes

the density of particles at a given position, velocity, and time, while the local equilibrium distribution function f^{eq} dictates its expected particle density. The shape of f^{eq} needs to be specified. The relations between the distribution function and the macroscopic quantities, such as mass density ρ and momentum density ρv , are given by

$$\rho(\mathbf{x}, t) = \int f(\mathbf{x}, \mathbf{c}, t) d^3 c, \quad (2.32)$$

$$\rho(\mathbf{x}, t) \mathbf{v}(\mathbf{x}, t) = \int \mathbf{c} f(\mathbf{x}, \mathbf{c}, t) d^3 c, \quad (2.33)$$

where \mathbf{c} is the velocity of the particle.

Eq. (2.31) is also called the collision operator where it models the collision of particles as a relaxation towards an equilibrium condition. We can express this equation in a discretised form to obtain the time evolution equation of the distribution function

$$f(\mathbf{x} + \mathbf{c}\Delta t, t + \Delta t) = f(\mathbf{x}, t) - \frac{\Delta t}{\tau} (f(\mathbf{x}, t) - f^{eq}). \quad (2.34)$$

Eq. (2.34) is the core of the LB simulation. The Δt in Eq. (2.34) manifests in the simulation as a timestep or iteration, thus $\Delta t = 1$. We can see from Eq. (2.34) that, as the iteration goes, f evolves toward f^{eq} with a relaxation time τ .

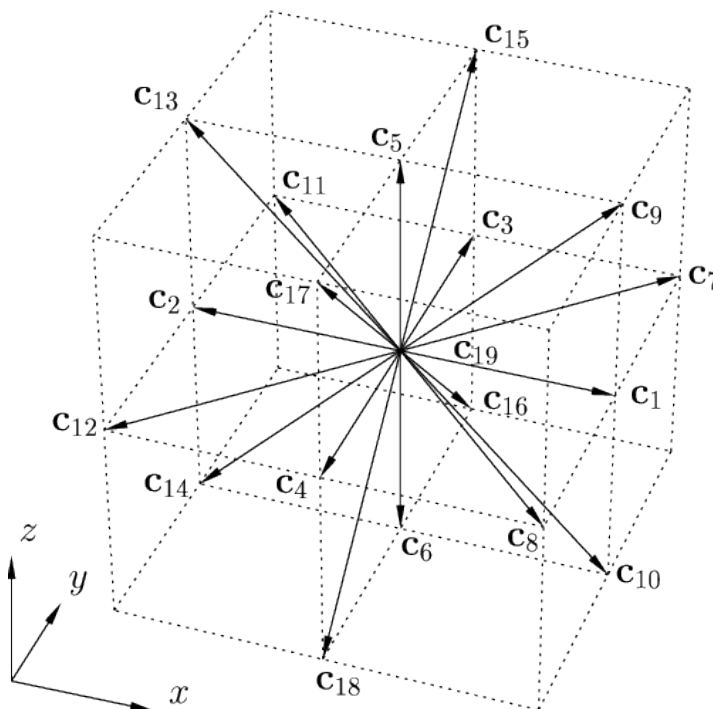


Figure 2.1: A unit cell of D3Q19 lattice velocity model. The \mathbf{c} 's represent the discretised velocity directions.

In LB simulation, the space, time and velocity vector are discretised. We use the D3Q19 lattice model where the velocity vectors are discretised into 19 directions \mathbf{c}_i in three dimensions as shown in Fig. 2.1. For each \mathbf{c}_i , we assign particle distribution function f_i . The time evolution of f_i can be written as

$$f_i(\mathbf{x} + \mathbf{c}_i, t + 1) = f_i - \frac{1}{\tau}(f_i - f_i^{eq}). \quad (2.35)$$

For each timestep, we need to calculate f_i^{eq} and compute $f_i^*(\mathbf{x}, t) = f_i - \frac{1}{\tau}(f_i - f_i^{eq})$. This step is called the collision step. Then, at the next timestep, we assign $f(\mathbf{x} + \mathbf{c}_i, t + 1) = f_i^*(\mathbf{x}, t)$, which means that the value obtained from the collision step is assigned as the value of f_i of the neighbouring node at the direction of \mathbf{c}_i for the next timestep. This step is called the propagation step. LB simulation is carried out by performing the collision and the propagation steps iteratively for every velocity direction \mathbf{c}_i and for every lattice node. This process is illustrated in Fig. 2.2.

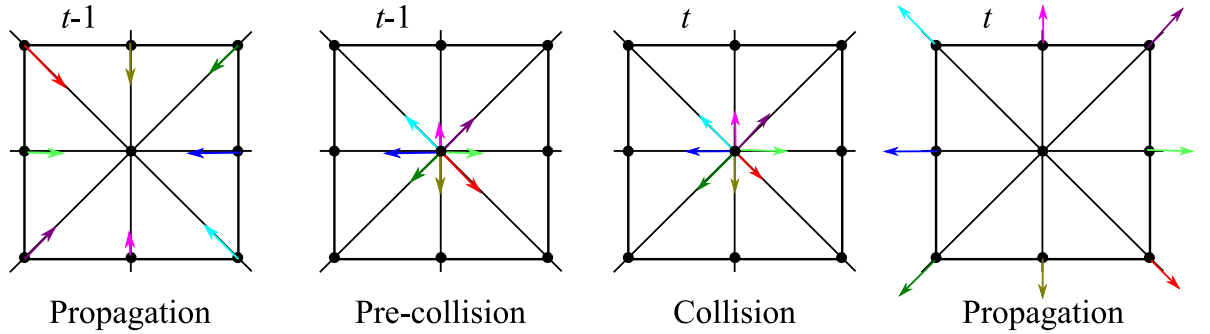


Figure 2.2: At initial propagation step ($t - 1$), f_i from nodes around the central node are streamed to the central node. Each f_i is indicated with different colour. At pre-collision step, f_i at the centre node are assigned with these new values. These new values are used to calculate f_i^{eq} and $f_i - \frac{1}{\tau}(f_i - f_i^{eq})$ at the collision step. Finally, the new values of f_i are propagated to the neighbouring nodes at the next propagation step (t).

The above procedure is sufficient to recover the Navier-Stokes and the continuity equations for the system of one fluid phase. In this case, f_i^{eq} can be expressed as the Maxwell-Boltzmann equilibrium distribution function. When written in power series up to the second order in velocity, f_i^{eq} is given by

$$f_i^{eq}(\mathbf{x}, t) = w_i \rho \left(1 + \frac{c_{i\alpha} v_\alpha}{c_s^2} + \frac{v_\alpha v_\beta (c_{i\alpha} c_{i\beta} - c_s^2 \delta_{\alpha\beta})}{2c_s^4} \right), \quad (2.36)$$

where c_s and w_i are the speed of sound $c_s = \Delta x / \Delta t \sqrt{3}$, and the weight factor whose values are specific for each of the velocity direction. However, the above distribution function does not

describe fluid-fluid and fluid-solid interactions, which are required in this study. To add additional physics due to surface tension, we need to choose the shape of f_i^{eq} that can incorporate the thermodynamic properties of the system. The choice of f_i^{eq} is not unique, but it has to satisfy the following constraints

$$\sum_i f_i^{eq} = \rho, \quad (2.37)$$

$$\sum_i f_i^{eq} c_{i\alpha} = \rho v_\alpha, \quad (2.38)$$

$$\sum_i f_i^{eq} c_{i\alpha} c_{i\beta} = P_{\alpha\beta} + \rho v_\alpha v_\beta, \quad (2.39)$$

where $P_{\alpha\beta}$ is the pressure tensor which also appears in the Navier-Stokes equation Eq. (2.30). This pressure tensor is also where the thermodynamic properties prescribed by the free energy model enter the LB equation. These constraints correspond to the conservation of mass, momentum and concentration.

As a reminder, the free energy model in the absence of solid surface is given by

$$\Psi = \int_V \sum_{m=1}^3 \left(\frac{\kappa_m}{2} C_m^2 (1 - C_m)^2 + \frac{\alpha^2 \kappa_m}{2} (\nabla C_m)^2 \right) dV. \quad (2.40)$$

In our LB implementation, we carry out a coordinate transformation

$$\rho = C_1 + C_2 + C_3; \quad \phi = C_1 - C_2; \quad \psi = C_3. \quad (2.41)$$

ϕ and ψ are order parameters which we have introduced to distinguish the fluid phases. Correspondingly, the relation of the fluid concentration with these order parameter is given by

$$C_1 = (\rho + \phi - \psi)/2; \quad C_2 = (\rho - \phi - \psi)/2; \quad C_3 = \psi. \quad (2.42)$$

Substituting Eq. (2.42) into Eq. (2.40) we can write the free energy model as function of the order parameters

$$\begin{aligned} F = \int_V \left[\frac{\kappa_1}{32} (\rho + \phi - \psi)^2 (2 + \psi - \rho - \phi)^2 + \frac{\alpha^2 \kappa_1}{8} (\nabla \rho + \nabla \phi - \nabla \psi)^2 + \right. \\ \left. \frac{\kappa_2}{32} (\rho - \phi - \psi)^2 (2 + \psi - \rho + \phi)^2 + \frac{\alpha^2 \kappa_2}{8} (\nabla \rho - \nabla \phi - \nabla \psi)^2 + \right. \\ \left. \frac{\kappa_3}{2} \psi^2 (1 - \psi)^2 + \frac{\alpha^2 \kappa_3}{2} (\nabla \psi)^2 \right] dV \end{aligned} \quad (2.43)$$

and we can obtain the chemical potentials of each order parameter

$$\begin{aligned}\mu_\rho = & \frac{\kappa_1}{8}(\rho + \phi - \psi)(\rho + \phi - \psi - 2)(\rho + \phi - \psi - 1) + \\ & \frac{\kappa_2}{8}(\rho - \phi - \psi)(\rho - \phi - \psi - 2)(\rho - \phi - \psi - 1) + \\ & \frac{\alpha^2}{4}[(\kappa_1 + \kappa_2)(\nabla^2\psi - \nabla^2\rho) + (\kappa_2 - \kappa_1)\nabla^2\phi],\end{aligned}\quad (2.44)$$

$$\begin{aligned}\mu_\phi = & \frac{\kappa_1}{8}(\rho + \phi - \psi)(\rho + \phi - \psi - 2)(\rho + \phi - \psi - 1) - \\ & \frac{\kappa_2}{8}(\rho - \phi - \psi)(\rho - \phi - \psi - 2)(\rho - \phi - \psi - 1) + \\ & \frac{\alpha^2}{4}[(\kappa_2 - \kappa_1)(\nabla^2\rho - \nabla^2\psi) - (\kappa_1 + \kappa_2)\nabla^2\phi],\end{aligned}\quad (2.45)$$

$$\begin{aligned}\mu_\psi = & -\frac{\kappa_1}{8}(\rho + \phi - \psi)(\rho + \phi - \psi - 2)(\rho + \phi - \psi - 1) - \\ & -\frac{\kappa_2}{8}(\rho - \phi - \psi)(\rho - \phi - \psi - 2)(\rho - \phi - \psi - 1) + \kappa_3\psi(\psi - 1)(2\psi - 1) + \\ & \frac{\alpha^2}{4}[(\kappa_1 + \kappa_2)\nabla^2\rho - (\kappa_2 - \kappa_1)\nabla^2\phi - (\kappa_2 + \kappa_1 + 4\kappa_3)\nabla^2\psi],\end{aligned}\quad (2.46)$$

The chemical potential itself is the measure of free energy change by adding or removing materials at a particular point. At equilibrium the chemical potential has to be the same everywhere. Any inhomogeneity will lead to a body force that transfers material from higher μ to lower μ . In our case, the corresponding body force is proportional to the gradient of the chemical potential times the order parameter. Therefore, the generalised form of the pressure tensor gradient is written as

$$\partial_\beta P_{\alpha\beta} = \partial_\alpha p_b + \rho\partial_\alpha\mu_\rho + \phi\partial_\alpha\mu_\phi + \psi\partial_\alpha\mu_\psi, \quad (2.47)$$

which reads

$$\begin{aligned}
P_{\alpha\beta} = & p_b \delta_{\alpha\beta} + \alpha^2 \kappa_{\rho\rho} [(\partial_\alpha \rho)(\partial_\beta \rho) - (1/2)(\partial_\gamma \rho)^2 \delta_{\alpha\beta} - \rho(\partial_{\gamma\gamma} \rho) \delta_{\alpha\beta}] \\
& + \alpha^2 \kappa_{\phi\phi} [(\partial_\alpha \phi)(\partial_\beta \phi) - (1/2)(\partial_\gamma \phi)^2 \delta_{\alpha\beta} - \phi(\partial_{\gamma\gamma} \phi) \delta_{\alpha\beta}] \\
& + \alpha^2 \kappa_{\psi\psi} [(\partial_\alpha \psi)(\partial_\beta \psi) - (1/2)(\partial_\gamma \psi)^2 \delta_{\alpha\beta} - \psi(\partial_{\gamma\gamma} \psi) \delta_{\alpha\beta}] \\
& + \alpha^2 \kappa_{\rho\phi} [(\partial_\alpha \rho)(\partial_\beta \phi) + (\partial_\alpha \phi)(\partial_\beta \rho) - (\partial_\gamma \rho)(\partial_\gamma \phi) \delta_{\alpha\beta} - \rho(\partial_{\gamma\gamma} \phi) \delta_{\alpha\beta} - \phi(\partial_{\gamma\gamma} \rho) \delta_{\alpha\beta}] \\
& + \alpha^2 \kappa_{\rho\psi} [(\partial_\alpha \rho)(\partial_\beta \psi) + (\partial_\alpha \psi)(\partial_\beta \rho) - (\partial_\gamma \rho)(\partial_\gamma \psi) \delta_{\alpha\beta} - \rho(\partial_{\gamma\gamma} \psi) \delta_{\alpha\beta} - \psi(\partial_{\gamma\gamma} \rho) \delta_{\alpha\beta}] \\
& + \alpha^2 \kappa_{\phi\psi} [(\partial_\alpha \phi)(\partial_\beta \psi) + (\partial_\alpha \psi)(\partial_\beta \phi) - (\partial_\gamma \phi)(\partial_\gamma \psi) \delta_{\alpha\beta} - \phi(\partial_{\gamma\gamma} \psi) \delta_{\alpha\beta} - \psi(\partial_{\gamma\gamma} \phi) \delta_{\alpha\beta}], \quad (2.48)
\end{aligned}$$

where

$$\begin{aligned}
p_b = & \rho c_s^2 + (\kappa_1 + \kappa_2) \left[\frac{3}{32} \rho^4 + \frac{3}{32} \phi^4 + \frac{9}{16} \rho^2 \phi^2 + \frac{9}{16} \rho^2 \psi^2 + \frac{9}{16} \phi^2 \psi^2 - \frac{3}{8} \rho^3 \psi - \frac{3}{8} \rho \psi^3 + \right. \\
& \left. \frac{3}{4} \rho^2 \psi - \frac{3}{4} \rho \phi^2 - \frac{3}{4} \rho \psi^2 + \frac{3}{4} \phi^2 \psi - \frac{1}{4} \rho^3 + \frac{1}{8} \rho^2 + \frac{1}{8} \phi^2 - \frac{1}{4} \rho \psi - \frac{9}{8} \rho \phi^2 \psi \right] + \\
& (\kappa_1 - \kappa_2) \left[\frac{3}{8} \rho^3 \phi + \frac{3}{8} \rho \phi^3 - \frac{3}{8} \phi^3 \psi - \frac{3}{8} \phi \psi^3 - \frac{1}{4} \phi^3 - \frac{3}{4} \rho^2 \phi - \frac{3}{4} \phi \psi^2 + \frac{1}{4} \rho \phi - \frac{1}{4} \phi \psi + \right. \\
& \left. \frac{9}{8} \rho \phi \psi^2 - \frac{9}{8} \rho^2 \phi \psi + \frac{3}{2} \rho \phi \psi \right] + \frac{1}{4} (\kappa_1 + \kappa_2 - 8\kappa_3) \psi^3 + (\kappa_1 + \kappa_2 + 16\kappa_3) \left[\frac{3}{32} \psi^4 + \frac{1}{32} \psi^2 \right], \quad (2.49)
\end{aligned}$$

and

$$\begin{aligned}
\kappa_{\rho\rho} = \kappa_{\phi\phi} = \frac{\kappa_1 + \kappa_2}{4}, & \quad \kappa_{\psi\psi} = \frac{\kappa_1 + \kappa_2 + 4\kappa_3}{4}, \\
\kappa_{\rho\phi} = -\kappa_{\phi\psi} = \frac{\kappa_1 - \kappa_2}{4}, & \quad \kappa_{\rho\psi} = -\frac{\kappa_1 + \kappa_2}{4}. \quad (2.50)
\end{aligned}$$

Using this generalised pressure tensor, f_i^{eq} can be formulated to satisfy Eqs. (2.37 - 2.39).

In our LB implementation, the suitable f_i^{eq} is written as

$$\begin{aligned}
f_i^{eq} = & w_i \left(\frac{p_b}{c_s^2} + \frac{e_{i\alpha} \rho v_\alpha}{c_s^2} + \frac{\rho v_\alpha v_\beta (e_{i\alpha} e_{i\beta} - c_s^2 \delta_{\alpha\beta})}{2c_s^4} \right) - \frac{w_i}{c_s^2} (\kappa_{\rho\rho} \rho \nabla^2 \rho + \kappa_{\phi\phi} \phi \nabla^2 \phi + \kappa_{\psi\psi} \psi \nabla^2 \psi) \\
& + \frac{\kappa_{\rho\rho}}{c_s^2} (w_i^{xx} \partial_x \rho \partial_x \rho + w_i^{yy} \partial_y \rho \partial_y \rho + w_i^{zz} \partial_z \rho \partial_z \rho + w_i^{xy} \partial_x \rho \partial_y \rho + w_i^{yz} \partial_y \rho \partial_z \rho + w_i^{zx} \partial_z \rho \partial_x \rho) \\
& + \frac{\kappa_{\phi\phi}}{c_s^2} (w_i^{xx} \partial_x \phi \partial_x \phi + w_i^{yy} \partial_y \phi \partial_y \phi + w_i^{zz} \partial_z \phi \partial_z \phi + w_i^{xy} \partial_x \phi \partial_y \phi + w_i^{yz} \partial_y \phi \partial_z \phi + w_i^{zx} \partial_z \phi \partial_x \phi) \\
& + \frac{\kappa_{\psi\psi}}{c_s^2} (w_i^{xx} \partial_x \psi \partial_x \psi + w_i^{yy} \partial_y \psi \partial_y \psi + w_i^{zz} \partial_z \psi \partial_z \psi + w_i^{xy} \partial_x \psi \partial_y \psi + w_i^{yz} \partial_y \psi \partial_z \psi + w_i^{zx} \partial_z \psi \partial_x \psi) \\
& + \frac{2\kappa_{\rho\phi}}{c_s^2} (w_i^{xx} \partial_x \rho \partial_x \phi + w_i^{yy} \partial_y \rho \partial_y \phi + w_i^{zz} \partial_z \rho \partial_z \phi) - \frac{w_i}{c_s^2} (\kappa_{\rho\phi} \rho \nabla^2 \phi + \kappa_{\rho\phi} \phi \nabla^2 \rho) \\
& + \frac{\kappa_{\rho\phi}}{c_s^2} (w_i^{xy} \partial_x \rho \partial_y \phi + w_i^{xy} \partial_y \rho \partial_x \phi + w_i^{yz} \partial_y \rho \partial_z \phi + w_i^{yz} \partial_y \rho \partial_z \phi + w_i^{zx} \partial_z \rho \partial_x \phi + w_i^{zx} \partial_z \rho \partial_x \phi) \\
& + \frac{2\kappa_{\rho\psi}}{c_s^2} (w_i^{xx} \partial_x \rho \partial_x \psi + w_i^{yy} \partial_y \rho \partial_y \psi + w_i^{zz} \partial_z \rho \partial_z \psi) - \frac{w_i}{c_s^2} (\kappa_{\rho\psi} \rho \nabla^2 \psi + \kappa_{\rho\psi} \psi \nabla^2 \rho) \\
& + \frac{\kappa_{\rho\psi}}{c_s^2} (w_i^{xy} \partial_x \rho \partial_y \psi + w_i^{xy} \partial_y \rho \partial_x \psi + w_i^{yz} \partial_y \rho \partial_z \psi + w_i^{yz} \partial_y \rho \partial_z \psi + w_i^{zx} \partial_z \rho \partial_x \psi + w_i^{zx} \partial_z \rho \partial_x \psi) \\
& + \frac{2\kappa_{\phi\psi}}{c_s^2} (w_i^{xx} \partial_x \phi \partial_x \psi + w_i^{yy} \partial_y \phi \partial_y \psi + w_i^{zz} \partial_z \phi \partial_z \psi) - \frac{w_i}{c_s^2} (\kappa_{\phi\psi} \phi \nabla^2 \psi + \kappa_{\phi\psi} \psi \nabla^2 \phi) \\
& + \frac{\kappa_{\phi\psi}}{c_s^2} (w_i^{xy} \partial_x \phi \partial_y \psi + w_i^{xy} \partial_y \phi \partial_x \psi + w_i^{yz} \partial_y \phi \partial_z \psi + w_i^{yz} \partial_y \phi \partial_z \psi + w_i^{zx} \partial_z \phi \partial_x \psi + w_i^{zx} \partial_z \phi \partial_x \psi),
\end{aligned} \tag{2.51}$$

with the weight factors $w_{1-6} = 1/18$, $w_{7-18} = 1/36$, $w_{1,2}^{xx} = w_{3,4}^{yy} = w_{5,6}^{zz} = 5/36$, $w_{3-6}^{xx} = w_{1,2,5,6}^{yy} = w_{1-4}^{zz} = -1/9$, $w_{7-10}^{xx} = w_{15-18}^{xx} = w_{7-14}^{yy} = w_{11-18}^{zz} = -1/72$, $w_{11-14}^{xx} = w_{15-18}^{yy} = w_{7-10}^{zz} = 1/36$, $w_{1-6}^{xy} = w_{1-6}^{yz} = w_{1-6}^{zx} = 0$, $w_{7,10}^{xy} = w_{11,14}^{yz} = w_{15,18}^{zx} = 1/12$, $w_{8,9}^{xy} = w_{12,13}^{yz} = w_{16,17}^{zx} = -1/12$, $w_{11-18}^{xy} = w_{7-10}^{yz} = w_{15-18}^{zx} = w_{7-14}^{zx} = 0$.

2.2.2 Body Force

The LB equation in Eq. (2.35) is used to solve the continuity and Navier-Stokes equations without the influence of an external body force. To allow external force to enter the simulation, the forcing term needs to be incorporated. In this case the time evolution LB equation becomes

$$f_i(x + c_i, t + 1) = f_i - \frac{1}{\tau}(f_i - f_i^{eq}) + F_i. \quad (2.52)$$

The forcing term F_i is related to acceleration due to an external body force ρa . It has to satisfy the following constraints [73]

$$\sum_i F_i = 0, \quad (2.53)$$

$$\sum_i F_i c_{i\alpha} = F_\alpha, \quad (2.54)$$

$$\sum_i F_i c_{i\alpha} c_{i\beta} = F_\alpha v_\beta + F_\beta v_\alpha. \quad (2.55)$$

In our LB implementation, the choice of F_i which satisfy the above constraints is given by

$$F_i = 3w_i[(c_{i\alpha}a_\alpha - v_\alpha a_\alpha) + 3c_{i\alpha}c_{i\beta}v_\alpha a_\beta]. \quad (2.56)$$

In our simulation, the acceleration a becomes the simulation parameter that controls the strength of the external force.

2.2.3 Cahn-Hilliard Equation

It is worth mentioning that the Navier-Stokes equation describes the evolution of all of the fluid components represented by a single entity in the density ρ . However, the evolution of the other two order parameters is yet to be described. To do this, we use two Cahn-Hilliard equations for each of the order parameters:

$$\partial_t \phi + \partial_\alpha(\phi v_\alpha) = M_\phi \nabla^2 \mu_\phi, \quad (2.57)$$

$$\partial_t \psi + \partial_\alpha(\psi v_\alpha) = M_\psi \nabla^2 \mu_\psi, \quad (2.58)$$

where M is the mobility parameter. These equations allow the order parameters to evolve via advection and diffusion. These equations can also be solved using two LB equations using two

particle distribution function g_i and k_i which are similar to Eq. (2.35)

$$g_i(x + c_i, t + 1) = g_i - \frac{1}{\tau_\phi}(g_i - g_i^{eq}), \quad (2.59)$$

$$k_i(x + c_i, t + 1) = k_i - \frac{1}{\tau_\psi}(k_i - k_i^{eq}). \quad (2.60)$$

However, the equilibrium particle distribution functions g^{eq} and k^{eq} need to satisfy different constraints as follow,

$$\sum_i g_i^{eq} = \phi; \quad \sum_i g_i^{eq} c_{i\alpha} = \phi v_\alpha; \quad \sum_i g_i^{eq} c_{i\alpha} c_{i\beta} = \Gamma_\phi \mu_\phi \delta_{\alpha\beta} + \phi v_\alpha v_\beta; \quad (2.61)$$

$$\sum_i k_i^{eq} = \psi; \quad \sum_i k_i^{eq} c_{i\alpha} = \psi v_\alpha; \quad \sum_i k_i^{eq} c_{i\alpha} c_{i\beta} = \Gamma_\psi \mu_\psi \delta_{\alpha\beta} + \psi v_\alpha v_\beta. \quad (2.62)$$

Here, M , Γ and τ are connected to the following relations

$$M_\phi = \Gamma_\phi \left(\tau_\phi - \frac{1}{2} \right); \quad M_\psi = \Gamma_\psi \left(\tau_\psi - \frac{1}{2} \right). \quad (2.63)$$

In our LB implementation, the choice of g^{eq} and k^{eq} for $i > 0$ are given by

$$g_i^{eq} = w_i \left(\frac{\Gamma_\phi \mu_\phi}{c_s^2} + \frac{\phi e_{i\alpha} v_\alpha}{c_s^2} + \frac{\phi v_\alpha v_\beta (e_{i\alpha} e_{i\beta} - c_s^2 \delta_{\alpha\beta})}{2c_s^4} \right), \quad (2.64)$$

$$k_i^{eq} = w_i \left(\frac{\Gamma_\psi \mu_\psi}{c_s^2} + \frac{\psi e_{i\alpha} v_\alpha}{c_s^2} + \frac{\psi v_\alpha v_\beta (e_{i\alpha} e_{i\beta} - c_s^2 \delta_{\alpha\beta})}{2c_s^4} \right), \quad (2.65)$$

The equilibrium distribution functions for $i = 0$ are obtained by ensuring conservation of ϕ and ψ . Using similar procedures to recover the Navier-Stokes equation, the collision and propagation steps are also done iteratively for particle distribution functions g_i and k_i in order to solve the Cahn-Hilliard equations.

2.2.4 Boundary Conditions

In LB simulation, there are two types of boundary conditions that need to be implemented to mimic the experiment. The first one is the wetting boundary condition that dictates the interaction of the solid surface with the fluid phase. This effectively sets the corresponding contact angles for each phase. In the LB simulations carried out in this thesis, we use linear wetting potential, hence the corresponding wetting boundary condition must be satisfied.

It can be noticed that the construction of the generalised pressure tensor Eq. (2.47) does not involve the wetting potential. Instead, the wetting potential is incorporated in the simulation by setting up the boundary condition as the surface nodes by following Eq. (2.24). The implementation of these boundary conditions is done when the gradients of the order parameters are calculated at the solid boundary. From our variable transformation, the wetting boundary condition is given by

$$\nabla_{\perp}\rho_s = \frac{h_1}{\alpha^2\kappa_1} + \frac{h_2}{\alpha^2\kappa_2} + \frac{h_3}{\alpha^2\kappa_3}, \quad \nabla_{\perp}\phi_s = \frac{h_1}{\alpha^2\kappa_1} - \frac{h_2}{\alpha^2\kappa_2}, \quad \nabla_{\perp}\psi_s = \frac{h_3}{\alpha^2\kappa_3}. \quad (2.66)$$

As seen in Eqs. (2.51), (2.64) and (2.65), the gradient and the Laplacian of the density order parameters are needed to calculate the equilibrium distribution functions. Using finite difference method, taking the z direction as an example, they are evaluated as

$$\partial_z\rho_{ijk} = (\rho_{ij(k+1)} - \rho_{ij(k-1)})/2, \quad (2.67)$$

$$\partial_{zz}\rho_{ijk} = (\rho_{ij(k+1)} + \rho_{ij(k-1)} - 2\rho_{ijk}). \quad (2.68)$$

Here we have assumed that the lattice spacing is unity. Equivalent finite difference schemes can be used for ϕ and ψ for the x and y directions.

Now, suppose our system of interest is bounded by a flat solid surface, as illustrated in Fig. 2.3. At fluid nodes ($z \geq 2$), calculation of the gradient and the laplacian are possible

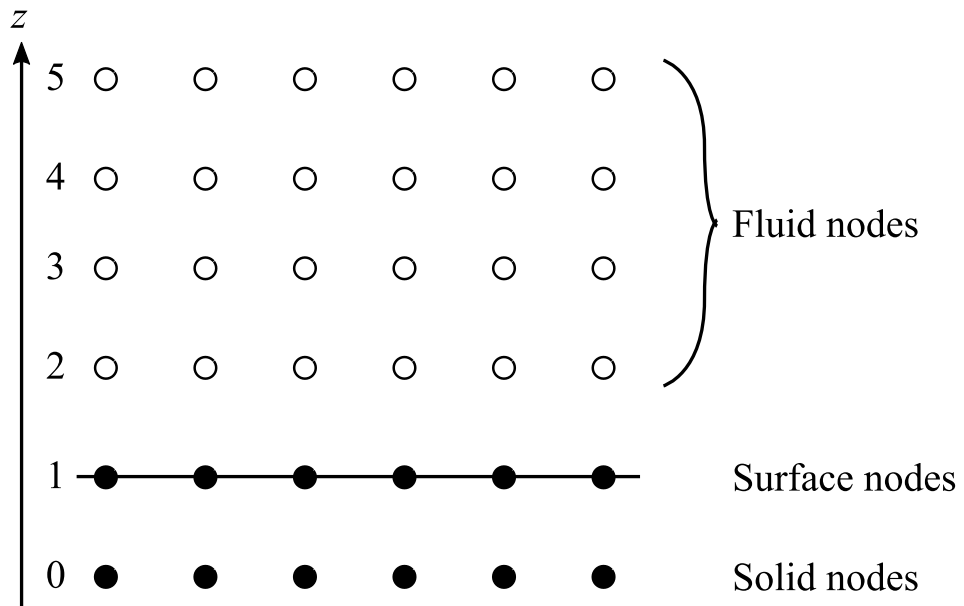


Figure 2.3: Illustration of lattice nodes configuration of a flat solid surface.

since the value of the order parameters at the neighbouring nodes are accessible. However, at surface nodes ($z = 1$), the calculation of the gradient and the laplacian will require the value of the order parameters at the solid nodes ($z = 0$), which is unavailable. Instead, the gradient calculation should be replaced by Eq. (2.66). Thus, for example,

$$\partial_z \rho_{ij1} = \nabla_{\perp} \rho_s = \frac{h_1}{\alpha^2 \kappa_1} + \frac{h_2}{\alpha^2 \kappa_2} + \frac{h_3}{\alpha^2 \kappa_3}, \quad (2.69)$$

$$\partial_{zz} \rho_{ij1} = 2(\rho_{ij2} - \rho_{ij1} - \nabla_{\perp} \rho_s) = 2\left(\rho_{ij2} - \rho_{ij1} - \left(\frac{h_1}{\alpha^2 \kappa_1} + \frac{h_2}{\alpha^2 \kappa_2} + \frac{h_3}{\alpha^2 \kappa_3}\right)\right) \quad (2.70)$$

The second boundary condition is the no-slip boundary condition which ensures the fluid velocity at the solid boundary is the same as the velocity of the solid boundary. This boundary condition is commonly observed in experiments and is part of basic assumptions in fluid mechanical problems such as viscous channel flow. Therefore, setting up this boundary condition correctly will allow us to benchmark the simulation with simple problems, such as Poiseuille flow or Couette flow.

In LB simulation, the no-slip boundary condition is implemented by applying bounce back rule during the propagation step for f_i towards the surface nodes. This means that the particle distribution functions that are propagated to a solid node will be reflected back to the original node. This process is illustrated in Fig. 2.4.

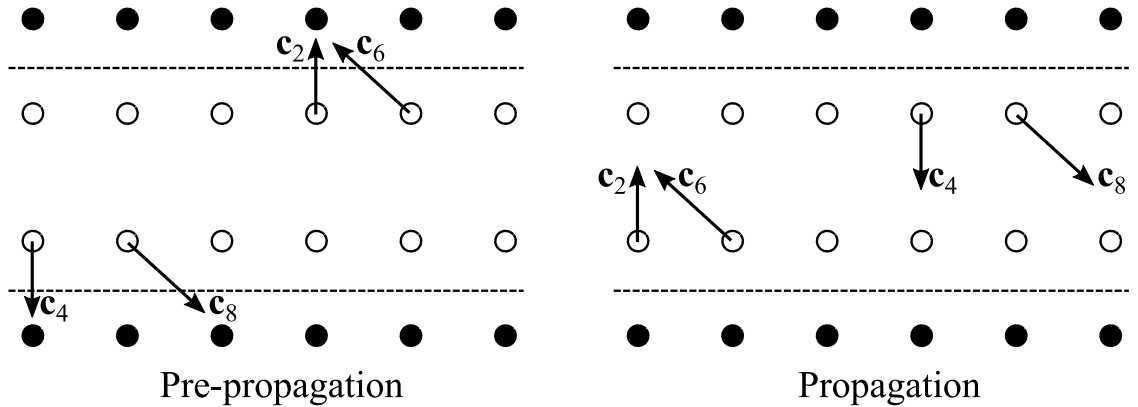


Figure 2.4: Illustration of how the no-slip boundary condition is achieved by implementing the bounce back rule such that if f_i is propagated in the direction of c_i , it will be reflected back in the direction of $-c_i$.

2.3 The Phase Field Energy Minimisation Method

The LB method offers great features for studying wetting phenomena. This method allows us to capture the static and dynamic properties of the system. However, this method requires considerable computational power. There are instances where the static properties of the system are the main interest, such as when we want to study the wetting states for different liquid combinations or to investigate the static contact angles. If the process of how the system reaches the equilibrium is not part of the main interest, nor the effect of external body force and fluid viscosity, using LB method will be a waste of computational power.

Another way to study the equilibrium properties of wetting systems is to use a minimisation algorithm such as the limited-memory Broyden-Fletcher-Goldfarb-Shanno (L-BFGS) algorithm [79]. This method can be used to find the configuration that corresponds to the minimum energy state of the system [54, 80]. Since this algorithm does not account for the dynamic of the system, it is around 1000 times faster when compared to the lattice Boltzmann method in finding the minimum total free energy.

In principle, the L-BFGS method works by iteratively increasing or decreasing the value of the variables of a function until the minimum value of the function is obtained. In our case, the variables are the fluid densities C_m 's. At each iteration, the algorithm will decrease or increase the values of C_m 's of every node depending on the gradient of the total free energy with respect to C_m at that particular node. Negative gradient means the total free energy can be reduced by increasing the value of C_m at that particular node, and vice versa. Please note that the gradient of the total free energy is calculated with respect to the fluid density, and is not to be confused with the spatial gradient. From the gradient, the fluid density is updated iteratively until the minimum total free energy is achieved.

2.3.1 The Total Free Energy Calculation

The L-BFGS method used the same free energy model used for the LB method, which is given in Eq. (2.1). However, there are several differences in how we implement the calculations. Here, we use the constraint $C_1 + C_2 + C_3 = 1$ to define $C_3 = 1 - C_1 - C_2$ to reduce the number of variables that needs to be optimised. Also, we use the cubic wetting potential to control the surface free energy and hence the contact angle. Lastly, the integral in Eq. (2.1) becomes a summation over all of the contributing nodes. Thus, the total free energy is calculated as the

following,

$$\Psi = \sum_{ijk}^V [\Psi_{bulk} + \Psi_{interface}] + \sum_{ijk}^S \Psi_{surface}, \quad (2.71)$$

where,

$$\Psi_{bulk} = \sum_{m=1}^3 \frac{\kappa_m}{2} (C_m|_{ijk})^2 (1 - C_m|_{ijk})^2, \quad (2.72)$$

$$\Psi_{interface} = \sum_{m=1}^3 \frac{\alpha^2 \kappa_m}{2} (\nabla C_m|_{ijk})^2, \quad (2.73)$$

$$\begin{aligned} \Psi_{surface} = & -\alpha(\kappa_1 + \kappa_3) \cos \theta_{13} \left(\frac{1}{2} (C_1|_{ijk})^2 - \frac{1}{3} (C_1|_{ijk})^3 \right) \\ & -\alpha(\kappa_2 + \kappa_3) \cos \theta_{23} \left(\frac{1}{2} (C_2|_{ijk})^2 - \frac{1}{3} (C_2|_{ijk})^3 \right). \end{aligned} \quad (2.74)$$

As a reminder, the subscript m is to indicate the fluid phase, while i, j and k are to indicate the spatial dimensions in the x, y and z directions respectively.

To clarify the calculation of the total free energy, consider the visualisation of the simulation nodes illustrated in Fig. 2.5. In this setup, the size simulation box used is $LX \times LY \times LZ \times = 20 \times 1 \times 10$. At the initialisation step, we label every node as either a fluid node or solid node. Then, we relabel the solid nodes that have an interface with fluid nodes as surface nodes. The V in Eq. (2.71) indicates that summation is carried out over bulk fluid nodes and surface nodes, whereas S indicates that it is done over surface nodes only. The solid nodes do not contribute to the total free energy calculation.

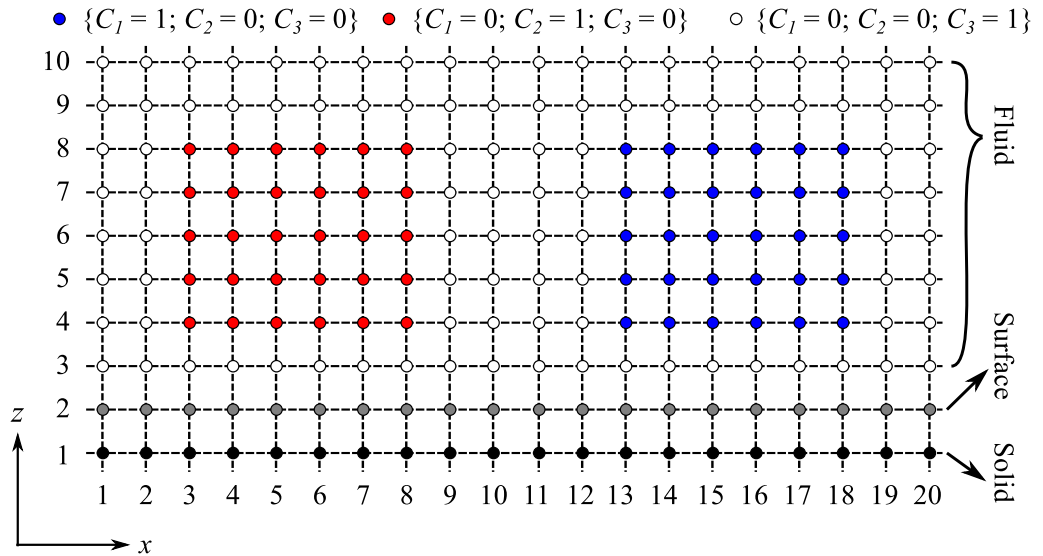


Figure 2.5: Illustration of the matrix for simulation.

The spatial gradient of the fluid phase density $\nabla C_m|_{ijk}$ is calculated by finite difference

method

$$\nabla C_m|_{ijk} = \partial_x C_m|_{ijk} \hat{\mathbf{i}} + \partial_y C_m|_{ijk} \hat{\mathbf{j}} + \partial_z C_m|_{ijk} \hat{\mathbf{k}}, \quad (2.75)$$

with

$$\partial_z C_m|_{ijk} = \frac{C_m|_{ij(k+1)} - C_m|_{ij(k-1)}}{2\Delta z}, \quad (2.76)$$

The squared of the spatial gradient, which is needed to compute $\Psi_{interface}$, is calculated using the second order finite difference as the following

$$(\nabla C_m|_{ijk})^2 = (\partial_x C_m|_{ijk})^2 + (\partial_y C_m|_{ijk})^2 + (\partial_z C_m|_{ijk})^2 \quad (2.77)$$

with

$$(\partial_z C_m|_{ijk})^2 = \frac{(C_m|_{ijk} - C_m|_{ij(k-1)})^2 + (C_m|_{ijk} - C_m|_{ij(k+1)})^2}{2\Delta z}, \quad (2.78)$$

and similarly for the x and y directions. This scheme is used to avoid the checkerboard instability [80]. However, this choice is not available for calculating gradient to the direction perpendicular to the surface, e.g. at node $\{10,1,2\}$ in Fig. 2.5. In this case, the squared gradient in z direction is calculated using forward difference such as

$$(\partial_z C_m|_{ijk})^2 = \left(\frac{C_m|_{ijk} - C_m|_{ij(k+1)}}{\Delta z} \right)^2. \quad (2.79)$$

2.3.2 Calculating the Gradient of the Total Free Energy

In order to achieve the minimum total free energy configuration, the value of the fluid density at every node needs to be updated. The gradient of the total free energy with respect to the fluid density at every node ($\partial\Psi/\partial C_m|_{ijk}$) is used to determine the direction of the update, either to increase or to decrease the value of $C_m|_{ijk}$.

The calculation of the gradient is straightforward for Ψ_{bulk} and $\Psi_{surface}$ in Eq. (2.71), since they are local in C_m . However, one needs to be careful when calculating the gradient of $\Psi_{interface}$ since it requires the information from the neighbouring nodes. To demonstrate the gradient calculation, we will calculate $\partial\Psi/\partial C_m|_{ijk}$ for the nodes away from the solid nodes and for the nodes next to the solid nodes. To simplify the demonstration, let us assume that the system is one dimensional and consists of only one fluid phase (Fig. 2.6). Also, we will only consider the contribution from the $\Psi_{interface}$ terms.

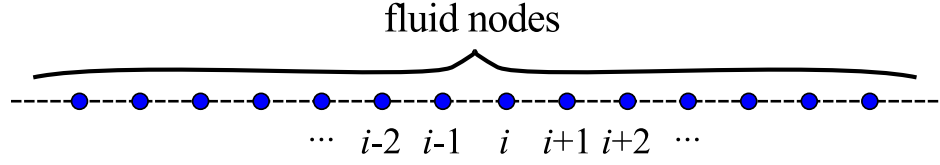


Figure 2.6: One dimensional fluid nodes system.

Using Eq. (2.73), the total free energy is given by

$$\begin{aligned} \Psi = \dots + & \frac{\alpha^2 \kappa_1}{2} \frac{(C_1|_{(i-1)} - C_1|_{(i-2)})^2 + (C_1|_{(i-1)} - C_1|_i)^2}{2} + \\ & \frac{\alpha^2 \kappa_1}{2} \frac{(C_1|_i - C_1|_{(i-1)})^2 + (C_1|_i - C_1|_{(i+1)})^2}{2} + \\ & \frac{\alpha^2 \kappa_1}{2} \frac{(C_1|_{(i+1)} - C_1|_i)^2 + (C_1|_{(i+1)} - C_1|_{(i+2)})^2}{2} + \dots \end{aligned} \quad (2.80)$$

Here, we have use $\Delta x = 1$. We can see that $C_1|_i$ also appears for the calculation of Ψ at $(i-1)$ and at $(i+1)$. Hence, when evaluating the gradient of the total free energy with respect to $C_1|_i$, we have to consider the contribution from the adjacent nodes as follows

$$\begin{aligned} \frac{\partial \Psi}{\partial C_1|_i} = & -\alpha^2 \kappa_1 (C_1|_{(i-1)} - C_1|_i)/2 \\ & + \alpha^2 \kappa_1 (2C_1|_i - C_1|_{(i-1)} - C_1|_{(i+1)})/2 \\ & - \alpha^2 \kappa_1 (C_1|_{(i+1)} - C_1|_i)/2. \end{aligned} \quad (2.81)$$

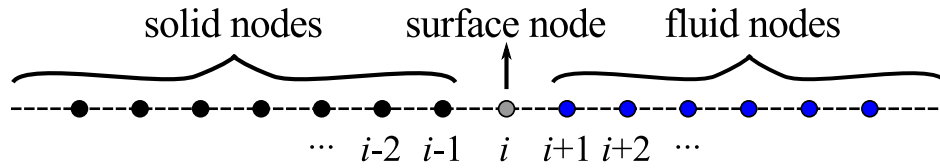


Figure 2.7: One dimensional system containing fluid, surface and solid nodes.

The configuration of nodes next to the solid nodes is shown in Fig. 2.7. As we can see here, the nodes before node i are solid nodes, hence do not contribute to the total free energy calculation. Node i and the nodes afterward, however, are surface node and fluid nodes

respectively. In this case, the contribution of $\Psi_{interface}$ to the total free energy is given by

$$\begin{aligned} \Psi = & \frac{\alpha^2 \kappa_1}{2} (C_1|_i - C_1|_{(i+1)})^2 + \\ & \frac{\alpha^2 \kappa_1}{2} \frac{(C_1|_{(i+1)} - C_1|_i)^2 + (C_1|_{(i+1)} - C_1|_{(i+2)})^2}{2} + \\ & \frac{\alpha^2 \kappa_1}{2} \frac{(C_1|_{(i+2)} - C_1|_{i+1})^2 + (C_1|_{(i+2)} - C_1|_{(i+3)})^2}{2} + \dots \end{aligned} \quad (2.82)$$

Hence, the gradient is written as

$$\frac{\partial \Psi}{\partial C_1|_i} = \alpha^2 \kappa_1 (C_1|_i - C_1|_{(i+1)}) - \alpha^2 \kappa_1 (C_1|_{(i+1)} - C_1|_i) / 2. \quad (2.83)$$

These two cases are the building blocks for calculating $\partial \Psi / \partial C_m|_{ijk}$. Eqs. (2.81) and (2.83) are the analytical form for the gradient of Ψ . One way to check that the gradient calculation has been implemented correctly is by comparing it with the numerical gradient

$$\frac{\partial \Psi}{\partial C_1|_i} = \frac{\Psi(C_1|_i + \Delta C) - \Psi(C_1|_i - \Delta C)}{2\Delta C}, \quad (2.84)$$

where ΔC is a small quantity. If Eq. (2.81) and Eq. (2.83) are in a good agreement with Eq. (2.84), then the analytical form of the gradient has been implemented correctly.

2.4 Benchmark

It is important to make sure that our simulation tools can correctly capture the physics of our system of interest. To do that, we performed simulations of simple setups such as fluid flow in a channel and sessile droplet on a flat solid surface. The channel flow or Poiseuille flow (Fig. 2.8) is one of the simplest cases where the solution of the Navier-Stokes can be obtained analytically to determine the velocity profile of the fluid flow in the channel. Similarly, the equilibrium shape of a droplet on a flat solid surface represents many thermodynamic parameters. Hence, having an agreement between simulation results and theory is ensuring that the thermodynamic properties are represented correctly in our simulations.

For the channel flow, suppose an incompressible fluid is flowing in a 2-dimensional channel under the influence of an external body force as illustrated in Fig. 2.8. The equations of motion are given by the Navier-Stokes equations, as shown in Eq. (2.30). The external body force appears as an additional term to the RHS of Eq. (2.30) as ρa , where a is the acceleration

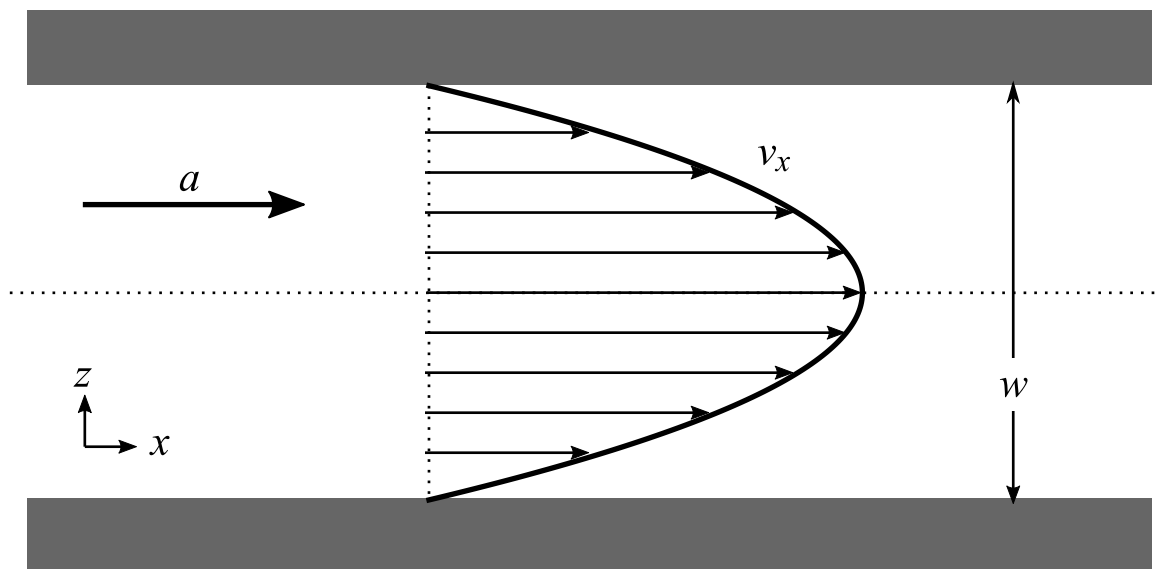


Figure 2.8: Illustration of fluid flow in a two dimensional channel under the influence of a body force a in the positive x direction. w and v_x are the width of the channel and the fluid velocity in the x direction respectively.

due to the body force. Since the fluid is incompressible and homogeneous, $\partial_t \rho = 0$ and $\partial_\gamma \rho = 0$. When the flow is fully developed the fluid velocity is steady over time, thus $\partial_t v_\gamma = 0$. Moreover, since the acceleration due to body force a is only in the x direction, we have $v_z = 0$. Thus the equation of motion becomes

$$\partial_{zz} v_x = -\frac{\rho a}{\eta}, \quad (2.85)$$

and is subject to the no-slip boundary conditions $v_x(z=0) = 0$ and $v_x(z=w) = 0$. The solution for this differential equation is the velocity profile of the flow, which is given by

$$v_x(z) = \frac{\rho a}{2\eta} z(w-z). \quad (2.86)$$

Fig. 2.9 shows the comparison between the simulation results and the theoretical predictions. The agreement between simulation and theory confirms that our LB algorithm and the forcing method have been implemented correctly. Further, the results also confirm that the two physical parameters tested in this setup, body force and fluid viscosity, can be represented correctly in our simulations.

As mentioned earlier that LIS system consists of more than one fluids. Hence, we test our LB simulation code further by having a channel flow with multiphases. Fluid phase 1 with viscosity η_1 is flowing at the lower half of the channel, while fluid phase 2 with viscosity η_2 is

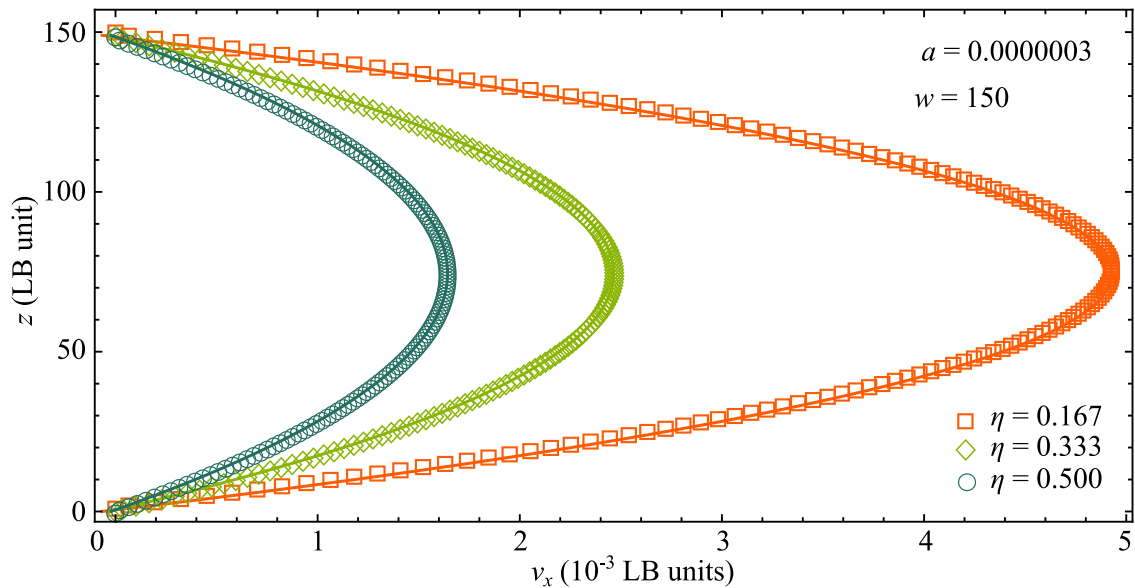


Figure 2.9: The simulation results for fluid flow in a channel for different fluid viscosities η . The simulations were performed using the LB method. The velocity profiles show an excellent agreement between theory (lines) and simulations (data points).

flowing at the upper half. Thus the solution for Eq. (2.85) becomes

$$v_{x1} = -\frac{\rho a}{2\eta_1} z^2 + Az + B, \quad (2.87)$$

$$v_{x2} = -\frac{\rho a}{2\eta_2} z^2 + Cz + D, \quad (2.88)$$

where v_{x1} and v_{x2} respectively are the fluid velocity at the lower and the upper halves. The constants A, B, C and D are to be determined by using the no-slip boundary conditions ($v_{x1} = 0$ at $z = 0$ and $v_{x2} = 0$ at $z = w$), and employing the continuous flow condition, which demands $v_{x1} = v_{x2}$ and $\eta_1 \partial_z v_{x1} = \eta_2 \partial_z v_{x2}$ at $z = w/2$.

For this test, we varied the viscosity of the upper fluid while keeping the viscosity of the lower fluid. The analytical solution for the multiphase Poiseuille flow and its comparison with our simulation are presented in Fig. 2.10. As can be seen, the simulation data points are on top of the theoretical lines.

For droplet on a flat solid surface, the physical parameters involved are the fluid-fluid and fluid-solid interfacial tensions, and the equilibrium contact angle, as described by the Young's equation. In our simulations, these physical quantities are controlled by the simulation parameters κ 's and h 's for the LB simulations, and κ 's and θ 's for the L-BFGS method. The simulation setup and simulation results are shown in Fig. 2.11(a). We can see that the droplet

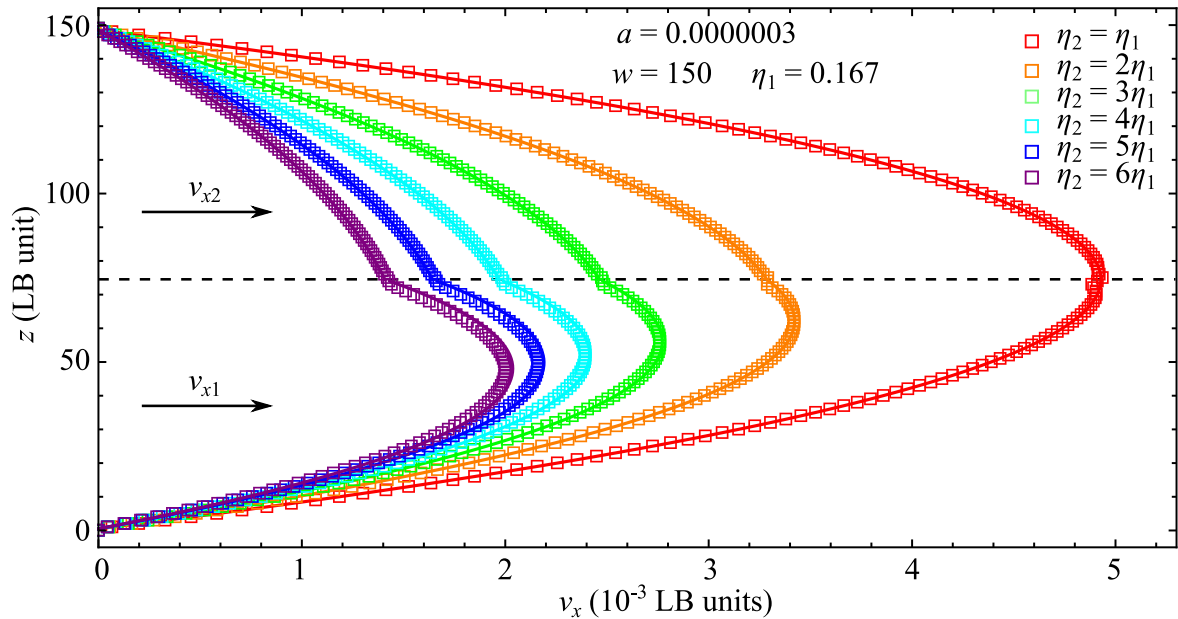


Figure 2.10: The simulation results for two-phases fluid flow in a channel for different fluid viscosities. The velocity profiles show an excellent agreement between theory and simulations where the data points are on top of the theoretical lines.

contact angles measured from the simulation results are in agreement with the prescribed values. We further simulate three fluid phases in a box to form the Neumann's angles, as shown in Fig. 2.11(b). These results confirm that the thermodynamic properties of the system can be captured correctly in our simulations using our free energy model.

2.5 Discussion

Our simulation methods offer many advantages for studying wetting phenomena such as the ability to manipulate surface textures and tune the solid and liquid interfacial properties. However, there are some limitations that need to be considered. First, the physics of the system depends on the prescribed model. For example, our lattice Boltzmann simulation is capable of simulating the dynamics of a fluid system as well as the effect of surface tension. However, other physics such as temperature and phase transformation is not incorporated in the model and thus, their effect cannot be studied using the current model. Also, finite size and finite difference calculation may become one of the source of errors which may affect the simulation results. Some simulations such as 3D simulations also demand excessive computational power. To obtain a meaningful conclusion, multiple simulations are often required, which could consume longer time and larger resources. There are several approaches to reduce

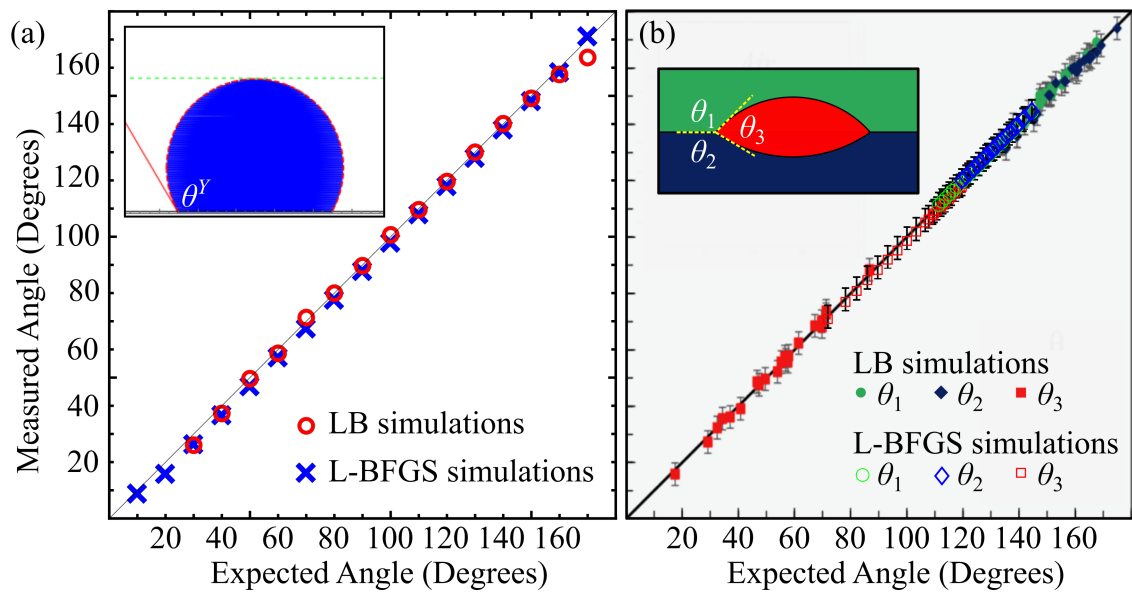


Figure 2.11: (a) Simulations of a liquid droplet on a flat surface. The values of the measured contact angles are in agreement with the prescribed values. The simulations were performed using the LB simulations and the L-BFGS simulations where the former uses the linear wetting potential and the latter uses the cubic wetting potential. (b) Simulation of three fluid phases in a box. The Neumann angles measured are in agreement with the predicted values.

the computational cost and hence speed up the simulation time. These approaches include the quasi 3D setup, periodic boundary condition and incorporating the wetting boundary condition at the top of the simulation box, which will be discussed in the following chapters.

CHAPTER 3

Droplet Morphology and Droplet Mobility on Liquid Infused Surfaces

Liquid repellent surfaces have been long an attractive research interest for industries and academics. Various kind and mechanism of liquid repellent surfaces have been studied including smooth, defect-free surfaces, low surface energy materials, and superhydrophobic surfaces. On the other hand, liquid infused surfaces (LIS), is relatively a new field of research. The excellent liquid repellency arises when the presence of an immiscible liquid in surface roughness can reduce the adherence of the other liquid on the solid surfaces.

LIS were first introduced by Wong *et al.* in 2011. They fabricated the omni-repellent surfaces by infusing Teflon nano-fibers with FC70 lubricant, which is immiscible with both aqueous and hydrocarbon fluids [58]. In 2013, Smith *et al.* argued that the application of LIS by Wong *et al.* is limited due to the hazardous nature of FC70 lubricant [57]. Employing different lubricant, however, is sometimes not possible because the lubricant may not fully wet the solid so that it is unable to give proper lubrication. Using thermodynamic analysis, Smith *et al.* proposed different wetting states of a droplet on LIS system [57]. They also demonstrate that introducing secondary roughness to the solid texture can significantly increase the liquid repellency even if the lubricant only partially wets the solid [57].

In 2015, Schellenberger *et al.* confirmed the wetting states proposed by Smith *et al.* using laser confocal microscopy [64]. They also demonstrated that the apparent contact angle of a droplet on LIS can be very different depending on the type of the lubricant. This was later explained by Sempregon *et al.* in 2016. Using geometrical analysis, Sempregon *et al.* proposed the relation of the droplet apparent contact angle on LIS with the surface tensions,

the wetting angles and the size of the meniscus [67]. For the droplet dynamics, Keiser *et al.* in 2017 reported two distinct regimes of droplet mobility depending on the viscosity of the droplet and the lubricant [69]. Build upon these findings, we present a computational method to study the LIS system. To the best of our knowledge, this was the first computational study of LIS system. The methods presented in this thesis is expected to be a complement to the experimental methods and as an alternative method for those who are limited with the equipment to study LIS system experimentally.

In this chapter, we explain the simulation setup we used and the parameters we varied to study the LIS system. We then study the morphology of droplets on LIS and compare our simulation results with the theory proposed by Semprebon *et al.*. Further, we also reproduce the experimental procedure presented by Keiser *et al.* to study the droplet mobility for various droplet and lubricant viscosities. These comparisons, with theory and experiments, validate our simulation results and gives confidence in the accuracy of the results.

3.1 Simulation Setup

The simulation method employed in this chapter is the lattice-Boltzmann (LB) method. To conserve computational power, simulations are performed in a quasi three-dimensional simulation box. This quasi 3D setup has the advantage of reducing the computational cost when compared to a full 3D simulation while capturing the key 3D features. In the case of LIS, it preserves the essential feature of allowing the lubricant to flow in between the surface texture underneath the liquid droplet. This setup has been successfully employed to study droplet dynamics on flat and on superhydrophobic surfaces [73, 81, 82].

The simulation setup is shown in Fig. 3.1. The dimension of the simulation box is $400 \times 10 \times 150$ LB units with the top surface bounded by a flat wall. The bottom solid surface is textured with a row of square posts of height $h = 10$ LB units, width $a = 5$ LB units, and periodicity $p = 10$ LB units. A periodic boundary condition is applied in the other two directions. Except stated otherwise, most simulations presented in this chapter were performed using this quasi 3D setup.

The lubricant phase is initialised to fill the space between the posts and an additional layer of two lattice nodes on top of them, in order to allow the formation of a lubricant ridge at the two sides of the droplet. To make sure the lubricant imbibes the bottom surface, the lubricant-

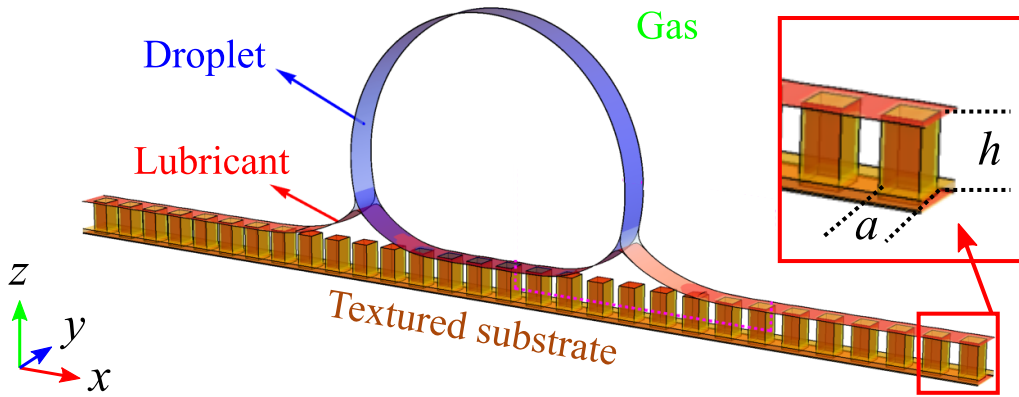


Figure 3.1: Rendering of a quasi 3D setup of a LIS system where a droplet is sitting on a textured substrate infused with a lubricant. h and a are the height and width of the posts.

droplet contact angle θ_{ld} and the lubricant-gas contact angle θ_{lg} have to be smaller than the critical angle θ_c so that the lubricant can hemiwick the textured surface. From thermodynamic considerations it can be shown that $\cos \theta_c = (1 - \varphi_s)/(r - \varphi_s)$, where φ_s and r are respectively the solid fraction and roughness factor of the surface pattern [16, 17]. The texture employed in this work gives $\varphi_s = 0.25$ and $r = 3$, which leads to $\theta_c \approx 74^\circ$. A hemispherical droplet with radius $R = 60$ LB units (Fig. 3.2) is placed on top of the posts and is then allowed to reach equilibrium.

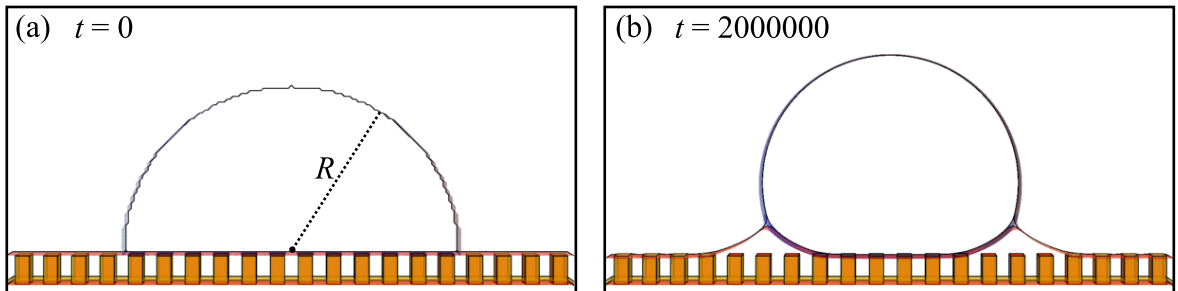


Figure 3.2: The droplet (a) initial and (b) final shape after 2000000 iterations. R is the initial droplet radius.

3.2 Droplet Morphologies in Mechanical Equilibrium

In this subsection we will demonstrate that our ternary LB approach can accurately simulate droplet morphologies in mechanical equilibrium on LIS. For a liquid droplet placed on an ideal smooth surface, the material contact angle, θ_{dg}^Y , is given by the Young's law [7], which arises

from the force balance between the interfacial tensions at the three-phase contact line:

$$\cos \theta_{dg}^Y = \frac{\gamma_{sg} - \gamma_{sd}}{\gamma_{dg}}, \quad (3.1)$$

where γ_{sg} , γ_{sd} , and γ_{dg} are the solid-gas, solid-droplet and droplet-gas interfacial tensions respectively. Here we employ the superscript Y to distinguish the material contact angle from the effective contact angle under the Cassie-Baxter approximation (superscript CB).

For a droplet placed on LIS, the solid-gas-droplet contact line does not exist, and thus Eq. (3.1) does not represent a physically meaningful condition. In this study we focus on the case where the lubricant is partially wetting the solid ($\theta_{lg}, \theta_{ld} > 0$) and does not cloak the droplet. As such, there are three alternative three-phase lines (see Fig. 3.3): droplet-lubricant-gas, droplet-lubricant-solid, gas-lubricant-solid.

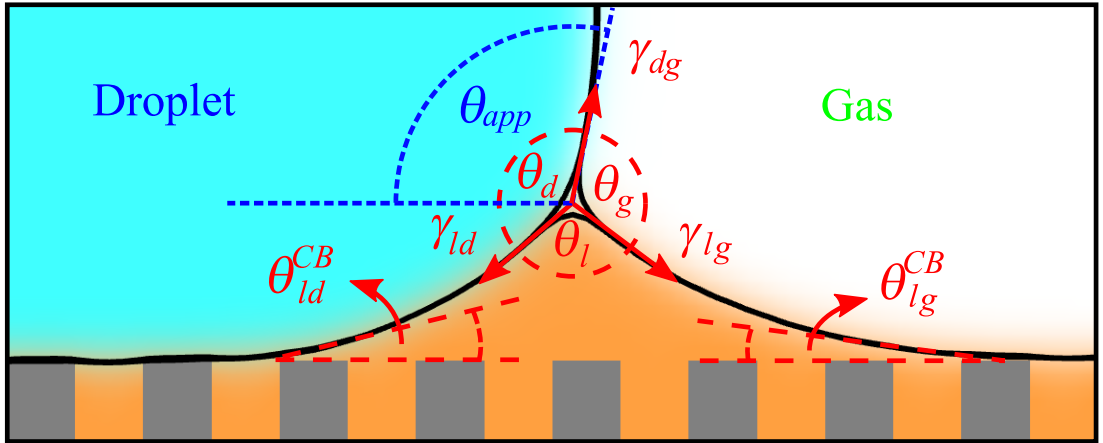


Figure 3.3: Magnification of the lubricant ridge. γ_{dg} , γ_{lg} , and γ_{ld} are the droplet-gas, lubricant-gas, and droplet-lubricant surface tensions; θ_d , θ_g , and θ_l are the Neumann angles of the droplet, gas and lubricant; θ_{ld}^{CB} and θ_{lg}^{CB} are the droplet-lubricant and lubricant-gas contact angles assuming a Cassie-Baxter approximation; and θ_{app} is the apparent contact angle.

To characterise how much the droplet spreads on LIS, it is useful to introduce the notion of an apparent contact angle θ_{app} . The apparent angle can be defined with respect to the horizontal plane at the droplet-lubricant-gas triple line, as shown in Fig. 3.3. In the limit of small but finite lubricant ridge, Semprebon *et al.* have recently shown that the apparent angle need to satisfy the following relation [67]:

$$\frac{\sin \theta_g [\cos \theta_{ld}^{CB} - \cos(\theta_d - \theta_{app})]}{\sin \theta_d [\cos \theta_{lg}^{CB} - \cos(\theta_{app} + \theta_g)]} = \left(1 - \frac{\Delta P_{dg}}{\Delta P_{lg}} \right). \quad (3.2)$$

Here $\theta_{\alpha\beta}^{CB}$ is the averaged wettability expressed by the Cassie-Baxter contact angle,

$$\cos \theta_{\alpha\beta}^{CB} = \varphi_s \cos \theta_{\alpha\beta}^Y + (1 - \varphi_s), \quad (3.3)$$

which accounts for the fact that the droplet and gas phases lie on top of a composite solid-lubricant interface. The quantity $\Delta P_{dg}/\Delta P_{lg}$ is the ratio between the Laplace pressures at the droplet-gas and lubricant-gas interfaces. Since the Laplace pressure is given by

$$\Delta P_{\alpha\beta} = \frac{\gamma_{\alpha\beta}}{R_{\alpha\beta}}, \quad (3.4)$$

where $R_{\alpha\beta}$ is the mean radius of curvature for the $\alpha\beta$ interface, $\Delta P_{dg}/\Delta P_{lg}$ is directly related to the size ratio between the lubricant ridge and the droplet. In the strict limit of vanishing lubricant ridge, $\Delta P_{dg}/\Delta P_{lg} \rightarrow 0$, Eq. (3.2) can be simplified to

$$\cos \theta_{app} = \frac{\gamma_{lg}}{\gamma_{dg}} \cos \theta_{lg}^{CB} - \frac{\gamma_{ld}}{\gamma_{dg}} \cos \theta_{ld}^{CB}. \quad (3.5)$$

The main advantage of Eq. (3.5) is that all variables on the right hand side are material parameters which can be measured independently. In contrast, the value of $\Delta P_{dg}/\Delta P_{lg}$ in Eq. (3.2) is usually not known a priori. However, it can be inferred from analysing the shape of the lubricant ridge. We then compare the apparent angle obtained from our LB simulations once mechanical equilibrium is reached, against both the full solution in Eq. (3.2) and the vanishing lubricant ridge approximation in Eq. (3.5).

To compare the simulation results with the predicted values, we need to measure θ_{app} when the simulations reach mechanical equilibrium. The apparent contact angle is evaluated by calculating the equilibrium droplet radius R_{dg} , the droplet height h_d and the meniscus height h_m . These values are obtained from the simulation results. By analysing the density of the fluids at every node, the fluid-fluid interfaces can be tracked and R_{dg} , h_d , and h_m can be measured. The apparent contact angle is then calculated as

$$\theta_{app} = 90^\circ - \sin^{-1} \left(\frac{R_{dg} - (h_d - h_m)}{R_{dg}} \right). \quad (3.6)$$

Fig. 3.4 illustrates how R_{dg} , h_d , and h_m are extracted from simulation to evaluate θ_{app} .

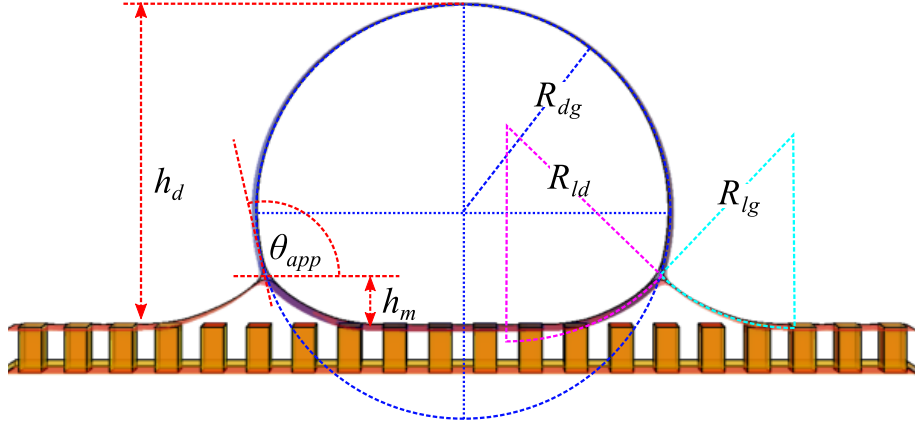


Figure 3.4: Geometrical analysis for contact angle measurement from the LB simulation results. The apparent contact angle is then calculated using Eq. (3.6).

The range of apparent angles are obtained by varying the surface tensions γ_{lg} , γ_{dg} and γ_{ld} , as well as the lubricant's material contact angles θ_{lg}^Y and θ_{ld}^Y . For comparison against the full solution, Eq. (3.2), we compute $\Delta P_{dg}/\Delta P_{lg}$ by measuring the radii of curvature of the droplet-gas and lubricant-gas interfaces once mechanical equilibrium is reached in our simulations.

The comparison between the simulation results and the theory is presented in Fig. 3.5. Respectively, the full solution and the vanishing lubricant ridge approximation is plotted in red hollow squares and green triangles respectively. The obtained apparent angles in our LB simulations are in very good agreement with the full solution. When compared against the vanishing lubricant ridge approximation Eq. (3.5), the obtained values of the apparent angle has a systematic deviation by several degrees. This deviation is expected since the size of the lubricant ridge in our simulations is not negligible compared to the droplet size. Nonetheless, Eq. (3.5) remains a good first estimate for predicting the apparent angle of a droplets on a LIS, and the accuracy improves the smaller the lubricant meniscus is compared to the droplet size.

Using our LB simulations and Eq. (3.5), it is also useful to demonstrate the effect of varying both the droplet and lubricant properties. Essentially, this is equivalent to choosing the droplet-lubricant combination. Schellenberger *et al.* demonstrated that water, decanol and glycerol have different apparent angles when placed on FC70 (a fluorinated oil) infused surfaces [64]. Here using our LB simulations, we can systematically vary the parameters in Eq. (3.5). In this attempt, we use the same lubricant wetting angles, both in the presence of

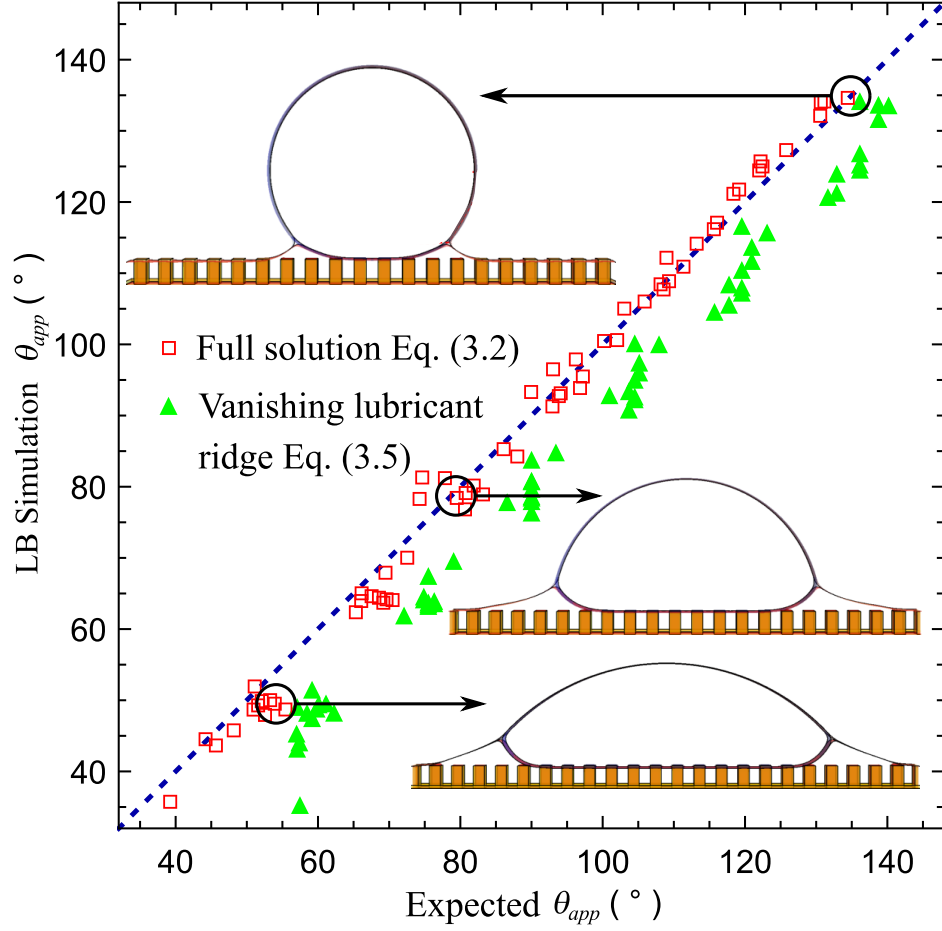


Figure 3.5: Comparison between θ_{app} obtained from our simulations against the predicted values from both the full solution Eq. (3.2) and the vanishing lubricant ridge approximation Eq. (3.5). The top left inset illustrates how θ_{app} is measured at the droplet-lubricant-gas triple line.

gas phase and droplet phase, $\theta_{lg} = \theta_{ld} = \theta_{wet}$. As such, we can modify Eq. (3.5) into

$$\cos \theta_{app} = \frac{\gamma_{lg} - \gamma_{ld}}{\gamma_{dg}} \cos \theta_{wet}^{CB}. \quad (3.7)$$

We can observe that the sign of the RHS in Eq. (3.7) depends on the numerator of the surface tensions ratio. When $\gamma_{lg} > \gamma_{ld}$, the sign is positive and the droplet will have a *hydrophilic*-like shape. On the contrary, when $\gamma_{lg} < \gamma_{ld}$, the droplet will have a *hydrophobic*-like shape. The denominator, on the other hand, reduces the magnitude of the surface tension ratio, regardless of the sign. The larger the γ_{dg} , the closer the surface tension ratio to 0, and thus, the closer θ_{app} to 90° . This is the reason why water droplet on LIS is often reported to have $\theta_{app} = 90^\circ$, since in this case, γ_{dg} is significantly larger than the lubricant surface tensions [57, 64, 69].

Fig. 3.6 shows different morphologies of liquid droplets on LIS with various surface tension

ratios and lubricant wetting angles. It shows that the more negative the surface tension ratio, the more hydrophobic the droplet shape. Compared to the surface tension ratio, the lubricant wetting angle θ_{wet} does not significantly affect the droplet shape. Instead, θ_{wet} influences the shape of the lubricant meniscus, especially for lower θ_{app} .

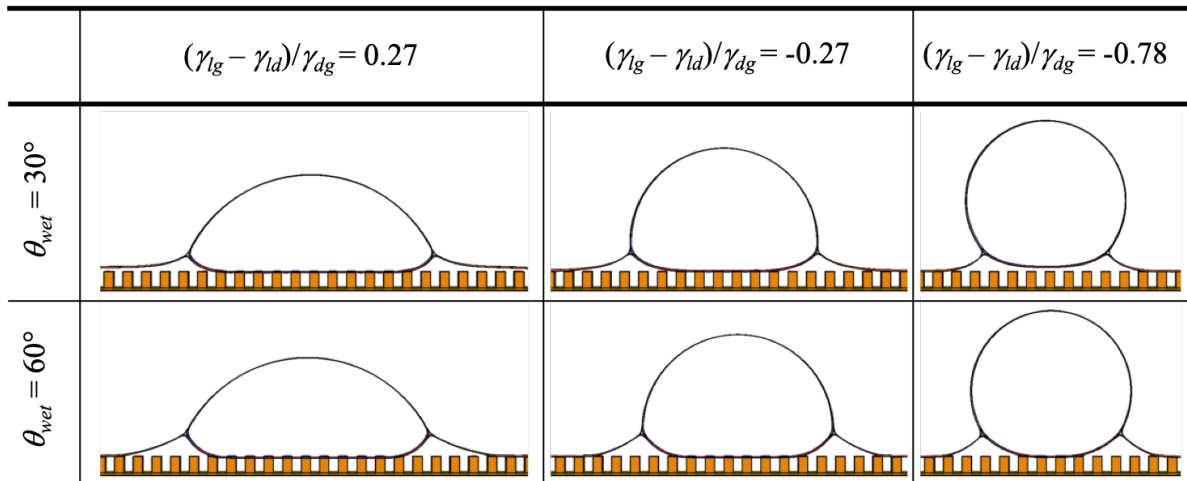


Figure 3.6: The morphology of liquid droplets on LIS with various surface tension ratios and lubricant wetting angles.

3.3 Droplet Mobility Under Influence of the Fluid Viscosities

A recent experiment by Keiser *et al.* suggests that there is a crossover between the bulk droplet and lubricant ridge dominated energy dissipation regimes, depending on the viscosity of the droplet and the lubricant [69]. Here we aim to reproduce this crossover behaviour to demonstrate that our LB simulation can correctly capture the dynamics of droplets moving across LIS.

To do this, we introduce body force to mobilise the droplet after it reaches the equilibrium state. Unless stated otherwise, we set the horizontal and the vertical components of body force to be equal, such that $G_z = -G_x$. This choice corresponds to an experimental setup where the substrate is tilted at an angle of 45° . Adding a downward body force ensures the droplet to remain attached to the substrate, especially when it has a large apparent angle. The typical droplet shape and the velocity profile is shown in Fig. 3.7.

Fig. 3.7(a) shows the droplet morphology when in motion due to an external driving force. We extract the droplet centre of mass velocity V by calculating the total momentum of the droplet divided by the total mass of the droplet. From Fig. 3.7(b), we notice that V is

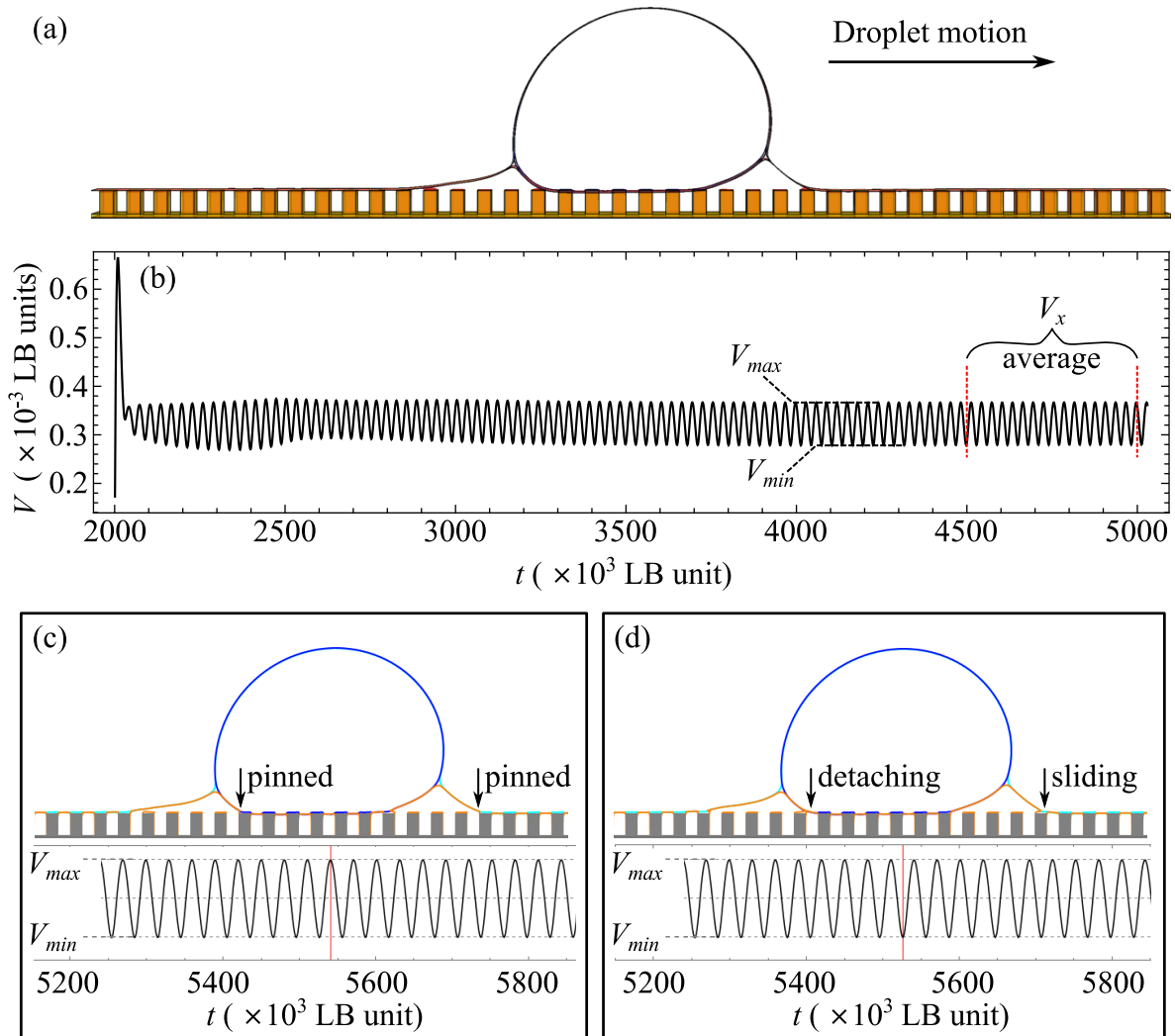


Figure 3.7: (a) A typical droplet shape during in motion under influence of body force. (b) The centre of mass droplet velocity exhibits an oscillation. (c-d) Upon closer inspection, the oscillation is linked to a series of (c) pinning and (d) depinning events as the droplet moves across the textured surface.

oscillating with time. We further evaluate the droplet morphology when at the top and at the bottom of the oscillation. At the top of the oscillation (Fig. 3.7(c)), we found that the decrease of the droplet velocity is related to the pinning events of the advancing lubricant-gas and lubricant-droplet interfaces. On the contrary, at the bottom of the oscillation (Fig. 3.7(d)), we observe that the droplet starts to gain velocity when the aforementioned contact lines are moving. These series of pinning-depinning events occur as the droplet move across the textured surface. The contact line pinning of a droplet on a LIS system and the effect of various parameters are systematically studied in Chapter 6.

Considering the effect of the contact line pinning, the droplet mobility is characterised

by the average velocity at steady state V_x , where the oscillation becomes stable. We find V_x to be insensitive to the value of G_z as long as the droplet size is smaller than the capillary length, $R < l_c = \sqrt{\gamma_{dg}/\rho|G_z|}$. To characterise the droplet mobility, we will take advantage of a dimensionless parameter, the Bond number $Bo = \Delta(\rho G_x)R^2/\gamma_{dg}$ where R and γ_{dg} are the initial droplet radius as shown in Fig. 3.2 and the droplet-gas surface tension respectively.

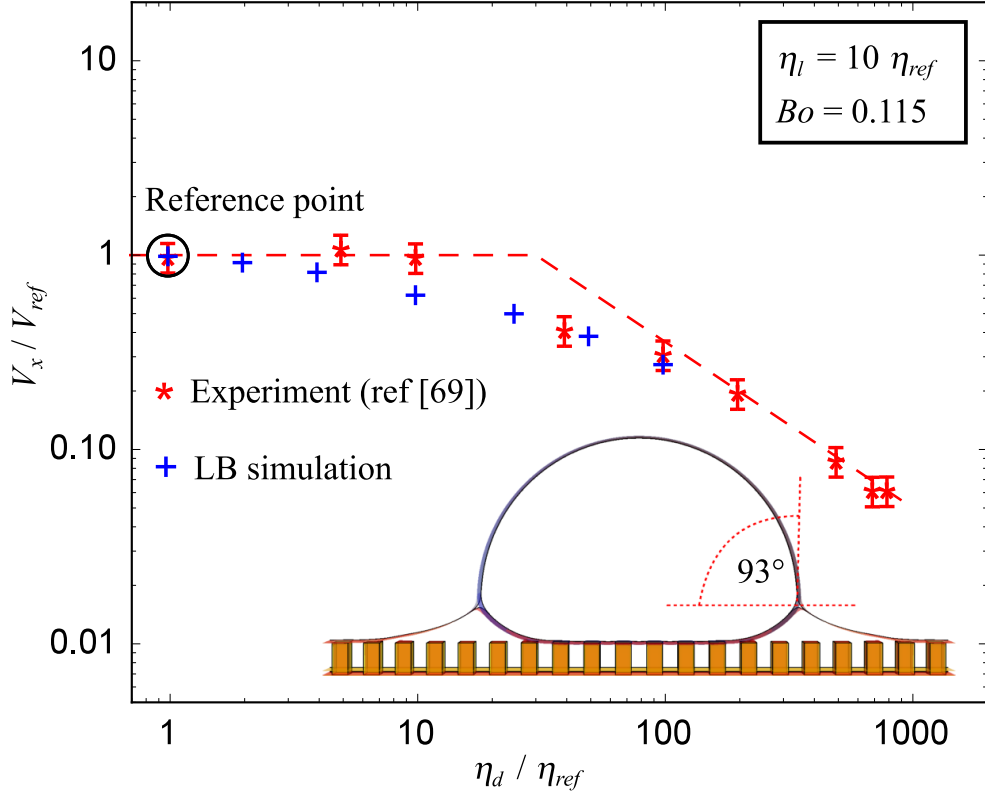


Figure 3.8: Comparison between our simulation results against experimental data by Keiser *et al.* [69]. Here the lubricant viscosity is fixed at $\eta_l = 10 \eta_{ref}$, while the droplet viscosity is varied. The reference viscosity η_{ref} in the experiment is water viscosity (1 mPa.s). To ensure correct viscosity ratio between the droplet and the air phases, we set $\eta_{ref} = 50\eta_g$ in our simulations. V_{ref} is droplet velocity when $\eta_d = \eta_{ref}$.

The values of experimental parameters used by Keiser *et al.* are $\varphi_s = 0.23$, $\theta_{app} = 90^\circ$, and $Bo = 0.115$ [69]. To mimic this experiment, we use similar surface patterning, surface tensions, and body force in our simulations. Specifically, we use $\varphi_s = 0.25$, $\theta_{app} = 93^\circ$, and $Bo = 0.115$. To allow comparison with experiment, we present the data points from experiment and from our simulations in a non-dimensionalised plot, respectively plotted as red asterisks and blue plus symbols in Fig. 3.8. For the experimental data points, we use the reported value of water viscosity as the reference viscosity, $\eta_{ref} = 1$ mPa.s [69]. Correspondingly, we also use V_x of droplet with viscosity $\eta_d = \eta_{ref}$ as V_{ref} . For simulations, we use the lowest possible value

of viscosity as the viscosity of air η_g . Since the water viscosity at room temperature is about 50 times larger than the viscosity of air, we define η_{ref} in simulation as $\eta_{ref} = 50\eta_g$. To mimic the normalisation in experiment, we also use V_{ref} as droplet velocity when $\eta_d = \eta_{ref}$.

For large droplet viscosity, viscous dissipation lies predominantly inside the droplet. In this regime, as the droplet viscosity is lowered, the droplet velocity increases as $V \propto \eta_d^{-1}$ [69], until it eventually plateaus to $V_x \simeq V_{ref}$. Both in simulations and experiments, the crossover occurs approximately at $\eta_d \sim 3\eta_l$. Below this value of droplet viscosity, viscous dissipation in the lubricant ridge becomes dominant compared to dissipation in the droplet. In this regime, the droplet velocity has a strong dependence on the lubricant viscosity, while the droplet viscosity has virtually no effect.

There are a number of differences between the experiments in Ref. [69] and our numerical setup. Firstly, our simulations are in quasi 3-D, rather than full 3-D. Secondly, the size of the lubricant ridge compared to the droplet size is larger than that in experiments. Thirdly, we have considered partial wetting lubricant, $\theta_{wet} = 45^\circ$, whereas the experiments were done using a complete wetting lubricant, $\theta_{wet} = 0^\circ$. Nonetheless, it is clear from Fig. 3.8 that the crossover between the bulk droplet and lubricant ridge dominated dissipation regimes is a robust phenomenon, which our simulations can accurately capture.

3.4 Discussion

We have presented the results of our LB simulations for a droplet on a LIS system. In section 3.1, we explain the simulation setup used in this study. We then use this setup to study the droplet morphology at the equilibrium state in section 3.2. We explain the method to calculate the apparent contact angle and then compare the results with the theoretical predictions. The apparent angles calculated from our simulation results are systematically off several degrees with the vanishing meniscus approximation in Eq. (3.5). This is because the meniscus size in our system is considerable compared to the droplet itself. Instead, we can measure the Laplace's pressure of the droplet-gas and the lubricant-gas interfaces and calculate the apparent angle using Eq. (3.2). In this case, the calculated contact angles are in excellent agreement with the theoretical prediction. These results confirm that our simulation method can accurately capture the equilibrium properties of a droplet on a LIS. We also demonstrate how the interfacial parameters affect droplet morphology. We conclude that the fluid interfacial

tensions play a more dominant factor compared to the lubricant wetting angles.

In section 3.3, we present the simulation results of droplets moving on LIS under influence of an external body force. We initially discuss the velocity of the droplet as a function of time, which is oscillating as the droplet is moving on the surface. We take the average of the velocity at the steady state to characterise the droplet mobility. We then match the parameters and performed the experiments discussed in Ref. [69] using our LB simulation. The results are analysed by assessing the droplet mobility for different lubricant viscosity. We successfully capture the two regimes of dominating channel of the energy dissipation, as is presented in Ref. [69]. This agreement between our LB simulation results with the experiments of moving droplets confirms that our simulation method can capture the dynamics of a droplet on a LIS. These validations of our simulation results, both the equilibrium and dynamics properties, become the stepping stone for studying the effect of the thermodynamic properties of the system to the droplet dynamics, which is discussed in the next chapter.

There are several aspects that are worth investigating for future studies. At this point, we have only considered one type of surface texturing, which is square posts. However, from Eq. (3.5) we can see that the solid surface only influences the droplet morphology via the solid fraction φ_s . In the future, it would be interesting to study how the droplet shape is influenced by the details of the surface texture. It is also interesting to study the effect of the surface texturing to droplet mobility and the durability of LIS. In particular, we find it intriguing to study the relationship between the detail of surface texturing and the rate of lubricant depletion and lubricant recovery in LIS system.

CHAPTER 4

Translational and Rotational Dynamics of Droplets on Liquid Infused Surfaces

Compared to the more commonly studied cases of smooth and superhydrophobic surfaces [81, 83–87], the main distinguishing feature of liquid infused surfaces (LIS) is the presence of the infusing lubricant which forms a wetting ridge. Thus the central aim of this chapter is to shed light on the role of the lubricant ridge in the dynamics of droplets on LIS.

Based on thermodynamic arguments, Smith *et al.* showed that a liquid droplet placed on LIS may invade the corrugation and replace the infusing lubricant, or it can sit on top of the corrugation with the lubricant present underneath the droplet [57]. If the lubricant is perfectly wetting the substrate, the droplet and the corrugated surface are separated by a thin film, and no pinning of the contact lines take place. However, closer inspection employing confocal microscopy revealed that this case is unlikely for a number of common lubricants, as they form in contact to the solid with a small but finite contact angle [57, 64]. As such, on one hand, the surface roughness helps to contain the lubricant; on the other hand, it is also the source of contact line pinning and contact angle hysteresis.

The presence of lubricant meniscus also introduces a competition of dissipation mechanisms acting on a droplet as it moves across LIS. The viscous dissipation may occur predominantly in the droplet or in the lubricant depending on the ratio of the droplet to the lubricant viscosities [69]. We confirmed this behaviour using our LB simulation, as discussed in the previous chapter. The similarity between experiments and numerical simulations is valid despite the fact we employed partial wetting lubricants, which involve also pinning and depinning effects.

However, most studies to date consider only droplets with apparent contact angles close to 90° [57, 69], and the impact of the shape of the lubricant meniscus on droplet mobility remain unexplored. To cover such gaps, in this chapter we will investigate these variations systematically using the lattice Boltzmann simulation method. Here we will focus on the role of lubricant wettability on the droplet mobility, in particular on the interplay between contact line pinning and viscous friction.

To study droplet mobility on LIS, we consider both translational and rotational motions. The translational motion of the droplet is assessed from the average droplet velocity in the direction parallel to the substrate. The starting point of this work is the relationship between the apparent angle and the droplet velocity on LIS in comparison to the smooth surface. Due to the presence of the surface inhomogeneity, droplet on LIS may experience a resisting force due to contact line pinning, especially when partially wetting lubricant is incorporated. We then study the interplay between this contact line pinning and viscous dissipation. We found that the droplet mobility is not only affected by the shape of the droplet but also the shape of the meniscus.

Similarly for the rotational motion, we also study the effect of the apparent contact angle on the percentage of energy that is converted into rotational motion when the droplet is moving. In a pioneering work, Smith *et al.* qualitatively observed the internal circulation of a moving droplet on LIS using coffee powder as particle tracking [57]. Here we show that using LB simulations we can quantify the rotational motion in a cleaner way by calculating the vorticity of the fluid flow inside the droplet. We further study the effect of the lubricant wettability as well as the viscosities of both the droplet and the lubricant on the rotational motion.

4.1 Translational Dynamics

In this section, we study the translational motion of the droplet. As a reference case, we first consider a droplet moving on a flat surface as illustrated in the bottom-right inset of Fig. 4.1(a). The viscosity of the droplet is set to be $\eta_d = 50\eta_g$ to mimic a water droplet in a dry air environment. A constant body force with $Bo = 0.211$ is then applied to mobilise the droplet so that the droplet moves and reaches a steady state velocity. Here, Bo is the Bond number defined as $Bo = \Delta(\rho G)R^2/\gamma_{dg}$ where R , G and γ_{dg} are the initial droplet radius as shown in Fig. 3.2, the acceleration from the body force, and the droplet-gas surface tension

respectively. We also use the capillary number $Ca = \eta_d V_x / \gamma_{dg}$ to characterise the droplet mobility, where η_d and V_x respectively are the droplet viscosity and the average velocity of the droplet after reaching the steady state respectively.

The results obtained for droplets on a smooth surface are plotted in Fig. 4.1(a) as a function of the contact angle. For a smooth surface, we identify the apparent contact angle $\theta_{app} = \theta_{dg}$, which is the droplet contact angle on a smooth surface in the air environment. In agreement with previous studies, the steady state capillary number of the droplet increases monotonically with θ_{app} [86,87], due to the decrease in wedge dissipation at the contact line.

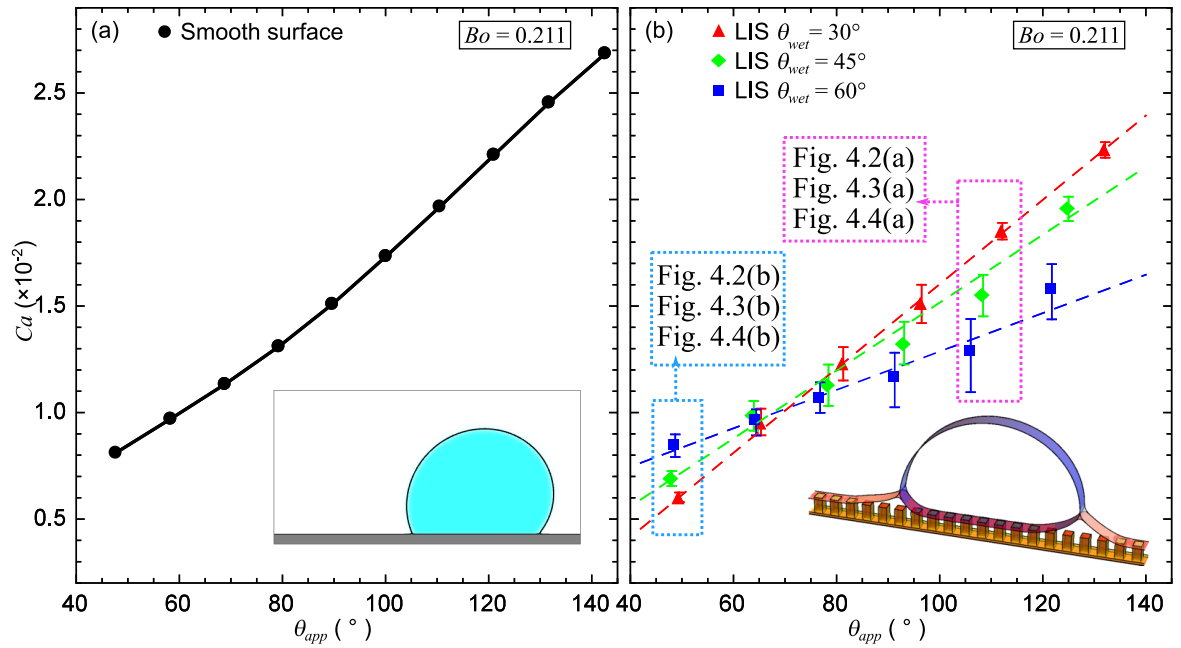


Figure 4.1: (a) Droplet mobility on smooth surface and (b) on LIS plotted against the apparent contact angle θ_{app} . For panel (a) θ_{app} is the material contact angle while for panel (b) θ_{app} is the droplet contact angle measured from the top of meniscus. θ_{wet} is the wetting angle of the lubricant phase ($\theta_{lg} = \theta_{ld} = \theta_{wet}$). The droplet mobility is represented by the capillary number Ca . The error bars represent the maximum and the minimum variation droplet velocity due to the oscillation when moving on the textured surface.

Let us now consider the equivalent setup for droplets on LIS, as illustrated in the bottom-right inset of Fig. 4.1(b). The apparent contact angle θ_{app} for droplet on LIS is defined as the droplet contact angle measured from the top of the meniscus, as has been discussed in section 3.2 in the previous chapter. The lubricant viscosity η_l is set to be the same as the droplet viscosity, $\eta_l = \eta_d = 50\eta_g$. To reduce the number of parameters to be explored in our simulations, we will assume a symmetric wetting condition for the lubricant, where $\theta_{lg} = \theta_{ld} = \theta_{wet}$.

For a given θ_{wet} we systematically vary θ_{app} by tuning the fluid-fluid surface tensions,

and consequently the Neumann angles, θ_l , θ_d and θ_g . θ_{app} is measured when the droplet is in mechanical equilibrium. In Fig. 4.1(b) we compare the droplet mobility, quantified as the time-averaged capillary number Ca for $\theta_{wet} = 30^\circ$ (red triangles), $\theta_{wet} = 45^\circ$ (green diamonds), and $\theta_{wet} = 60^\circ$ (blue squares). Similar to the smooth surface case, the droplet mobility increases monotonically with the apparent angle, but the magnitude of the Ca is generally smaller than for a smooth surface. Interestingly, when comparing the three datasets for different θ_{wet} , we observe that, while for larger θ_{app} droplets with smaller θ_{wet} move faster than those with larger θ_{wet} , this ordering is reversed for lower θ_{app} . The presence of these two regimes (for lower θ_{app} and larger θ_{app}) is persistent for different values of Bo , η_d and η_l .

We hypothesise this ordering inversion is due to a shift in the relative importance between viscous dissipation and contact line pinning at the lubricant ridge. To better characterise the pinning-depinning effects during droplet motion, we plot the instantaneous Ca associated to the droplet's centre of mass, as a function of time for three droplets with $\theta_{app} \sim 110^\circ$ and $\theta_{app} \sim 45^\circ$ respectively in Figs. 4.2(a) and (b). We observe that the instantaneous Ca oscillates periodically, which is due to pinning-depinning events as the droplet moves across the periodic LIS pattern. For both large (Fig. 4.2(a)) and small (Fig. 4.2(b)) θ_{app} , the oscillations with larger amplitude are always observed for higher θ_{wet} . At the same time, the amplitude of the oscillations is generally smaller for $\theta_{app} \sim 45^\circ$ than for $\theta_{app} \sim 110^\circ$, which implies a less pronounced effect of pinning and depinning. Since θ_{app} here is only influenced by the surface tension ratio, as θ_{wet} remain the same, this becomes the first indication of the importance of surface tensions to the pinning force, which will be investigated further in the later chapter of this thesis.

Another factor that influences the droplet mobility is viscous dissipation. To further assess the relative importance of pinning versus viscous dissipation, we explore the relation between the driving force and the droplet velocity for both cases of $\theta_{app} \sim 110^\circ$ (Fig. 4.3(a)) and $\theta_{app} \sim 45^\circ$ (Fig. 4.3(b)). Assuming a linear approximation, the relation between Ca , Bo and the critical bond number Bo_c can be expressed as [17, 57, 88]

$$Ca = \frac{1}{\beta}(Bo - Bo_c). \quad (4.1)$$

Bo_c is the largest Bond number at which the droplet remains stationary. Bo_c is also a measure of contact line pinning, or alternatively, contact angle hysteresis. β is a function of the shapes

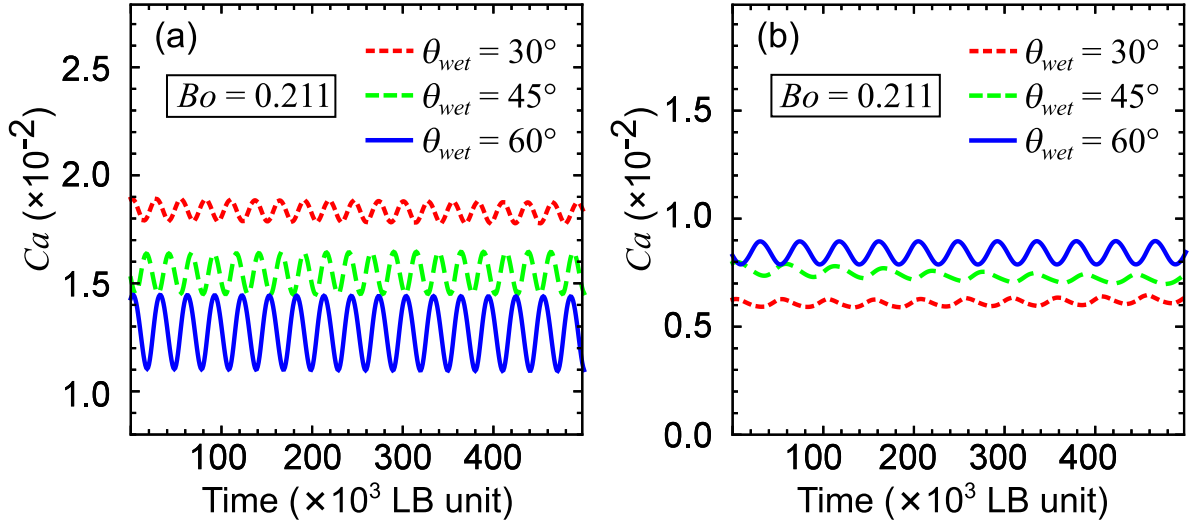


Figure 4.2: Droplet mobility versus time for droplets with (a) $\theta_{app} \sim 110^\circ$ and (b) $\theta_{app} \sim 45^\circ$ as indicated in Fig. 4.1(b). The capillary number Ca increases and decreases periodically due to pinning-depinning events.

of the droplet and lubricant meniscus, and it is related to their rate of viscous dissipation [17, 57, 88].

Considering Ca as a function of $(Bo - Bo_c)$, our data show an important difference between the large and small apparent angle droplets. For large apparent angles (Fig. 4.3(a)), all the curves practically overlap onto a master curve. The variations in the results for $\theta_{wet} = 30^\circ$ (red triangles), 45° (green diamonds), and 60° (blue squares) can be captured by differences in the value of the critical Bond number, Bo_c , as shown in the inset. This indicates that the ordering observed in Fig. 4.1(b) for the large θ_{app} is determined by contact line pinning. The values of prefactor β are similar for the three datasets in Fig. 4.3(a), which suggest that the rate of viscous dissipation is on average the same once the reduction in the effective driving force due to pinning forces is taken into account.

In contrast, for small apparent angles (Fig. 4.3(b)), the datasets do not overlap onto a master curve. The critical Bond number, Bo_c , is also essentially the same for the three θ_{wet} used, any differences observed are within the error of the measurements. These two observations suggest that, for low θ_{app} , contact line pinning plays a minor role. The variations in Ca vs $(Bo - Bo_c)$ for the three datasets in θ_{wet} further imply that viscous dissipation is larger for the more wetting lubricant (the smaller θ_{wet}). Inspection of the droplet morphologies (Fig. 4.4) supports this observation. We find that, for large θ_{app} , the lubricant ridges have a similar shape, regardless of θ_{wet} . In contrast for low θ_{app} the ridge shape is broader for lower

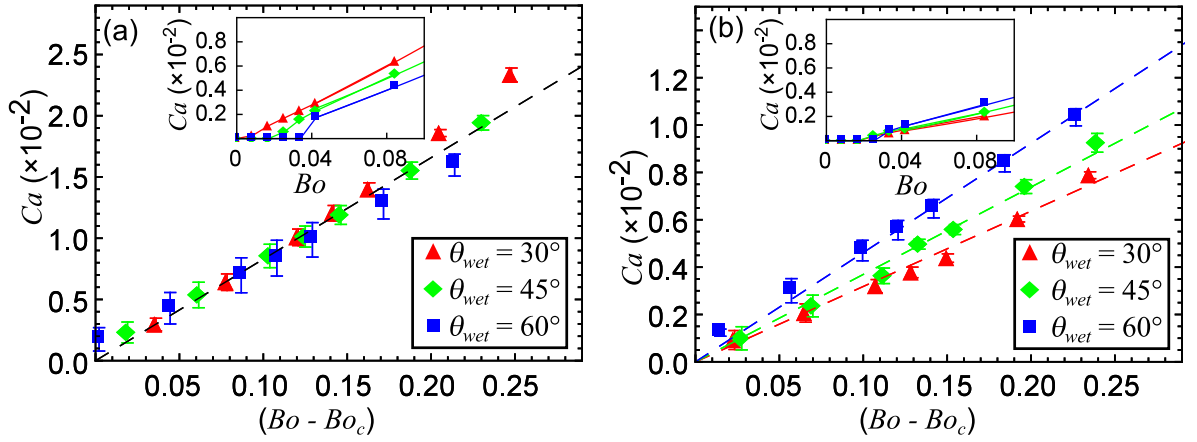


Figure 4.3: Droplet mobility as a function of $Bo - Bo_c$ for droplets with (a) $\theta_{app} \sim 110^\circ$ and (b) $\theta_{app} \sim 45^\circ$ as indicated in Fig. 4.1(b). Bo is the Bond number. The insets show the critical Bond number, Bo_c , at which the droplets start moving under external body force.

θ_{wet} . We hypothesise that the rate of viscous dissipation depends on the shape of the lubricant meniscus. As such, droplets with large θ_{app} (Fig. 4.4(a)) have similar viscous dissipation while droplets with low θ_{app} (Fig. 4.4(b)) have more variation in viscous dissipation. We can also see that the variation in the shape of the lubricant meniscus is controlled by θ_{wet} .

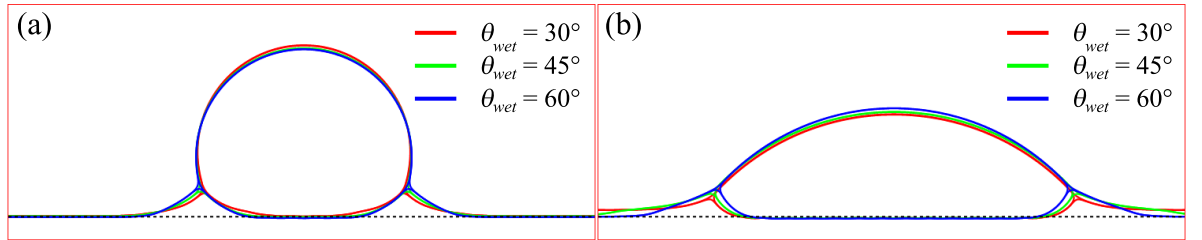


Figure 4.4: Droplet shapes for droplets with (a) $\theta_{app} \sim 110^\circ$ and (b) $\theta_{app} \sim 45^\circ$ as indicated in Fig. 4.1(b).

To further corroborate this hypothesis, we ran three additional sets of simulations, where pinning and depinning is inhibited by replacing the topography with a flat substrate, as shown in Fig. 4.5. The three sets correspond to $\theta_{wet} = 30^\circ$ (red triangles), $\theta_{wet} = 45^\circ$ (green diamonds), and $\theta_{wet} = 60^\circ$ (blue squares). The amount of lubricant in both the front and back ridge is the same for all 2D cases. Accordingly, once pinning is removed, droplets with higher θ_{wet} always move faster irrespective of θ_{app} , showing the same ordering that we obtain only for low θ_{app} in Fig. 4.1(b).

Fig. 4.6(a) compares the morphologies of droplets B and D indicated in Fig. 4.5. The two droplets have an almost identical shape and θ_{app} , but their lubricant ridge shapes and mobilities are different. For droplet B, θ_{wet} is smaller, and therefore the meniscus is broader.

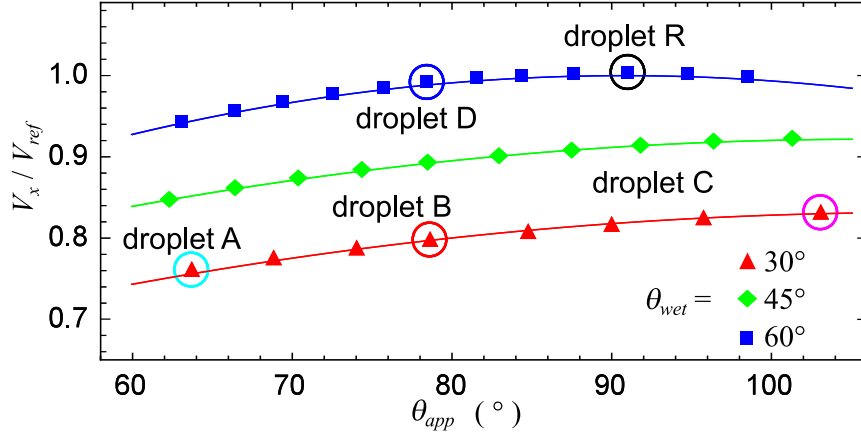


Figure 4.5: In the absence of contact line pinning (flat substrate), droplets with higher θ_{wet} always move faster. The lines are guide for the eye. V_{ref} is the velocity of droplet R.

We can characterise the meniscus shape by its aspect ratio, defined as $AR_m = h_m/l_m$, where h_m and l_m are its height and length respectively, see Fig. 4.6(b).

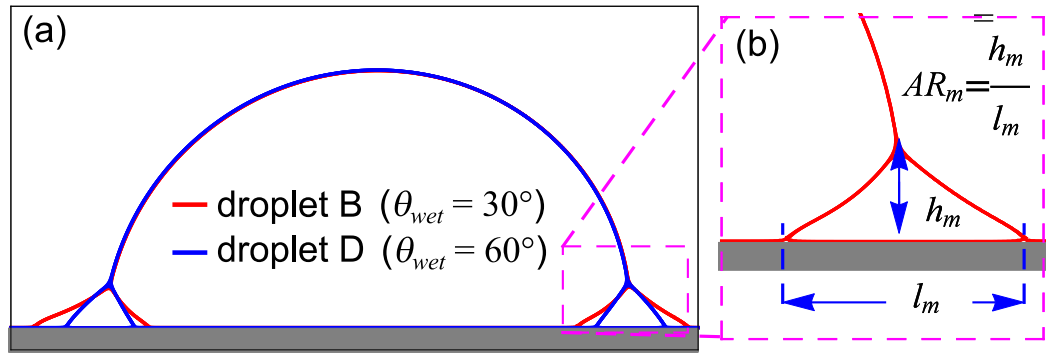


Figure 4.6: (a) Comparison of droplet shapes with the same θ_{app} but different θ_{wet} and correspondingly meniscus aspect ratio AR_m . (b) Definition of AR_m .

We now propose a scaling argument to explain how the droplet mobility depends on the lubricant ridge aspect ratio. We balance the rate of energy injected by the applied body force with the total rate of energy dissipation in the droplet and lubricant,

$$FV_x \sim \eta_d \int |\nabla v|_d^2 dA_d + \eta_l \int |\nabla v|_l^2 dA_l. \quad (4.2)$$

Here F is the total force acting on the droplet. We also recall that the simulations in Fig. 4.5 are two-dimensional simulations; thus the terms on the right hand side are integrated over the droplet and the lubricant ridge area. Taking $|\nabla v|_d \sim V_x/R$ and $|\nabla v|_l \sim V_x/h_m$ as the typical velocity gradient in the droplet and lubricant meniscus, as well as $\Delta A_d \sim R^2$ and $\Delta A_l \sim h_m l_m$

as the typical scales for the cross-sectional area of the droplet and the lubricant, we have

$$F \sim \alpha_d \eta_d V_x + \alpha_l \eta_l V_x l_m / h_m, \quad (4.3)$$

$$V_x \sim \frac{F}{\alpha_d \eta_d + \alpha_l \eta_l / AR_m}. \quad (4.4)$$

where α_d and α_l are positive, dimensionless fitting parameters. Eq. (4.4) shows that a smaller AR_m results in a larger energy dissipation in the lubricant meniscus, which in turn leads to the lower mobility of the droplet.

In Fig. 4.7, we consider droplets A, B and C indicated in Fig. 4.5, and increase their AR_m by tuning θ_{wet} . We keep all other variables in the simulations the same, including the body force, the fluid surface tensions, the lubricant and droplet viscosities, and the total droplet and lubricant cross-sectional area. The data points in Fig. 4.7 correspond to simulation results, while the lines correspond to the best fit results to Eq. (4.4), where we have fitted α_d and α_l separately for each dataset. Consistent with our scaling argument, for all of the three datasets in Fig. 4.5, droplet mobility increases monotonically with AR_m .

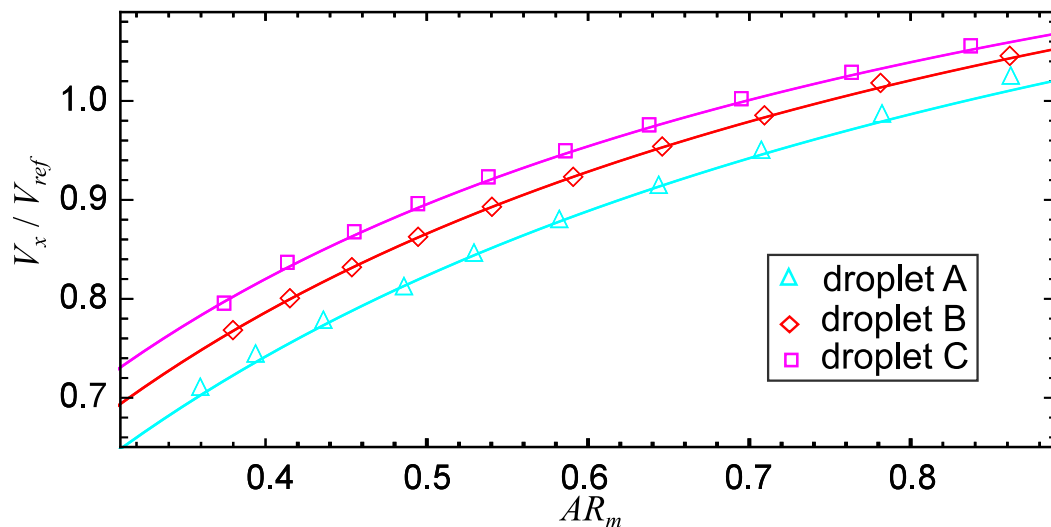


Figure 4.7: Droplet mobility against AR_m for different θ_{app} as indicated in Fig. 4.5. The lines are the best fit results to Eq. (4.4). V_{ref} is taken to be the velocity of droplet R in Fig. 4.5.

Taking advantage of the results in Fig. 4.7, we can robustly conclude that the ordering observed in Fig. 4.1(b) for small θ_{app} is due to variations in viscous dissipation at the lubricant ridge. For the present choice of viscosities $\eta_l = \eta_d = 50\eta_g$, the crossover between pinning and meniscus viscous friction dominated regimes in Fig. 4.1(b) occurs at $\theta_{app} \simeq 70^\circ$. Inversely, we can take the limit where the lubricant viscosity is very low, equal to the gas viscosity. In this

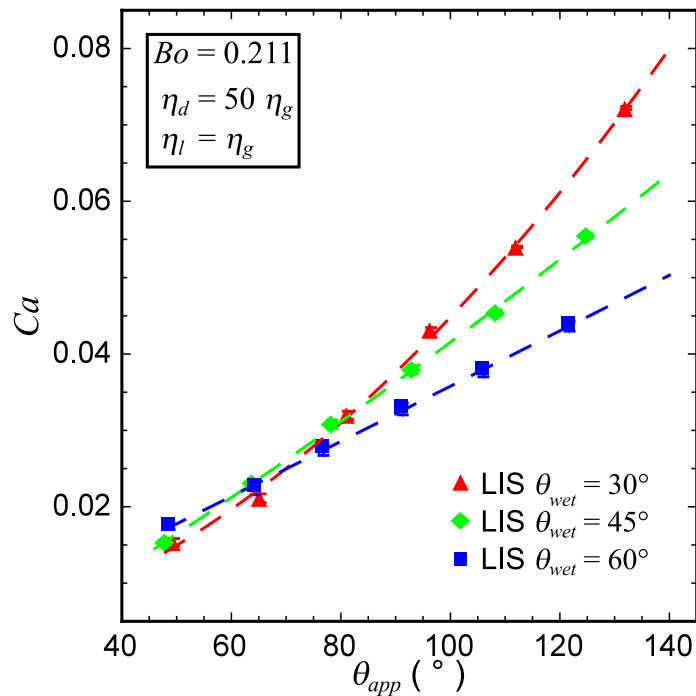


Figure 4.8: Droplet mobility, represented in capillary number Ca , plotted against the apparent angle θ_{app} . Here, the viscosity of the lubricant is set to the gas viscosity, $\eta_l = \eta_g$. For high apparent angles, contact line pinning effect is important, and consequently droplets with lower wetting angle, θ_{wet} , move faster. For low apparent angles, contact line pinning is not dominant and the small lubricant viscosity means viscous dissipation is small compared to that in the droplet. As such, the droplet mobilities are similar as we vary θ_{wet} .

case, viscous dissipation at the lubricant is weak compared to that in the droplet. As expected, as shown in Fig. 4.8, for low apparent angle θ_{app} , we then observe that the droplet mobilities remain very similar as we vary the wetting angle θ_{wet} .

4.2 Rotational Dynamics

It has been shown that droplets move across a solid surface by sliding, rolling or a combination of the two, depending on the surface texture of the solid and the shape of the droplets [81,86]. In some application such as self-cleaning surfaces, rolling motion is desirable as it allows droplets to pick more dirt as they move on a surface [89]. In this section, we demonstrate how the droplet rolling motion on LIS is characterised. We also discuss how liquid viscosities, the droplet apparent contact angle, lubricant wetting angles affect the rolling motion.

To quantify the rolling motion, assume the fluid velocity vector is given by $\vec{v}(x,y) = a(x,y)\hat{i} + b(x,y)\hat{j}$, where a and b are the velocity components in the horizontal (x) and vertical (y) directions respectively, while \hat{i} and \hat{j} are unit vectors in the corresponding directions. A

typical example is shown in Fig. 4.9(a). To compute the fluid velocity inside the droplet, we subtract the centre of mass velocity, $\vec{v}'(x, y) = \vec{v}(x, y) - \vec{v}_{cm} = a'(x, y)\hat{i} + b'(x, y)\hat{j}$. The typical velocity pattern in the centre of mass reference is shown in Fig. 4.9(b).

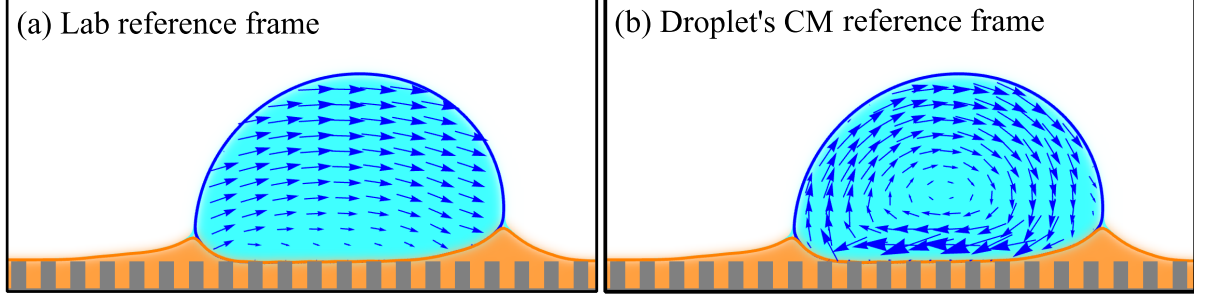


Figure 4.9: The fluid velocity inside the droplet in (a) the laboratory and (b) droplet centre of mass frames of reference. The size of the arrows indicates the magnitude of the velocity vector.

To compute the angular velocity of the rolling motion, we first need to calculate the vorticity Ω defined as $\Omega(x, y) = b'_x - a'_y$. Here, we have used the notation a'_i and b'_i for the partial derivatives of the velocity components in the i -direction. This vorticity is a local quantity which includes shearing motion and rigid body rotation of a fluid element [86]. The shearing motion is characterised by the strain rate S , which is given by $S(x, y) = \sqrt{4(a'_x)^2 + (a'_y + b'_x)^2}$. The rigid body rotation then can be obtained by subtracting the strain rate from the total vorticity, which is called the residual vorticity Ω_{res} . Mathematically this can be expressed as [86]

$$\Omega_{res}(x, y) = \Omega(x, y) - S(x, y), \quad (4.5)$$

The result of this process is color mapped in Fig. 4.10.

The angular velocity is then computed as half of the average residual vorticity inside the droplet, $\omega = \langle \Omega_{res}/2 \rangle$, and correspondingly the velocity due to rolling motion V_{roll} is approximated by $V_{roll} = \omega r$. Following Thampi *et al.* [86], we have taken the radius of rotation to be half of the droplet height, $r = h_d/2$. Finally, the percent of rolling motion is given by

$$\%Roll = (V_{roll}/V_x) \times 100. \quad (4.6)$$

Let us start by examining the rotational dynamics of droplets on a smooth surface. The data for $\%Roll$ versus θ_{app} are plotted as black circles in Fig. 4.11. We see that they fall onto a master curve (black line), regardless of the Bond number Bo . This means $\%Roll$ primarily

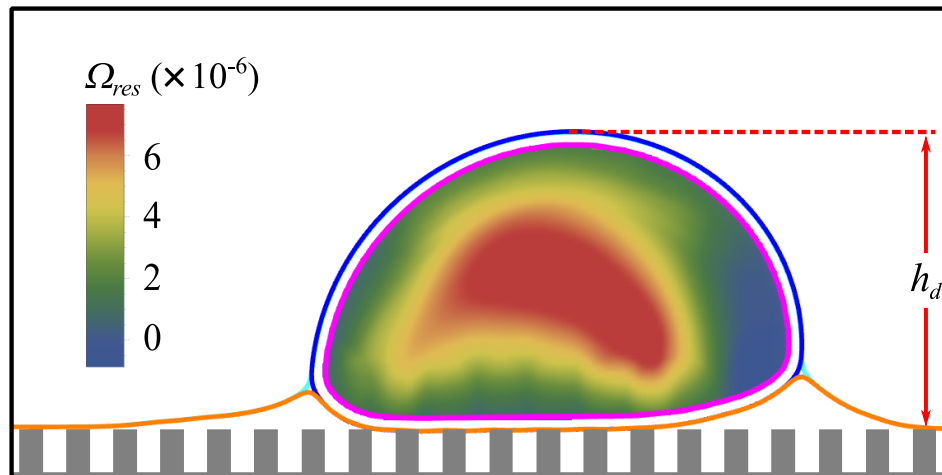


Figure 4.10: The result of calculation of the residual vorticity Ω_{res} using Eq. (4.5). The average of Ω_{res} is then used to calculate the angular velocity of the droplet ω .

depends on the shape of the droplet. The higher θ_{app} the closer the droplet is to a spherical shape, and the more the droplet rolls. These results are in agreement with previous studies, see e.g. Ref. [81, 86].

For droplets on LIS, we also observe that all data points fall onto a master curve (magenta line), as we vary both Bo and the wetting angles θ_{wet} , which again implies the main dependence of $\%Roll$ is on the droplet shape. Initially, in the case of LIS, $\%Roll$ also increases with θ_{app} . However, beyond $\theta_{app} \approx 110^\circ$, unlike the smooth surface scenario, here $\%Roll$ decreases instead. Our simulation results suggest this is because the lubricant acts to reduce the contact between the droplet and the solid surface on top of the posts. Comparing the configurations obtained in our simulations, the contact area is smaller for droplets on LIS than on a smooth surface for the same apparent angle θ_{app} . Such contact reduction with the solid surface results in smaller angular velocity of the droplet ω , and subsequently smaller percentage of rolling $\%Roll$.

The data points in Fig. 4.11 are the average $\%Roll$ computed from our simulations, while the error bars correspond to the maximum and minimum values observed. The variation of $\%Roll$ is related to the oscillation of the droplet velocity when moving on the textured surface. Comparing the results for different θ_{wet} , we observe that the error bars are much bigger for higher θ_{wet} than for lower θ_{wet} , especially for large θ_{app} . This is another manifestation of contact line pinning effect. As discussed in the previous section, contact line pinning plays a less important role for small θ_{app} . Droplets with lower θ_{app} also have a larger number of posts with which they are in contact. As a result, the variation in the number of posts covered by the droplets as they move and the observed value of $\%Roll$ do not vary significantly (i.e. the

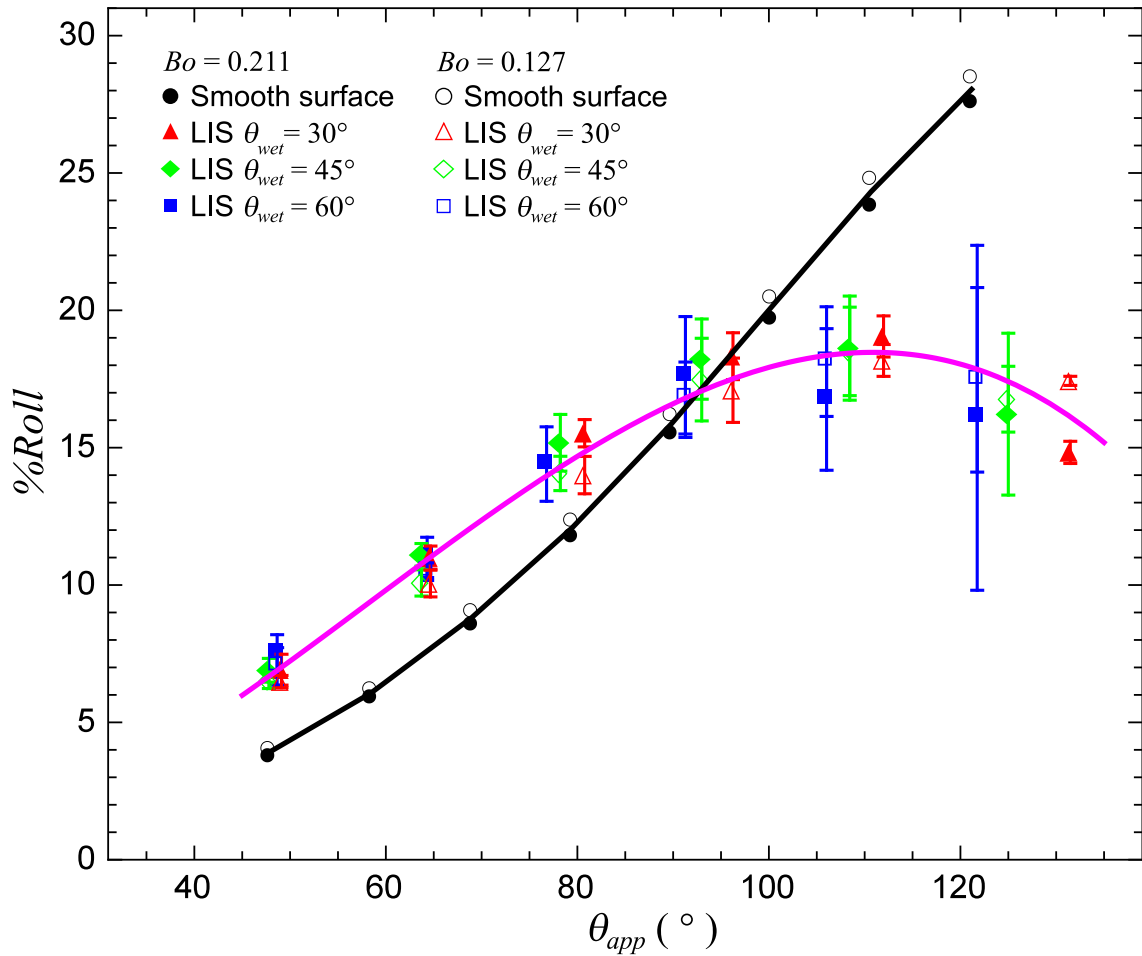


Figure 4.11: The percentage of rolling $\%Roll$ against θ_{app} for several values of Bond number Bo and wetting angle θ_{wet} .

error bars are small). In contrast, for large θ_{app} , contact line pinning is stronger for higher θ_{wet} , as we have previously seen in Fig. 4.2(a). Furthermore, the droplets sit on top of a small number of posts in our simulations, and the variation in the number of posts due to pinning and depinning events is significant. Therefore, the measured $\%Roll$ can vary dramatically as the droplets move across the surface, resulting in large error bars.

We also consider the effect of viscosity on the rolling dynamics of droplets on LIS by varying the droplet viscosity η_d for a fixed lubricant viscosity η_l for several values of η_l . Both the droplet and lubricant viscosities are represented in the unit of a fixed reference viscosity, $\eta_{ref} = 50\eta_g$, which mimics the viscosity ratio of water to air. As shown in Fig. 4.12, for a given η_l , $\%Roll$ slightly increases with η_d but it reaches a plateau for $\eta_d \gtrsim 2.5\eta_{ref}$. Such result is similar to what is observed in the rolling dynamics of droplets on a smooth surface where $\%Roll$ initially increases with the droplet viscosity, but it then starts plateauing when the

droplet to gas viscosity ratio is about 50 [86]. We also find that the rolling dynamics depends only weakly on η_l . In particular, for $\eta_l \gtrsim 2\eta_{ref}$, the rolling dynamics are insensitive to any further increase in the lubricant viscosity, while the data points collapse to a master curve.

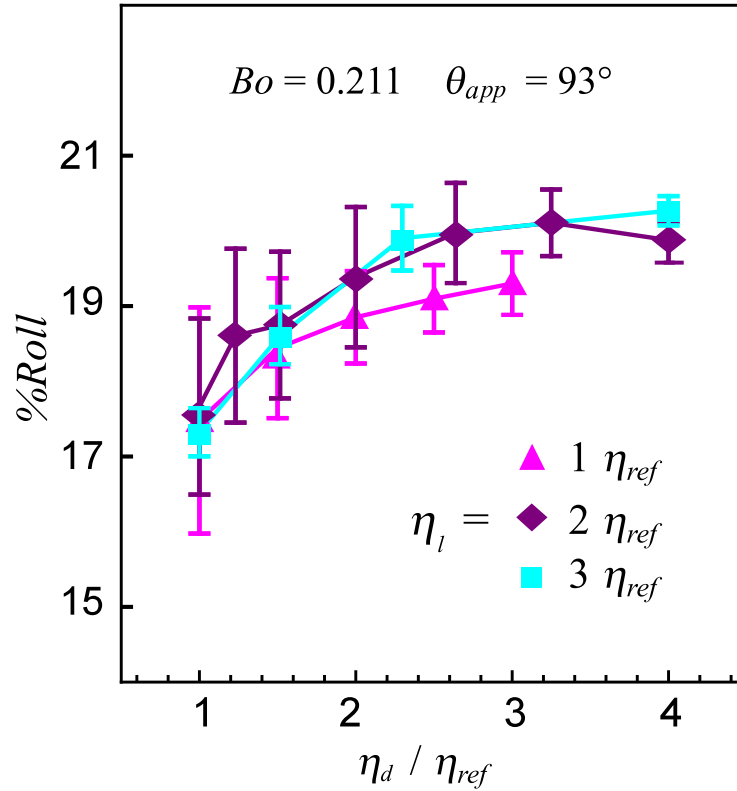


Figure 4.12: The percentage of rolling $\%Roll$ against the ratio of the droplet to the lubricant viscosities.

4.3 Discussion

In this chapter, we have employed the LB simulations to study droplet dynamics on LIS. By executing systematic numerical studies of droplet motion on LIS we highlight the rich interplay between contact line pinning and viscous dissipation at the wetting ridge in determining the droplet mobility. The droplet mobility is affected by contact line pinning in cases where θ_{app} are high. In such cases, employing lubricants with lower θ_{wet} will reduce contact line pinning and allow the droplets to move faster. For low θ_{app} , contact line pinning is less significant, and droplet mobility can be tuned by adjusting the shape (aspect ratio) of the meniscus. More wetting lubricants lead to wetting ridges with smaller aspect ratios, which in turn result in

larger viscous dissipation.

Additionally, we have shown that the advancing mechanism of droplets on LIS is a combination of sliding and rolling motion, where typically the percentage of rolling is relatively small, $\%Roll < 20\%$. Similar to the case of droplets on smooth surfaces, the primary determinant of $\%Roll$ is the droplet shape. However, unlike the smooth surface scenario, we find $\%Roll$ does not increase monotonically with θ_{app} because the droplet is quickly losing contact with the solid surface at high apparent contact angle. Finally, for sufficiently high droplet and lubricant viscosities, we find $\%Roll$ only depends weakly on these two fluid viscosities.

For the future outlook, it is interesting to consider the case where the lubricant perfectly wets the solid and is encapsulating the droplet. This typical case is particularly interesting because, on one hand, the droplet can glide on the surface pinning free, but on the other hand, the lubricant gradually depletes as the droplet sheds from the surface. Currently, our simulation codes are not able to simulate the perfectly wetting lubricant condition. In order to implement this, the disjoining pressure needs to be incorporated into the free energy model. In addition, since the lubricant film is very thin compared to the size of the droplet, this situation might be difficult to be simulated using the diffuse interface model.

Another interesting aspect is the dynamics of the lubricant, both at the wetting ridge and within the surface corrugation. This case is of interest as this might help us understand how the lubricant depletes from the corrugation and how to mitigate this lubricant depletion. From the channel flow simulation, we understood that the fluid velocity depends on the channel width and the fluid viscosity. Thus, we speculate that the lubricant is relatively stationary in the corrugation when compared to the droplet, especially for high lubricant viscosity. However, the same thought experiment is invalid for the meniscus and thus the flow physics at the lubricant meniscus remains an open question. To properly study this, one should scale up the simulation so that the diffuse interface effect does not interfere with the results.

CHAPTER 5

Bidirectional Motion of Droplets on Gradient Liquid Infused Surfaces

Controlling droplet motion on a solid surface is important for a wide range of applications, from droplet microfluidics to water harvesting and self-cleaning surfaces [90–95]. Among the various approaches to induce motion, a good passive strategy is to introduce a wetting gradient on the solid surface, as this does not require energy to be provided continuously to the system. Such spontaneous motion has been extensively investigated for binary fluids systems under a variety of wetting gradients, including due to variations in surface chemistry [96, 97], topography [32, 68, 98] and elasticity [99].

More recently, there has been a growing interest to study droplet self-propulsion on liquid infused surfaces (LIS) [100–102]. Importantly, in all cases reported to date, including existing works on LIS, droplet motion on surfaces with texture/topographical gradients is always unidirectional towards the denser solid fraction area. In contrast, here we will demonstrate a bidirectional spontaneous droplet motion. The presence of the lubricant on LIS can be exploited for a novel self-propulsion mechanism, in which the droplet has preferential wetting on *either* the denser *or* the sparser solid fraction area. Fig. 5.1 provides an example of this phenomenon. In Fig. 5.1(a), when a structured substrate is infused with an ionic liquid, a water droplet placed on the surface moves toward the sparser solid area. In contrast, when the same substrate is infused with Krytox oil, the water droplet moves toward the denser solid area, as shown in Fig. 5.1(b).

This chapter is structured as follows. First, we develop an analytical theory that elaborates how topographical gradient on LIS gives rise to the driving force that can propel droplets

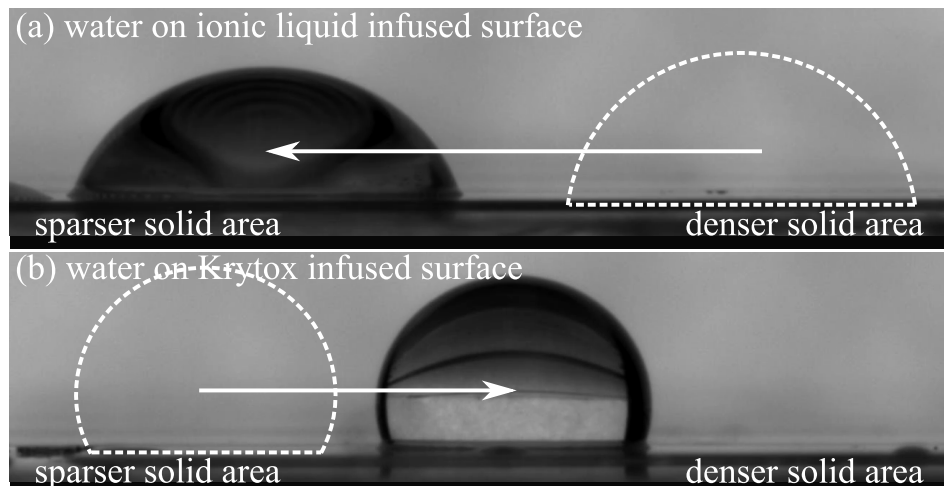


Figure 5.1: Spontaneous droplet motion on LIS with topographical gradient. (a) Water droplet on ionic liquid infused surface moves toward the sparser solid area, while for (b) Krytox infused surface, water droplet moves toward the denser solid area.

toward two possible directions. We then verify our theory using both lattice Boltzmann simulations and experiments. We demonstrate that this phenomenon can be observed using various liquid combinations for droplets and lubricants, as well as for different forms of structural gradients.

5.1 The Origin of the Driving Force

When a liquid droplet is placed on a homogenous solid surface, it stays stationary because the surface tension force pulls the base of the droplet equally in the radial direction [7]. This force balance is broken when the wettability of one side of the droplet is different from the other, resulting in a spontaneous droplet motion towards the more wettable region of the solid [103].

On LIS, the apparent contact angle of a droplet depends on the surface tensions and the intrinsic contact angles of all fluids involved in the system [66,67,104]. This rich interplay makes it much less trivial to predict the direction of droplet motion when there is a topographical gradient. To do this we need to break down the contributing surface tension forces.

Consider a liquid droplet placed on top of a LIS with topographical gradient, as shown in Fig. 5.2(a). The substrate is set horizontally such that gravity does not play a role. For convenience, we use the subscripts d, l, g and s to refer to the droplet, infusing lubricant, gas and solid phases respectively. Furthermore, we introduce spreading parameter [57],

$$S = \gamma_{dg} - \gamma_{lg} - \gamma_{ld}, \quad (5.1)$$

with γ_{mn} the interfacial tension between phases m and n . The droplet is encapsulated by the lubricant when $S > 0$ [57, 65, 66], see Fig. 5.2(c). For $S < 0$, the droplet is not encapsulated, as illustrated in Fig. 5.2(d).

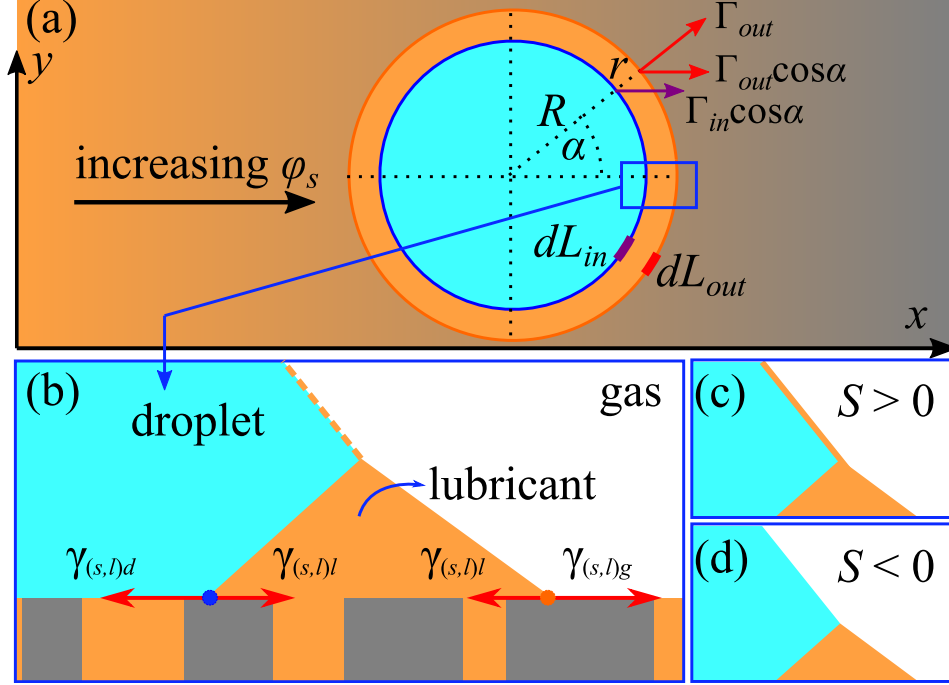


Figure 5.2: (a) Illustration of a droplet on a LIS with topographical gradient, where greater solid fraction (φ_s) area is indicated by the darker area. R and r are the droplet base radius and meniscus width respectively. Γ_{out} and Γ_{in} are the surface tension forces per unit length that act on the outer and inner contact lines. (b) Magnification of the meniscus area (side-view). The red arrows indicates the relevant composite interfacial tensions, as described in Eqs. (5.2)-(5.4). The dashed line at droplet-air interface indicates the possibility of lubricant encapsulation. Depending on the sign of the spreading parameter S , the lubricant may encapsulate the droplet (c-d).

We will now argue that LIS can be considered as composite surfaces of solid and lubricant, with fractions of φ_s and $(1 - \varphi_s)$ respectively. Therefore, the *composite* interfacial tension of LIS with phase m is $\gamma_{(s,l)m} \equiv \varphi_s \gamma_{sm} + (1 - \varphi_s) \gamma_{lm}$. Letting the solid fraction φ_s vary in the x direction only (see Fig. 5.2(a)), then leads to the composite interfacial tensions

$$\gamma_{(s,l)d} \equiv \varphi_s(x) \gamma_{sd} + (1 - \varphi_s(x)) \gamma_{ld}, \quad (5.2)$$

$$\gamma_{(s,l)l} \equiv \varphi_s(x) \gamma_{sl} + (1 - \varphi_s(x)) \gamma_{ll} = \varphi_s(x) \gamma_{sl}, \quad (5.3)$$

$$\gamma_{(s,l)g} \equiv \varphi_s(x) \gamma_{sg} + (1 - \varphi_s(x)) \gamma_{lg}. \quad (5.4)$$

It is worth mentioning that these composite interfacial tensions are the same irrespective of whether the droplet is encapsulated. The key effect of the lubricant encapsulation is to alter

the effective droplet-air surface tension to be $\gamma_{eff} = \gamma_{ld} + \gamma_{lg}$, as the droplet-air interface in this case is now constitutes as droplet-lubricant and lubricant-air interfaces [104].

The relevant surface tension forces per unit length that pull the droplet in radial direction are $\Gamma_{in} = \gamma_{(s,l)l} - \gamma_{(s,l)d}$ and $\Gamma_{out} = \gamma_{(s,l)g} - \gamma_{(s,l)l}$ for the inner (droplet-lubricant-composite substrate) and the outer (lubricant-air-composite substrate) contact lines respectively, which are given by

$$\Gamma_{in} = (\gamma_{sl} - \gamma_{sd} + \gamma_{ld})\varphi_s(x) - \gamma_{ld}, \quad (5.5)$$

$$\Gamma_{out} = (\gamma_{sg} - \gamma_{lg} - \gamma_{sl})\varphi_s(x) + \gamma_{lg}. \quad (5.6)$$

Since φ_s does not vary with y , only the x -component of the forces contributes to the driving force, i.e. $\Gamma_{in} \cos \alpha$ and $\Gamma_{out} \cos \alpha$, where α is azimuthal angle as indicated in Fig. 5.2. The total driving force is thus the sum of these surface tensions integrated over the total perimeters of the inner and outer contact lines,

$$F = \int_{L_{in}} \Gamma_{in} \cos \alpha dL_{in} + \int_{L_{out}} \Gamma_{out} \cos \alpha dL_{out}. \quad (5.7)$$

It can be shown that $\oint \cos \alpha dL_{in} = 0$. Therefore, the constant terms in Eqs. (5.5) and (5.6) do not contribute to the total force when integrated over the contact line. As such, the total driving force can be rewritten as:

$$F = \int_{L_{in}} (\gamma_{sl} - \gamma_{sd} + \gamma_{ld})\varphi_s(x) \cos \alpha dL_{in} + \int_{L_{out}} (\gamma_{sg} - \gamma_{lg} - \gamma_{sl})\varphi_s(x) \cos \alpha dL_{out}. \quad (5.8)$$

We will now make another simplifying assumption. If the shapes of the contact lines are circular (as illustrated in Fig. 5.2), we can express $dL_{in} = R d\alpha$ and $dL_{out} = (R + r) d\alpha$. Hence, the driving force becomes

$$\begin{aligned} F &= (\gamma_{sl} - \gamma_{sd} + \gamma_{ld}) \int_{\alpha} \varphi_s(x) R \cos \alpha d\alpha + (\gamma_{sg} - \gamma_{sl} - \gamma_{lg}) \int_{\alpha} \varphi_s(x) (R + r) \cos \alpha d\alpha, \quad (5.9) \\ &= ((\gamma_{sl} - \gamma_{sd} + \gamma_{ld}) + (\gamma_{sg} - \gamma_{sl} - \gamma_{lg})) \int_{\alpha} \varphi_s(x) R \cos \alpha d\alpha + \\ &\quad (\gamma_{sg} - \gamma_{sl} - \gamma_{lg}) \int_{\alpha} \varphi_s(x) r \cos \alpha d\alpha. \quad (5.10) \end{aligned}$$

We can notice that the first and the second terms in Eq. (5.10) are the contribution of the forces at the droplet base and the meniscus perimeters. Let us first discuss the second term,

whose magnitude proportional to the meniscus width r

$$F_{meniscus} = (\gamma_{sg} - \gamma_{sl} - \gamma_{lg}) \int_{\alpha} \varphi_s(x) r \cos \alpha d\alpha. \quad (5.11)$$

Using the definition of $\cos \theta_{lg} = (\gamma_{sg} - \gamma_{sl})/\gamma_{lg}$, we can write $F_{meniscus}$ as

$$F_{meniscus} = \gamma_{lg}(\cos \theta_{lg} - 1) \int_{\alpha} \varphi_s(x) r \cos \alpha d\alpha. \quad (5.12)$$

From Eq. (5.12), we can see that the prefactor is always negative as long as θ_{lg} is finite. The force from the meniscus always pull the droplet to the opposite direction of the topographical gradient. For example, if the solid surface becomes denser with increasing x , $F_{meniscus}$ is always pulling the droplet in the $-x$ direction.

5.2 Small Meniscus Case

We will now consider the small meniscus case where $r \rightarrow 0$. In this case, the second term in Eq. (5.10) vanishes and the resulting force can be simplified into

$$F = ((\gamma_{sl} - \gamma_{sd} + \gamma_{ld}) + (\gamma_{sg} - \gamma_{sl} - \gamma_{lg})) \int_{\alpha} \varphi_s(x) R \cos \alpha d\alpha. \quad (5.13)$$

We can simplify Eq. (5.13) further by employing the Young's contact angles of the lubricant in the air and in the droplet phase environments, respectively defined as $\cos \theta_{lg} = (\gamma_{sg} - \gamma_{sl})/\gamma_{lg}$ and $\cos \theta_{ld} = (\gamma_{sd} - \gamma_{sl})/\gamma_{lg}$. In this case, Eq. (5.13) becomes

$$F = (\gamma_{ld}(1 - \cos \theta_{ld}) + \gamma_{lg}(\cos \theta_{lg} - 1)) \int_{\alpha} \varphi_s(x) R \cos \alpha d\alpha. \quad (5.14)$$

From Eq. (5.14) we find that the driving force ceases ($F = 0$) when the lubricant completely wets the solid surface both in the air and in the droplet phase environments ($\theta_{ld} = \theta_{lg} = 0$). This agrees with intuition since, in this case, the surface topography is covered by a thin layer of lubricant everywhere. We can still expect spontaneous motion to occur if either θ_{ld} or θ_{lg} is non-zero.

To determine the direction of droplet motion, we can introduce the droplet-air effective

interfacial tension [104]

$$\gamma_{eff} \equiv \begin{cases} \gamma_{lg} + \gamma_{ld}, & \text{if } S > 0 \text{ (lubricant encapsulation),} \\ \gamma_{lg}, & \text{otherwise,} \end{cases} \quad (5.15)$$

and the following definitions of apparent contact angles

$$\cos \theta_{dg|s}^{eff} \equiv \frac{\gamma_{sg} - \gamma_{sd}}{\gamma_{eff}}, \quad \cos \theta_{dg|o}^{eff} \equiv \frac{\gamma_{lg} - \gamma_{ld}}{\gamma_{eff}}, \quad (5.16)$$

such that the driving force in Eq. (5.13) can be written in the following form

$$F = \gamma_{eff} \left(\cos \theta_{dg|s}^{eff} - \cos \theta_{dg|o}^{eff} \right) \int_{\alpha} \varphi_s(x) \cos \alpha R d\alpha. \quad (5.17)$$

The angles $\theta_{dg|s}^{eff}$ and $\theta_{dg|l}^{eff}$ are defined as the contact angles of the droplet, either encapsulated by lubricant or not, on a smooth solid surface and on the lubricant surface respectively. When there is no encapsulation, $\gamma_{eff} = \gamma_{dg}$ and hence $\theta_{dg|s}^{eff} = \theta_{dg|s}$, which is the familiar Young's contact angle of a droplet on a smooth solid surface.

Let us now discuss the terms in Eq. (5.17). The term under the integral depends on the details of the surface patterning, $\varphi_s(x)$, and it modulates the strength of the driving force. The direction of the driving force is determined only by the sign of the gradient in $\varphi_s(x)$ and by the prefactor

$$\tilde{F} = \left(\cos \theta_{dg|s}^{eff} - \cos \theta_{dg|l}^{eff} \right), \quad (5.18)$$

which is in fact independent of the surface texture. Hence, we dub \tilde{F} in Eq. (5.18) as the normalised driving force. Eq. (5.18) has a clear and intuitive physical interpretation: it corresponds to the preferential wetting of the droplet on the region exhibiting the majority of solid or lubricant surface. Without any loss of generality, let us assume that the gradient in $\varphi_s(x)$ is positive, i.e. the solid fraction becomes denser with increasing x . When $\cos \theta_{dg|s}^{eff} > \cos \theta_{dg|l}^{eff}$, the droplet prefers to wet the solid rather than the lubricant. Therefore, the droplet moves toward the solid majority surface (denser solid area). In contrast, when $\cos \theta_{dg|s}^{eff} < \cos \theta_{dg|l}^{eff}$, the droplet moves toward lubricant majority surface (sparser solid area).

5.3 Demonstration of Bidirectional Motion Using Simulations and Experiments

We have argued that the normalised driving force \tilde{F} is independent of the surface patterning. We will now demonstrate this using simulations and experiments.

In order to validate Eq. (5.18), we need to know the values of $\cos\theta_{dg|s}^{eff}$ and $\cos\theta_{dg|l}^{eff}$, which depend on the wetting angles and the surface tensions of the system. In our simulations, we have the freedom to determine these values. Hence, exploring the parameters to test the driving force is relatively easy. However, our current model is not suitable for the case when the lubricant is encapsulating the droplet. To test the generality of our theory, we performed experiments for both droplet encapsulation and non-encapsulation cases.

Let us first discuss the case when the droplet is not encapsulated by the lubricant. In this case $\gamma_{eff} = \gamma_{dg}$ and the normalised driving force becomes

$$\tilde{F} = (\cos\theta_{dg|s} - \cos\theta_{dg|l}), \quad (5.19)$$

with

$$\cos\theta_{dg|s} = \frac{\gamma_{sg} - \gamma_{sd}}{\gamma_{dg}}, \quad \cos\theta_{dg|l} = \frac{\gamma_{lg} - \gamma_{ld}}{\gamma_{dg}}. \quad (5.20)$$

The angles $\theta_{dg|s}$ and $\theta_{dg|o}$ are the contact angles of the droplet on the smooth solid surface (Young's contact angle) and on the lubricant surface respectively. Typically $\theta_{dg|s}$ can be measured directly using drop shape analyser or goniometer. $\cos\theta_{dg|l}$ can be calculated from Eq. (5.20) if the corresponding surface tensions (γ_{lg} , γ_{ld} , and γ_{dg}) are known.

For the case where the droplet is encapsulated by the lubricant, following McHale *et al.* [104], we use $\gamma_{eff} = \gamma_{lg} + \gamma_{ld}$ and $\cos\theta_{dg|l}^{eff}$ can be calculated as

$$\cos\theta_{dg|l}^{eff} = \frac{\gamma_{lg} - \gamma_{ld}}{\gamma_{lg} + \gamma_{ld}}. \quad (5.21)$$

Conceptually, $\theta_{dg|s}^{eff}$ corresponds to the contact angle of an encapsulated droplet on a smooth solid surface surrounded by gas. This value is different from $\theta_{dg|s}$, the contact angle of a (bare) droplet on a smooth solid surface surrounded by gas. To compute $\theta_{dg|s}^{eff}$, we can use the relation

$\gamma_{sg} - \gamma_{sd} = \gamma_{dg} \cos \theta_{dg} = \gamma_{eff} \cos \theta_{dg|s}^{eff}$. As such,

$$\cos \theta_{dg|s}^{eff} = \frac{\gamma_{dg}}{\gamma_{lg} + \gamma_{ld}} \cos \theta_{dg|s}. \quad (5.22)$$

Eqs. (5.20-5.22) allow us to calculate \tilde{F} and validate our theory via simulations and experiments when $\theta_{dg|s}$, γ_{dg} , γ_{lg} , and γ_{ld} are known. Reference [15], for example, provides the surface tension data for common liquids.

5.3.1 Simulations

The simulations performed in this chapter are done using the lattice Boltzmann method. As shown in Fig. 5.3, we carry out the simulations with three different setups: full 3D simulations, quasi 3D simulations, and 2D simulations.

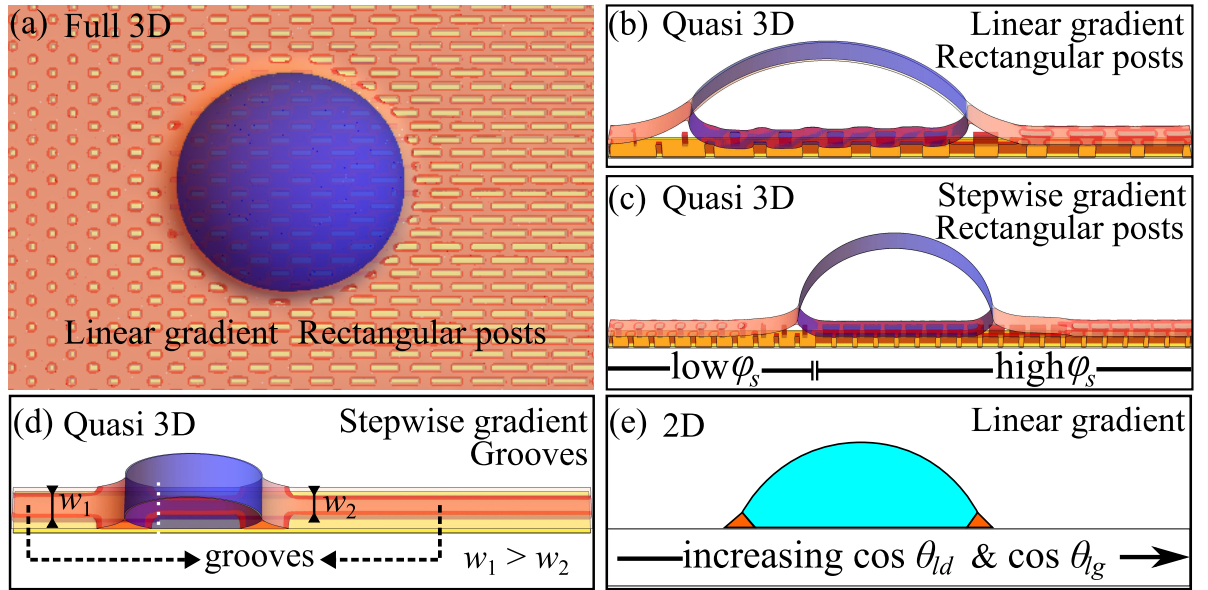


Figure 5.3: Various simulation setups of droplets on LIS with topographical gradients. (a) Full 3D simulation setup for droplets on linear gradient of rectangular posts in a hexagonal arrangement. (b-c) Quasi 3D simulation setups respectively for linear and stepwise gradient of rectangular posts. (d) Quasi 3D simulation setup for stepwise gradient of grooves. w_1 and w_2 are the width of the grooves. (e) A 2D simulation setup where the wetting gradient is represented by the linear variation of $\cos \theta_{ld}$ and $\cos \theta_{lg}$.

The box size for the full 3D simulations is set to be $L_x \times L_y \times L_z = 480 \times 320 \times 100$ lattice units. The surface texture consists of rectangular posts in the $x - y$ plane arranged in a hexagonal lattice. Each post has a fixed height and width given by 10 and 5 lattice units respectively. The post length l is varied by increasing 2 lattice units for each subsequent post in the x direction. The post-centre-to-centre distance is maintained at 30 lattice units in the

x -direction. In the y -direction, the distance between two rows of posts is set at 10 lattice units. To create the hexagonal arrangement, the even and odd rows are shifted by 15 lattice units in the x direction. The lubricant is initiated to fill the corrugation, and then a hemispherical droplet with a radius $R = 150$ lattice units is placed on top of the solid-lubricant composite surface.

For the quasi 3D simulations, the box size is set to be $L_x \times L_y \times L_z = 480 \times 20 \times 100$ lattice units, and a cylindrical droplet with radius $R = 150$ lattice units is placed on top of the solid-lubricant composite surface. We have used three types of surface texturing. First, a linear gradient is employed, akin to the full 3D case, except that only two rows of posts in the y direction are explicitly simulated. The second and third types of surface textures used in the quasi 3D simulations are the stepwise gradient of rectangular posts and stepwise gradient of grooves.

Lastly, for the 2D simulations, the box size is set to be $L_x \times L_z = 480 \times 100$ lattice units. In the 2D simulations, the surface textures are not simulated explicitly. Instead it is represented by varying the effective lubricant-droplet contact angle $\theta_{ld}(x)$ and the effective lubricant-air contact angle $\theta_{lg}(x)$ such that [28]

$$\cos \theta_{ln}(x) = \varphi_s(x) \cos \theta_{ln}^Y + (1 - \varphi_s(x)), \quad (5.23)$$

where the subscript $n = d, g$ and $\cos \theta_{ln}^Y$ is the contact angle on the smooth flat surface. A hemispherical liquid droplet with a radius $R = 120$ LB unit is initiated on top of the solid and a small amount of lubricant is placed around the droplet (initiated as squares of 20×20 lattice units on both sides of the droplet). The 2D simulation setup can be used to explore the phase diagram using relatively fast simulations.

5.3.2 Experiments

Sample Fabrication

The experimental investigation in this study is performed in collaboration with Dr Gaby Launay and Dr Gary Wells from Northumbria University. We use photolithography to produce surfaces with $60 \mu\text{m}$ deep grooves in the x -direction, as shown in Fig. 5.4. The width of each groove can be tuned (between 10 and $75 \mu\text{m}$) to obtain solid fractions φ_s ranging from 0.1 to 0.9 . This allows us to create topographical gradients along the x -direction by continuously

decreasing the width of the grooves. After fabrication, the geometry of the surfaces is carefully measured using optical profilometry and SEM (Scanning Electron Microscope) imaging.

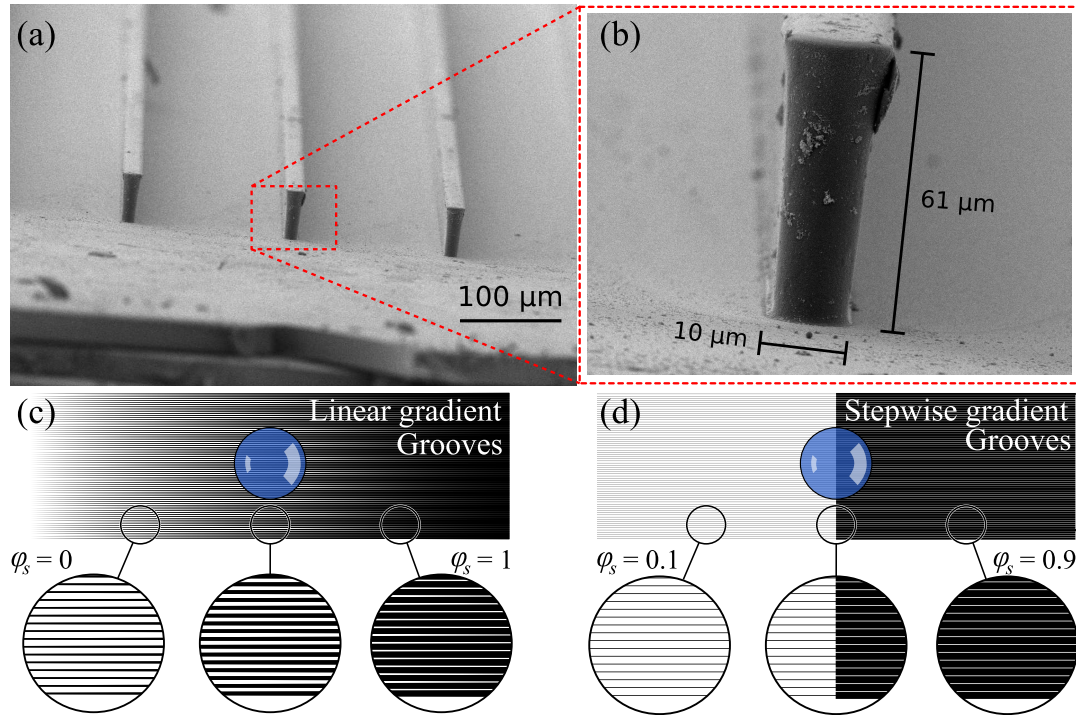


Figure 5.4: (a-b) Scanning electron micrograph revealing the detail of the surface texturing of the samples in this experiment. The structure used in this experiment is microscopic grooves with width variations. (c-d) The pictures of the photolithographic masks for creating samples with (c) linear and (d) stepwise increase of the solid fraction.

To avoid the contact angle hysteresis that would hinder droplet motion, the structured surfaces are treated with SOCAL (Slippery Omniphobic Covalently-Attached Liquid), following the protocol from Wang *et al.* [105], modified for SU-8 substrates. We verify the SOCAL coating by measuring the contact angle ($104.2^\circ \pm 2^\circ$) and contact angle hysteresis ($< 5^\circ$) of a water droplet deposited on a non-structured (flat) region of the sample.

The surfaces are then dipped in a lubricant and left to drain vertically for 10 minutes, in order to fill the grooves and create a LIS. Droplets are then deposited on the imbibed surfaces using a thin needle and their motion is tracked using a camera placed on the side. To rule out the effect of gravity on the droplet motion, the surface is slightly tilted (0.5°) against the expected direction of motion. The procedure is repeated 5 times for each configuration to ensure reproducibility.

Data Collection

In experiment, \tilde{F} can be inferred using Eqs. (5.20)-(5.22) when $\theta_{dg|s}$, γ_{dg} , γ_{lg} , and γ_{ld} are known. However, this is not always the case. Alternatively, when those parameters are not known, \tilde{F} can also be obtained using a graphical method. Here we employ the Cassie-Baxter approximation for the apparent contact angle of a droplet on the composite surface of solid and lubricant at the vanishing meniscus limit [67, 104]

$$\gamma_{eff} \cos \theta_{app} = \gamma_{(s,l)g} - \gamma_{(s,l)d}, \quad (5.24)$$

$$= (\varphi_s \gamma_{sg} + (1 - \varphi_s) \gamma_{lg}) - (\varphi_s \gamma_{sd} + (1 - \varphi_s) \gamma_{ld}), \quad (5.25)$$

$$= \varphi_s (\gamma_{sg} - \gamma_{sd}) + (1 - \varphi_s) (\gamma_{lg} - \gamma_{ld}). \quad (5.26)$$

The value of γ_{eff} is as explained in Eq. (5.15). Dividing both sides with γ_{eff} , we obtain

$$\cos \theta_{app} = \varphi_s \cos \theta_{dg|s}^{eff} + (1 - \varphi_s) \cos \theta_{dg|l}^{eff}, \quad (5.27)$$

$$= \left(\cos \theta_{dg|s}^{eff} - \cos \theta_{dg|l}^{eff} \right) \varphi_s + \cos \theta_{dg|l}^{eff}. \quad (5.28)$$

We can immediately see that the terms inside bracket is \tilde{F} , such that

$$\cos \theta_{app} = \tilde{F} \varphi_s + \cos \theta_{dg|l}^{eff}. \quad (5.29)$$

Thus, if we have the values for $\cos \theta_{app}$ at various solid fractions φ_s , we can compute \tilde{F} from the gradient of the curve. Furthermore, we can infer the values of $\cos \theta_{dg|s}^{eff}$ and $\cos \theta_{dg|l}^{eff}$ by extrapolating $\cos \theta_{app}$ to $\varphi_s = 1$ and $\varphi_s = 0$ respectively. It is also useful to note that this approach works for both encapsulating and non-encapsulating lubricant since it relies on direct contact angle measurement without the need to know the surface tension values of the liquids.

To estimate $\cos \theta_{dg|s}^{eff}$ and $\cos \theta_{dg|l}^{eff}$ using graphical method, the apparent contact angle of a droplet on LIS, θ_{app} , is measured at different φ_s . The measurements are accomplished by depositing a 5 μ l droplet from a thin needle on the sample. Contact angles are then measured from the lateral view of the sessile drop with the help of a camera and an image analysis software. Each measurement is repeated 5 times to reduce the measurement noise and to account for variations in the samples. The samples are imbibed with lubricant between each measurement, to avoid the effect of lubricant depletion from the surface.

Fig. 5.5 shows the measurement of $\cos \theta_{app}$ of various liquid combinations for different φ_s . For the droplet phase, we use water and ethylene glycol, while for the lubricant phase we use ionic liquid, rapeseed oil, sunflower oil, mineral oil, hydrocarbon oil and Krytox.

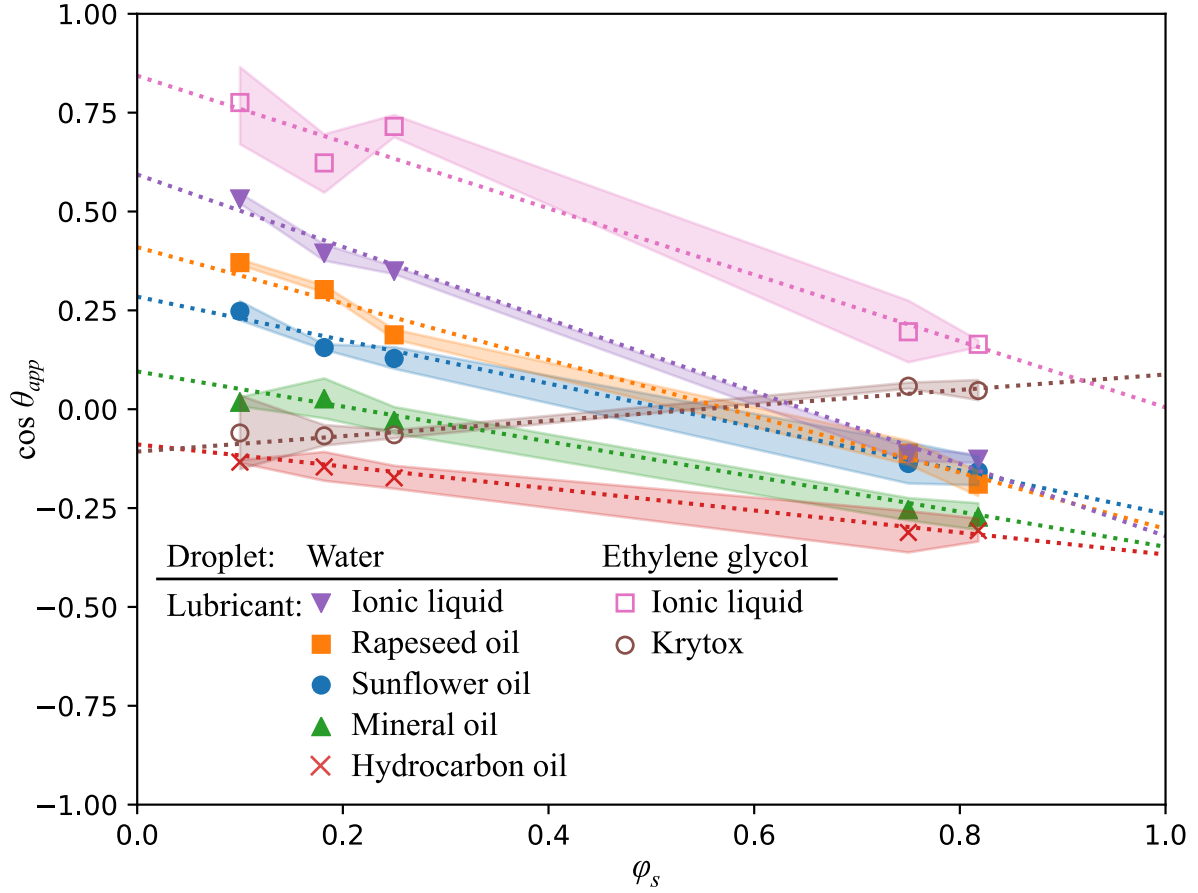


Figure 5.5: Estimation of \tilde{F} for water and ethylene glycol droplets on structured surfaces imbued with various lubricants. Each point is the average of 5 contact angle measurements of sessile droplets. The surrounding dim area represents the standard deviation. Dashed lines are fits of Eq. (5.29) using the least-square method. The gradient of the fits corresponds to \tilde{F} , while extrapolations of those fits to $\varphi_s = 1$ and $\varphi_s = 0$ give a measure of the values of $\cos \theta_{dg|s}^{eff}$ and $\cos \theta_{dg|l}^{eff}$ respectively.

The estimation of $\cos \theta_{dg|s}^{eff}$ and $\cos \theta_{dg|l}^{eff}$ using graphical method as well as using Eqs. (5.20-5.22) are tabulated in Table. 5.1. The droplet direction is tested over a wide range of lubricants, linear and wetting gradients, and lubricant encapsulation and non encapsulation cases. The experimental observations are in agreement with the theoretical predictions based on Eq. (5.18).

Table 5.1: List of liquid droplets and lubricants used in the experiments. Their values of $\cos\theta_{dg|s}^{eff}$ and $\cos\theta_{dg|l}^{eff}$ are either calculated using Eqs. (5.20-5.22) (\dagger) or estimated using the graphical method (\ddagger). The contact angles of the droplets on the flat solid surface $\theta_{dg|s}$ are measured at $(104^\circ \pm 2^\circ)$ and $(87^\circ \pm 2^\circ)$ for water and ethylene glycol respectively. The (*) symbol indicates that the lubricant is encapsulating the droplet, which can be predicted when the surface tension values are known.

Droplet	Lubricant	$\cos\theta_{dg s}^{eff}$	$\cos\theta_{dg l}^{eff}$	\tilde{F}	Direction
\dagger Water	Krytox*	-0.246	-0.493	0.247	Denser
\dagger Water	Diiodomethane	-0.242	0.277	-0.519	Sparser
\dagger Water	FC70*	-0.247	-0.492	0.245	Denser
\dagger Water	Silicone oil*	-0.278	-0.369	0.091	Denser
\dagger Water	Toluene*	-0.376	0.224	-0.601	Sparser
\ddagger Water	Sunflower oil	-0.267	0.292	-0.560	Sparser
\ddagger Water	Rapeseed oil	-0.305	0.417	-0.722	Sparser
\ddagger Water	Mineral oil	-0.350	0.103	-0.454	Sparser
\ddagger Water	Hydrocarbon oil	-0.370	-0.081	-0.289	Sparser
\ddagger Water	Ionic liquid	-0.323	0.601	-0.924	Sparser
\ddagger Ethylene Glycol	Krytox	0.096	-0.109	0.205	Denser
\ddagger Ethylene Glycol	Ionic liquid	0.002	0.851	-0.849	Sparser

5.3.3 Phase Diagram

To show the agreement between our theory with experiments and simulations, we combine the simulation and the experimental results into a phase diagram. Fig. 5.6 shows the phase diagram for the driving force (\tilde{F}), predicted by Eq. (5.18) (colormap), and the corresponding droplet motion observed in the numerical simulations and the experiments (symbols). The upper section of the phase diagram corresponds to an expected driving force directed towards the denser solid regions, while the lower section towards the sparser solid regions. The colour of the symbols represents motion to the denser (blue) or sparser (red) solid fraction area.

Our numerical simulations and experimental results show that the mechanism leading to bidirectional motion holds for various kinds of droplet-lubricant combinations. In addition, the mechanism also holds for different types of surface topographies, and thus supports that the relevant control parameter linked to the topography of the solid is the solid fraction φ_s . Specifically, we consider three different solid surface geometries in our simulations: (1) full 3D simulations with the linear gradient of rectangular posts; (2) quasi 3D simulations with the linear gradient of rectangular posts, and stepwise gradient of rectangular posts and grooves; and (3) 2D simulations. Similarly, our experimental results correspond to two different solid surface geometries: stepwise and linear gradients; and, crucially, show that the direction of motion of a droplet on a given topography can be switched by choosing the interfacial tensions.

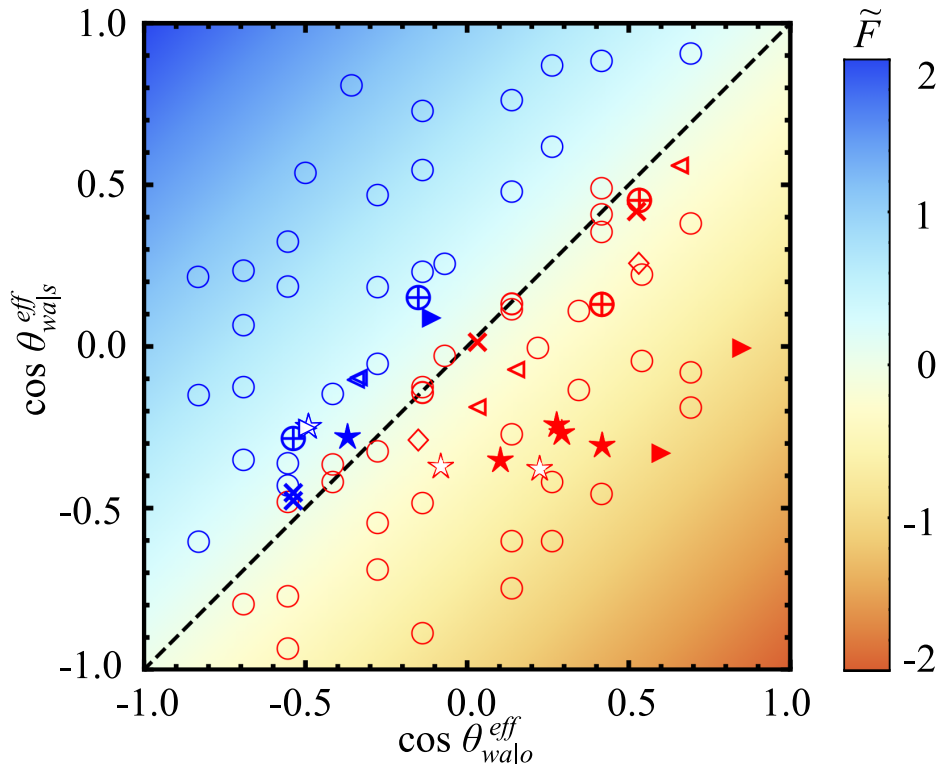


Figure 5.6: Confirmation of the bidirectional motion of droplets on LIS with a topographical gradient, as predicted in Eq. (5.18) via simulations and experiments. The blue and red data points indicate that the droplets were observed to move to the higher or lower solid fraction area, which respectively correspond to positive and negative \tilde{F} . The following symbols correspond to the numerical data points: (\oplus) full 3D simulations with linear gradient of rectangular posts; (\triangleleft) quasi 3D simulations with linear gradient of rectangular posts, and (\diamond) stepwise gradient of rectangular posts and (\times) grooves; and (\circ) 2D simulations. The following symbols correspond to the experimental data points: (\star) stepwise and (\blacktriangleright) linear gradients. The hollow \star and \triangleright data points indicate the lubricant encapsulation case.

Moreover, here we show that the bidirectional motion is also present in the case of lubricant encapsulation.

The confirmation of this bidirectional motion reveals yet another role of the lubricant in LIS system. The interplay of the interfacial forces at the meniscus gives rise to the preferential wetting of the droplet towards the solid or the lubricant majority surfaces. Interestingly, this effect happens when the lubricant does not wet the solid completely both in the presence of gas or droplet phases. The use of partially wetting lubricants can lead to the contact line pinning, which is a disadvantage. Nevertheless, it is demonstrated here that the use of partially wetting lubricants can add a new functionality.

5.3.4 The 2D Cases

The results presented in Fig. 5.6 show a good agreement between the simulations with the prediction. Few exceptions are present for the 2D simulations, where some of the red data points cross the diagonal line in the phase diagram. Those data points indicate that the droplets move toward the opposite direction dictated by Eq. (5.18). To understand this small discrepancy, we need to describe the force balance of the 2D system.

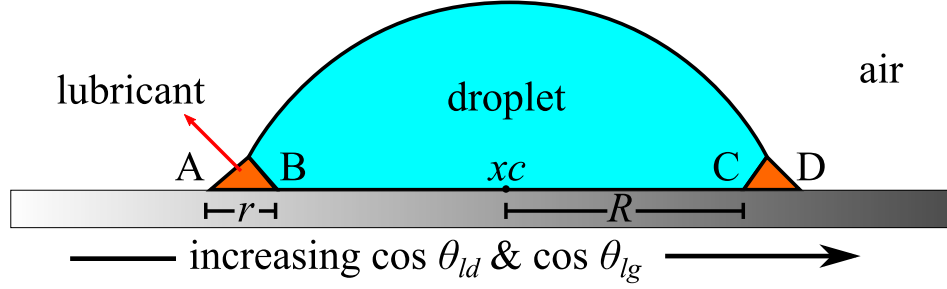


Figure 5.7: Sketch of the 2D simulation system. The three phase contact lines are indicated by A, B, C and D . x_c , R and r are respectively the droplet centre position, droplet base radius, and the width of the lubricant ridge.

Fig. 5.7 is the sketch of the 2D simulation system. The wetting angles of the lubricant on the solid surface is varied with x such a way that it mimics the effect of varying the surface texturing φ_s as follows

$$\cos \theta_{ln}(x) = \varphi_s(x) \cos \theta_{ln} + (1 - \varphi_s(x)), \quad (5.30)$$

where $n = d, g$. The total force balance is given by

$$F_{2D} = \Gamma_{out} + \Gamma_{in} \quad (5.31)$$

where

$$\Gamma_{out} = [\gamma_{sl} - \gamma_{sg}]_A + [\gamma_{sg} - \gamma_{sl}]_D \quad \text{and} \quad \Gamma_{in} = [\gamma_{sd} - \gamma_{sl}]_B + [\gamma_{sl} - \gamma_{sd}]_C. \quad (5.32)$$

Here, the subscript A, B, C and D the three point contact lines in Fig. 5.7. Using the definition of the Young's contact angle, Γ_{out} can be written as

$$\Gamma_{out} = \gamma_{lg} \cos \theta_{lg}(D) - \gamma_{lg} \cos \theta_{lg}(A), \quad (5.33)$$

$$= \gamma_{lg} (\cos \theta_{lg} - 1) (\varphi_s(D) - \varphi_s(A)). \quad (5.34)$$

The linear increase of φ_s can be expressed as $\varphi_s(x) = mx + \varphi_{s0}$ where m is the gradient of the solid fraction and φ_{s0} is the value of φ_s at $x = 0$. Using this definition, we can write

$$\varphi_s(D) - \varphi_s(A) = (m(xc + R + r) + \varphi_{s0}) - (m(xc - R - r) + \varphi_{s0}), \quad (5.35)$$

$$= 2m(R + r). \quad (5.36)$$

Therefore Γ_{out} can be written as

$$\Gamma_{out} = 2m(R + r)\gamma_{lg}(\cos \theta_{lg} - 1). \quad (5.37)$$

Following similar route, we also obtain

$$\Gamma_{in} = 2m(R)\gamma_{ld}(1 - \cos \theta_{ld}). \quad (5.38)$$

Finally, we can express the total force in 2D configuration as

$$F_{2D} = 2m(R + r)\gamma_{lg}(\cos \theta_{lg} - 1) + 2m(R)\gamma_{ld}(1 - \cos \theta_{ld}), \quad (5.39)$$

$$= 2mR[\gamma_{lg}(\cos \theta_{lg} - 1) + \gamma_{ld}(1 - \cos \theta_{ld})] + 2mr\gamma_{lg}(\cos \theta_{lg} - 1). \quad (5.40)$$

We can notice that the terms inside the square bracket in Eq. (5.40) is the same as the prefactor in Eq. (5.14), which is none other than $\gamma_{dg}\tilde{F}$. Thus, we can write the total force in 2D configuration as

$$F_{2D} = 2m(R\gamma_{dg}\tilde{F} + r\gamma_{lg}(\cos \theta_{lg} - 1)). \quad (5.41)$$

The second term in Eq. (5.41) is similar to the meniscus contribution of the driving force expressed in Eq. (5.12). We can see that the second term is always negative as long as θ_{lg} is finite. As a result, this contribution causes the droplets to move toward sparser solid area. This explains why some data points from the 2D simulations in Fig. 5.6 disagree with Eq. (5.18). For those data points, the values of the normalised driving force $\tilde{F} \approx 0$ (near the diagonal line). As such, the meniscus contribution to the driving force becomes apparent.

5.4 Droplet Dynamics under Different Surface Textures

A key advantage of the lattice Boltzmann simulation method is that it allows us to explore the effect of surface textures on the dynamics of the droplet. In this section, we start by studying different textures which share the same overall solid fraction gradient across the simulation domain. We define the normalised texture gradient as

$$\tilde{\alpha} = \frac{\Delta\varphi_s}{\Delta x} R, \quad (5.42)$$

where $\Delta\varphi_s/\Delta x$ is the texture gradient per unit length across the simulation domain and R is the droplet base radius.

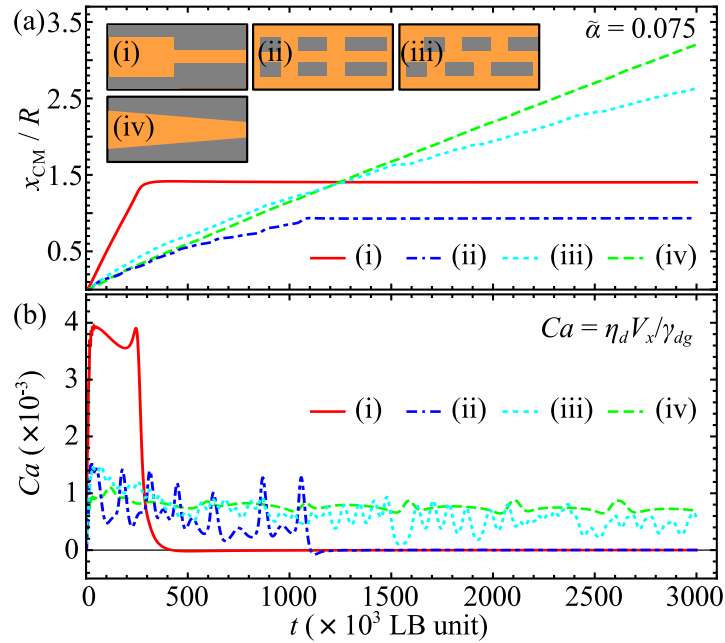


Figure 5.8: Droplet trajectories for different surface textures: (i) a stepwise groove, (ii) and (iii) linear rectangular posts with square and hexagonal arrangements respectively, and (iv) a linear groove. The normalised texture gradient $\tilde{\alpha}$ is kept the same. (a) The normalised droplet centre of mass position x_{CM}/R versus time t . (b) Droplet mobility, represented by the capillary number Ca , versus time t . Here, η_d , V_x and γ_{dg} are the droplet viscosity, the droplet centre of mass velocity, and the droplet-air surface tension.

Fig. 5.8(a) shows the droplet position x_{CM} (normalised by its base radius R) as a function of time when moving across a surface patterned with (i) a stepwise groove, (ii) and (iii) linear rectangular posts with square and hexagonal arrangements, and (iv) a linear groove. On the stepwise gradient groove (case i), the droplet velocity is the fastest. However, the droplet stops travelling when it no longer experiences a topographical gradient. For continuous

droplet motion, we anticipate that a linear texture gradient is needed and here we compare three different surface textures. On rectangular posts with square arrangements (case ii), the droplet, in fact, only moves a short distance before contact line pinning dominates. Changing the post arrangement into a hexagonal array (case iii) helps to advance the contact line by distributing the pinning points [68], which are located at the edge of the post. As the result, the droplet can move much further on the substrate. Contact line pinning is minimised using the linear groove (case iv). In this case, the contact line can slide along the edges of the grooves as the droplet moves. Thus, this surface patterning leads to the highest droplet mobility.

The effect of contact line pinning on the droplet motion can be further observed in Fig. 5.8(b). Rather than a constant velocity, we find a variation in the droplet velocity with time. The stick-slip motion can be observed most clearly for cases (ii) and (iii) for the rectangular posts, and they correspond to pinning and depinning events of the contact lines. Case (iv) also shows a small variation in the droplet velocity. This is because we have simulated the linear groove using a staircase approximation, where the linear increase in φ_s is represented by a small staircase-like gradual increase. The observed acceleration and deceleration occur at the corners of the staircase.

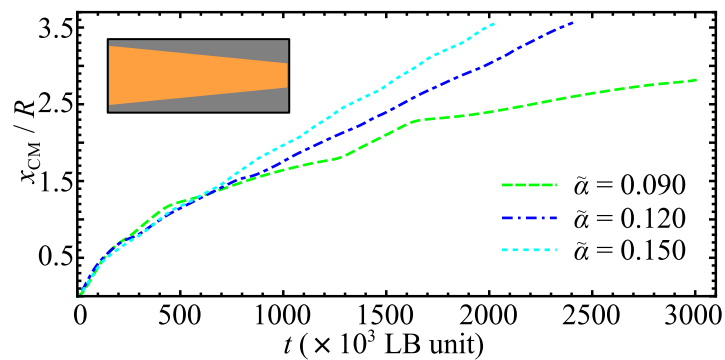


Figure 5.9: The normalised droplet centre of mass position x_{CM}/R versus time t on linear grooves with different normalised texture gradient $\tilde{\alpha}$.

In Fig. 5.9, we have also studied the effect of $\tilde{\alpha}$ on the droplet mobility, focussing on the case of linear grooves. We can observe that the larger $\tilde{\alpha}$, the faster the droplet since the texture gradient generates a larger driving force. However, at the same time, the larger $\tilde{\alpha}$ the smaller the distance that the droplet can travel for the same end-to-end difference in the solid fractions. This contradictory constraint is an important consideration for potential applications, such as in drop sorting. Employing large texture gradients increase the throughput of the sorting, but it limits the spatial distance over which the droplets can be distinctly separated.

5.5 Potential Applications

Our observation of spontaneous bidirectional droplet motion on LIS with topographical gradient can be exploited for a number of applications. In particular, we now propose ways of utilising this effect for droplet classification/sorting in the context of droplet microfluidics.

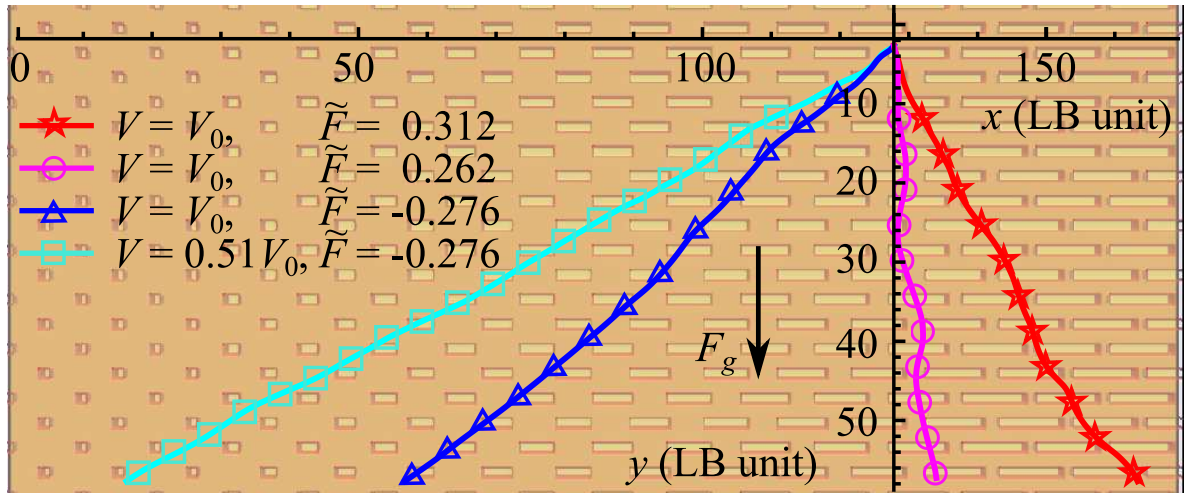


Figure 5.10: The trajectories of droplets on LIS with linear topographical gradient. Here, we test three droplets of the same volume V but with different values of \tilde{F} (★, ⊖ and △), and two droplets of the same \tilde{F} but with different V (△ and ⊞).

The first strategy is to use a linear topographical gradient, as illustrated in the background of Fig. 5.10. This concept is demonstrated using the lattice Boltzmann simulations. We start by simulating three droplets of the same size but with different \tilde{F} 's, as represented by the symbols ★, ⊖ and △. These droplets are directed into three different trajectories. As we have discussed above, the sign of the driving force due to the wetting gradient depends on \tilde{F} : negative \tilde{F} leads to droplet motion to the sparser solid area, while positive \tilde{F} biases the droplet to the denser solid area. Comparing the two cases with positive \tilde{F} , we can also see that the droplet with larger \tilde{F} is deflected further from the vertical line due to the stronger driving force from the wetting gradient. Next, we study two droplets of the same \tilde{F} but with different volumes, shown by the symbols △ and ⊞. Since the smaller droplet is less affected by F_g , we find its trajectory is deflected further from the vertical line, compared to the larger droplet. These results suggest that by combining gravity and the linear wetting gradient, we can classify/sort droplets based on their volume and their interfacial property at the same time.

The advantage of the linear gradient design is that it can smoothly distinguish droplets

of varying radii. However, the droplet trajectory can be quite sensitive to the initial droplet position; and in some cases, it is adequate, if not preferable, to sort droplets within a given size window. Thus, an alternative drop sorting strategy is to use multi-sections of stepwise topographical gradients, where the sample is divided into multiple areas with different φ_s . An example of this strategy is shown in the background of Fig. 5.11, obtained using the lattice Boltzmann simulation method.

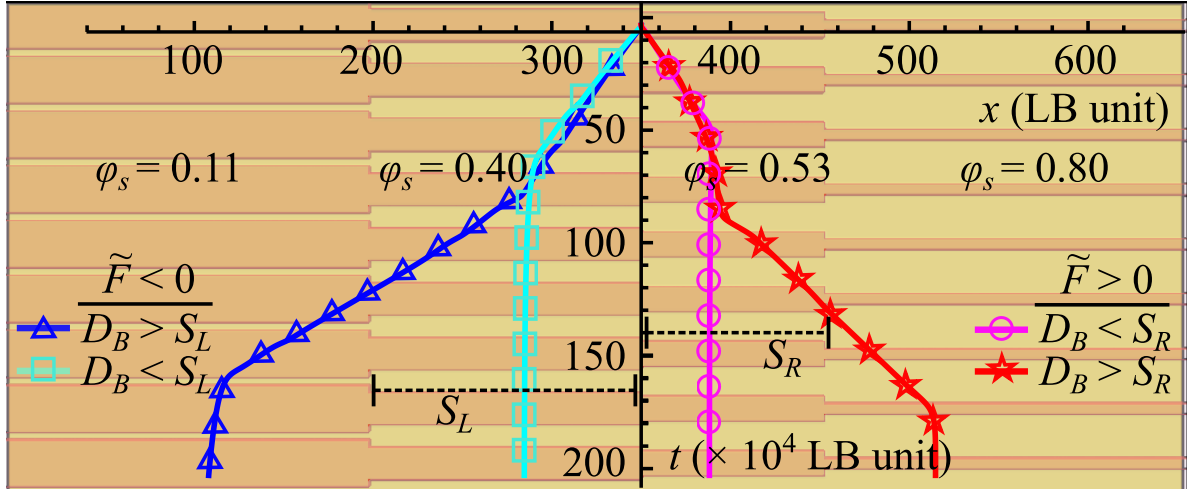


Figure 5.11: Potential applications of LIS with topographical gradient. With multi sections of stepwise gradients, droplets can be classified from their sizes, represented by their base diameter D_B , by controlling the sections' width, here S_L and S_R .

The sign of \tilde{F} controls the direction of droplet motion. Droplets with negative \tilde{F} (represented as \triangleleft and \triangleleft) are shifted to the $\varphi_s = 0.40$ section while those with positive \tilde{F} (\star and \ominus) are shifted to the $\varphi_s = 0.53$ section. The downward motion in Fig. 5.11 is due to gravity. In this sorting strategy, the widths of the sections are important (in this case, S_L and S_R). Droplets whose base diameter D_B are larger than S_L or S_R will be shifted to the outer left ($\varphi_s = 0.11$, \triangleleft) and right ($\varphi_s = 0.80$, \star) sections, while smaller droplets will stay in the $\varphi_s = 0.40$ (\triangleleft) and $\varphi_s = 0.53$ (\ominus) sections, since these droplets do not experience the additional wetting gradient.

5.6 Discussion

In this chapter, we have discussed a spontaneous bidirectional motion of droplet on LIS with topographical gradient. In contrast to previous studies describing mono-directional droplet motion on surfaces with topographical gradients, here the droplet can move toward the sparser

or the denser solid fraction area. We investigated the origin of this bidirectional motion by looking into the relevant surface tension forces acting on the droplet. Our analytical theory predicts, and our simulation and experimental results confirmed, that the direction of the motion is determined by a simple physical quantity, $(\cos \theta_{dg|s}^{eff} - \cos \theta_{dg|l}^{eff})$. This quantity can be intuitively interpreted as preferential wetting of the droplet on the solid majority surface or on the lubricant majority surface. The bidirectional motion is also validated over a wide range of surface tension and contact angle combinations, with and without lubricant encapsulation, and for different types of topographical gradients, both in our simulations and experiments. Finally, we propose two designs utilising this bidirectional motion to sort/classify droplets, based on linear gradients and multi sections of the stepwise gradient.

There are a number of avenues of future work to better understand and exploit the novel phenomenon described here. For instance, while we already show here that bidirectional motion applies for different types of topographical gradients, it remains an open problem which types of topographical gradients are optimal. It is also interesting to consider more advanced applications of the bidirectional motion. For example, we can consider the applications of these surfaces for liquid/liquid separation or for directing chemical reactions in a droplet microfluidic device.

CHAPTER 6

Factors Controlling the Pinning Force of Droplets on Liquid Infused Surfaces

Since their inception [55, 57, 58], liquid infused surfaces (LIS) have been prized for their anti-adhesive nature, which results in properties such as the high mobility of liquid droplets and anti-fouling. These properties are highly desirable in a broad range of applications, from marine and medical coatings [106, 107], to non-stick packaging [108], and digital microfluidics [109].

High mobility of a liquid droplet is particularly obtained when the lubricant completely wets the surface texture, as pinning of the droplet on the surface is negated by the intervening lubricant layer. However, the dependency on a fully wetting lubricant often limits the implementation of LIS, both due to the difficulty of finding the suitable lubricant for the desired applications [57, 110], and due to the possibility of lubricant depletion [111–115].

On the other hand, LIS with partially wetting lubricant have increasingly attracted interest, especially with a number of external stimuli shown to allow reversible change of wetting states from slippery to sticky (see for example the recent review [116]). Such surfaces have substantially expanded functionality than the purely slippery surfaces, with the ability to locally change the droplet mobility leading to the demonstration of fog capture even in high winds [117], to introduce bidirectional motion under texture gradients [118], and recently the unprecedented manipulation of both droplets and colloids [119].

It is important therefore to understand pinning from two perspectives: as a problem to be minimised, or as a functional phenomenon to be controlled. However, the quantitative relationship of the pinning force to both the surface roughness and fluid properties has never been systematically studied on LIS.

In this chapter, we numerically study the pinning force and contact angle hysteresis (CAH) of a droplet on LIS. The simulations carried out in this chapter is performed using the phase field energy minimisation method. We begin by developing a model for CAH based on averaged Cassie-Baxter surface approximation. We then observe both advancing and receding contact angles using computer simulations, showing that the simulated CAH closely matches the model results. We, therefore, are able to accurately quantify the hysteresis based on the surface roughness, and the set of fluid-solid and fluid-fluid surface tensions. Further, we derive the total pinning force and demonstrate that our prediction is consistent with experimental observations.

We find that there is a competition between two factors which control the pinning force on LIS, (i) the droplet base perimeter and (ii) the cosine difference between the receding and the advancing angles. Our theory suggests that this competition minimises pinning at the extremes of the apparent contact angle but maximises it at moderate values. Since most reported values of the apparent contact angle are moderate, the roll off angle could be much higher than the estimated CAH. Correspondingly, it is not advisable to use CAH as a measure of liquid repellency for LIS.

6.1 Derivation of Pinning Force and Contact Angle Hysteresis

The pinning force per unit length for a droplet on a dry (not lubricated) textured solid surface is given by [16]

$$f_{dry} = \gamma_{dg} \Delta \cos \theta, \quad (6.1)$$

where γ_{dg} is the surface tension of the droplet with the gas phase and $\Delta \cos \theta = (\cos \theta^R - \cos \theta^A)$ is the difference in the cosine of the receding θ^R and the advancing θ^A contact angles for the droplet-gas-solid contact line.

Compared to other surfaces, the distinguishing feature of LIS is the presence of the lubricant meniscus. As such, the droplet-gas-solid contact line is not present. Instead, we have to consider the compound effect of droplet-gas-lubricant, droplet-lubricant-solid and lubricant-gas-solid contact lines, as illustrated in Fig. 6.1. Semprebon *et al.* have derived an expression for the CAH on LIS using geometrical analysis of the meniscus [67]. Here, we will show that the CAH can also be derived employing a simpler argument based on force balance.

Let us consider a droplet on LIS under the influence of an external force F_{ext} , as shown

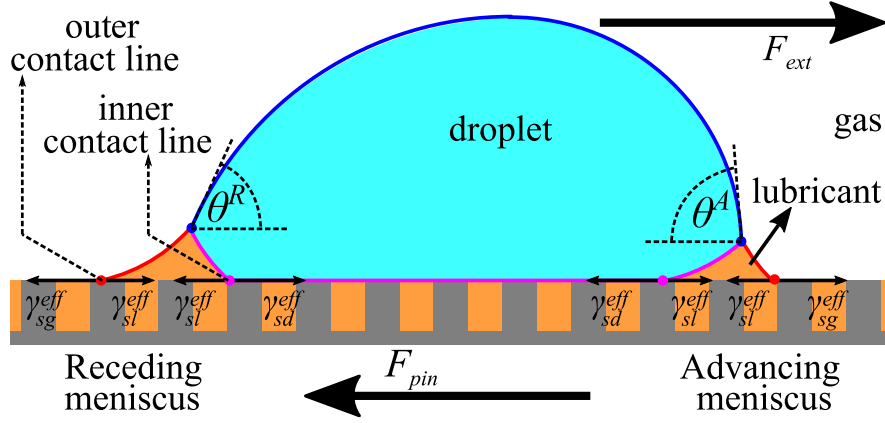


Figure 6.1: Droplet on LIS under influence of an external force F_{ext} . The resisting force due to contact line pinning, F_{pin} , is pointing in the opposite direction. We have also shown the surface tension forces acting on the inner and outer contact lines.

in Fig. 6.1. Here, γ_{sm}^{eff} denotes the effective interfacial tension of LIS with the fluid phase m , with $m = d, g, l$. The subscripts s, d, g and l are to indicate the solid, droplet, gas and lubricant phases respectively. LIS can be considered as a composite surface where φ_s fraction of the surface is solid surface and the remaining $(1 - \varphi_s)$ is the lubricant surface [28]. The effective interfacial tension of the fluid phase phase m with the composite surface can then be written as

$$\gamma_{sm}^{eff} = \varphi_s \gamma_{sm} + (1 - \varphi_s) \gamma_{lm}. \quad (6.2)$$

The pinning force per unit length for a droplet on LIS f_{LIS} can be calculated from the sum of the effective interfacial tensions of this composite surface at the outer and the inner contact lines, as indicated in Fig.6.1. Hence, f_{LIS} is written as

$$f_{LIS} = \left(\left[\gamma_{sg}^{eff} - \gamma_{sl}^{eff} \right]^R + \left[\gamma_{sl}^{eff} - \gamma_{sg}^{eff} \right]^A \right)_{outer} + \left(\left[\gamma_{sl}^{eff} - \gamma_{sd}^{eff} \right]^R + \left[\gamma_{sd}^{eff} - \gamma_{sl}^{eff} \right]^A \right)_{inner}. \quad (6.3)$$

The superscripts A and R indicate the advancing and the receding menisci.

Generally, the terms for the outer and inner contact lines cannot simply be added together since they are to be integrated over different lengths (i.e. the inner and the outer droplet base perimeters). However, in the limit where the meniscus size is small compared to the droplet, the outer and the inner droplet base perimeters can be taken to be approximately the same [67, 69]. In this approximation, we can introduce the effective lubricant wetting angles

as

$$\cos \theta_{lg}^{eff} = \frac{\gamma_{sg}^{eff} - \gamma_{sl}^{eff}}{\gamma_{lg}}, \quad \cos \theta_{ld}^{eff} = \frac{\gamma_{sd}^{eff} - \gamma_{sl}^{eff}}{\gamma_{ld}}, \quad (6.4)$$

such that Eq. (6.3) can be written into

$$f_{LIS} = \left(\left[\gamma_{lg} \cos \theta_{lg}^{eff} - \gamma_{ld} \cos \theta_{ld}^{eff} \right]^R - \left[\gamma_{lg} \cos \theta_{lg}^{eff} - \gamma_{ld} \cos \theta_{ld}^{eff} \right]^A \right). \quad (6.5)$$

6.1.1 Depinning Mechanisms

The simulation method used in this chapter is the phase field energy minimisation method. This method is preferred over the lattice Boltzmann method since the dynamic of the fluid is not the main interest of this study. We have also modified the total free energy given in Eq. (2.1) by adding a pressure term

$$\Psi = \int_V (\Psi_{bulk} + \Psi_{interface}) dV + \int_S \Psi_{surface} dS - \Delta P V_l, \quad (6.6)$$

where ΔP and V_l are the Laplace's pressure and the volume of the lubricant phase. This pressure term allows us to control the Laplace's pressure of the lubricant-gas and the lubricant-droplet interfaces. Since the volume of the fluids is not constrained, their value can increase or decrease as long as the pressure constrain is satisfied.

Numerous simulation studies have been conducted to investigate the effective contact angles when a droplet is about to move on a dry textured surface [54, 81]. In such cases, we typically consider two contact line depinning mechanisms, corresponding to the advancing and receding contact lines of the droplet-gas interfaces. In contrast, for LIS, we must consider how both the lubricant-droplet and lubricant-gas interfaces advance and recede.

For an advancing contact line on a dry textured surface, the front part of the droplet typically advances by *bridging* to the front subsequent post. For LIS, such a contact line bridging mechanism is also observed for the lubricant-droplet interface at the advancing meniscus as well as the lubricant-gas interface at the receding meniscus [120]. Therefore, the effective contact angle for both interfaces are zero when they depin, $[\theta_{lg}^{eff}]^R = 0$ and $[\theta_{ld}^{eff}]^A = 0$.

There are various mechanisms for the receding contact line to depin from the post, which

depend on the geometry and the surface energy of the post [54, 121]. For LIS, this is relevant for understanding the lubricant-droplet interface at the receding meniscus and the lubricant-gas interface at the advancing meniscus. Here we will focus on a square array of rectangular posts, and we can use our numerical approach to determine the relevant depinning mechanism. To do this, we start by simplifying the system studied and isolate the advancing lubricant-gas and the receding lubricant-droplet interfaces, as shown in Fig. 6.2(a-b).

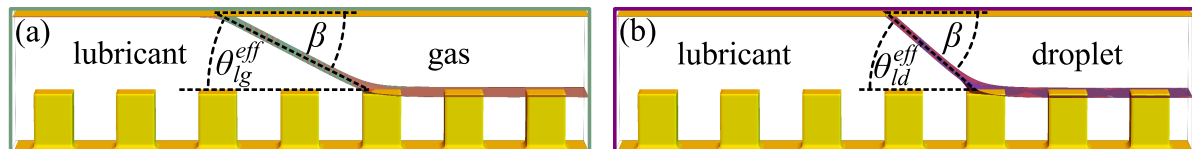


Figure 6.2: Simulations of the depinning mechanism using quasi 3D setups for (a) the advancing lubricant-gas and (b) the receding lubricant-droplet interfaces. The top contact angle β can be tuned to find θ_{lg}^{depin} and θ_{ld}^{depin} .

To reduce the computational cost, we concentrate our numerical study in the region close to the contact line. We have used a quasi 3D setup, where only a single row of posts are explicitly simulated at the bottom surface, a smooth wall is used for the top surface, and periodic boundary condition is applied in the direction perpendicular to the row of posts. At both ends of the simulation box, zero gradient boundary condition is applied to allow fluid phases to enter or exit the simulation box. Two fluid phases are then introduced in each half of the simulation domain, and the two phases have equal pressure such that their interface is flat.

The top contact angle β can be controlled to measure the depinning angles. This is performed by varying β and recording its critical angle, β_{max} , for the stability of the corresponding interfaces. Simple geometry then dictates that β_{max} is the critical depinning angle for $[\theta_{lg}^{eff}]^A$ and $[\theta_{ld}^{eff}]^R$.

The typical development of a receding interface is shown in Fig. 6.3(a) upon varying β . The interface is initially stable and pinned at the corner of the square post (purple line). Increasing β deforms the interface (blue line) until we eventually reach β_{max} (cyan line). Here the interface detaches from the corner and the contact line slides on top of the post (see green, orange and red lines), while maintaining a constant contact angle at the top plate. For this *simple* depinning mechanism, we can write the expression of force balance per unit length of

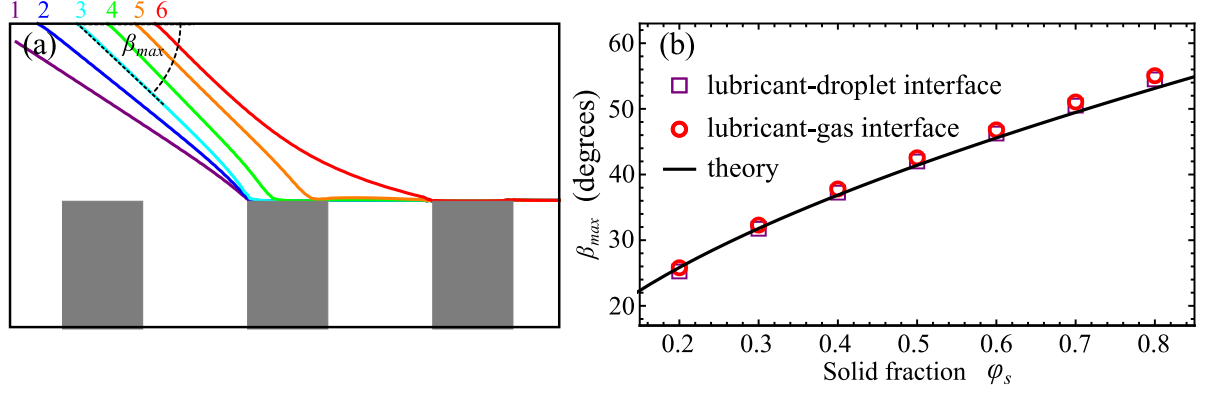


Figure 6.3: (a) The typical evolution of the contact line when β is increased. For $\beta < \beta_{max}$ (purple and blue lines), the contact line is pinned. At $\beta = \beta_{max}$ (cyan, green, orange and red lines), the contact line slides on top of the post. (b) The measurement of β_{max} for different φ_s and its comparison with theory provided in Eq. (6.10). Here, we have used $\theta_{ld} = \theta_{lg} = 60^\circ$.

the top and the bottom contact lines at $\beta = \beta_{max}$, just before the contact lines move:

$$(\gamma_{sm}^{top} - \gamma_{sl}^{top}) + (\gamma_{sm}^{eff} - \gamma_{sl}^{eff}) = 0, \quad (6.7)$$

$$(\gamma_{sm}^{top} - \gamma_{sl}^{top}) + ((\varphi_s \gamma_{sm} + (1 - \varphi_s) \gamma_{lm}) - (\varphi_s \gamma_{sl} + (1 - \varphi_s) \gamma_{ll})) = 0, \quad (6.8)$$

and $m = d, g$. Using the definition of Young's contact angle, we can simplify the above expression into

$$\cos \theta_{lm}^{top} + \varphi_s \cos \theta_{lm} + (1 - \varphi_s) = 0, \quad (6.9)$$

where $\theta_{lm}^{top} = \pi - \beta_{max}$. Thus, the critical angle is given by:

$$\cos \beta_{max} = \varphi_s \cos \theta_{lm} + (1 - \varphi_s). \quad (6.10)$$

As an illustrative example, Fig. 6.3(b) shows the measured β_{max} for different φ_s and Young's angles $\theta_{ld} = \theta_{lg} = 60^\circ$. We consistently find this depinning mechanism to be at play for the surface textures considered in this work (square arrays of square posts). Similarly good agreement between numerical results and the prediction in Eq. (6.10) is also obtained for other Young's contact angles.

6.1.2 The Advancing and the Receding Angles

Following the previous subsection, the depinning angles for the advancing lubricant-gas and the receding lubricant-droplet interfaces are given by

$$\cos \theta_{ld}^{depin} = \varphi_s \cos \theta_{ld} + (1 - \varphi_s), \quad (6.11)$$

$$\cos \theta_{lg}^{depin} = \varphi_s \cos \theta_{lg} + (1 - \varphi_s). \quad (6.12)$$

Substituting Eqs. (6.11) and (6.12), as well as $[\theta_{lg}^{eff}]^R = [\theta_{ld}^{eff}]^A = 0$, into Eq. (6.5), we obtain the full expression of the pinning force per unit length for a droplet on LIS:

$$f_{LIS} = [\gamma_{lg} - \gamma_{ld} (\varphi_s \cos \theta_{ld} + (1 - \varphi_s))]^R - [\gamma_{lg} (\varphi_s \cos \theta_{lg} + (1 - \varphi_s)) - \gamma_{ld}]^A. \quad (6.13)$$

One important observation from Eq. (6.13) is that the magnitude of the pinning force does not actually depend on the droplet-gas surface tension, γ_{dg} , which distinguishes the case of pinning on LIS to pinning on the other solid surfaces. Nonetheless, to allow comparisons with other solid surfaces, it is useful to write Eq. (6.13) in the following form

$$f_{LIS} = \gamma_{dg} \Delta \cos \theta, \quad (6.14)$$

where $\Delta \cos \theta = \cos \theta^R - \cos \theta^A$, and the receding and the advancing contact angles are respectively defined as

$$\cos \theta^R = \frac{\gamma_{lg}}{\gamma_{dg}} - \frac{\gamma_{ld}}{\gamma_{dg}} (\varphi_s \cos \theta_{ld} + (1 - \varphi_s)), \quad (6.15)$$

$$\cos \theta^A = \frac{\gamma_{lg}}{\gamma_{dg}} (\varphi_s \cos \theta_{lg} + (1 - \varphi_s)) - \frac{\gamma_{ld}}{\gamma_{dg}}. \quad (6.16)$$

These receding and the advancing contact angles are interpreted as the apparent contact angles at the front and rear of the lubricant meniscus as a liquid droplet depins on LIS (see Fig. 6.1). Here, we also define CAH as $\Delta \theta = \theta^A - \theta^R$.

It is worth noting that, in this work, we have focussed on the case where the lubricant does not encapsulate the droplet. When the lubricant encapsulates the droplet, the effective droplet-gas surface tension becomes $\gamma_{dg}^{eff} = \gamma_{lg} + \gamma_{ld}$ [104].

6.2 The Effect of Changing Fluid and Solid Properties

Eqs. (6.15) and (6.16) suggest the advancing and receding angles are controlled by the surface tensions ($\gamma_{dg}, \gamma_{lg}, \gamma_{ld}$), the lubricant wetting angles (θ_{lg}, θ_{ld}), and the fraction of solid φ_s . In this subsection we will systematically test the validity and accuracy of Eqs. (6.15) and (6.16) for predicting the advancing and receding angles.

To do this, rather than simulating the whole droplet (left panel of Fig. 6.4), we will focus on the region around the lubricant meniscus (right panel of Fig. 6.4). In this simulation setup, the three fluid phases are present; and as in the setup in Fig. 6.2, the movement of the meniscus is controlled by the contact angle at the top plate, β . The maximum angle β_{max} for which the meniscus remains stable corresponds to the advancing angle θ^A ; while the minimum angle β_{min} is the receding angle θ^R .

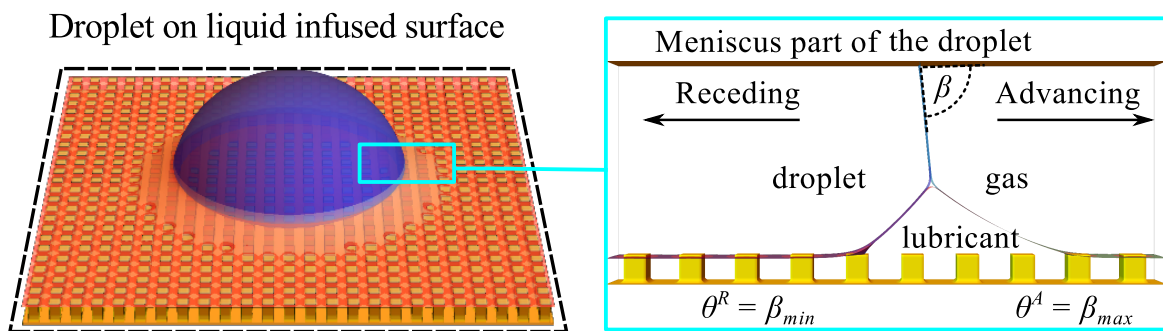


Figure 6.4: Simulation setup for the advancing and the receding angles. To reduce computational costs, we focus on simulating the region around the lubricant meniscus. By varying β , we are able to investigate when the meniscus advances or recedes.

We first investigate the role of meniscus size on the advancing and receding angles. The meniscus size can be controlled by varying the volume of the lubricant phase. Here, we parameterise the meniscus size \tilde{M} by taking the ratio of the cross sectional area of the lubricant meniscus to the unit cell of the post. Furthermore, we set the pressure in the droplet and gas phases to be equal, such that we are always in the vanishing meniscus regime [67] where the radius of the curvature of the lubricant meniscus is much smaller compared to the radius of curvature for the droplet-gas interface. From Fig. 6.5(a) we can see that the advancing and the receding angles are independent of the meniscus size in this limit.

The effect of the lubricant wetting angles, θ_{lg} and θ_{ld} , are presented in panels (b) and (c) of Fig. 6.5. In panel (b), we observe that θ_{lg} *only* affects the advancing angle but *not* the receding angle. This is because θ_{lg} controls the depinning angle of the lubricant-gas interface

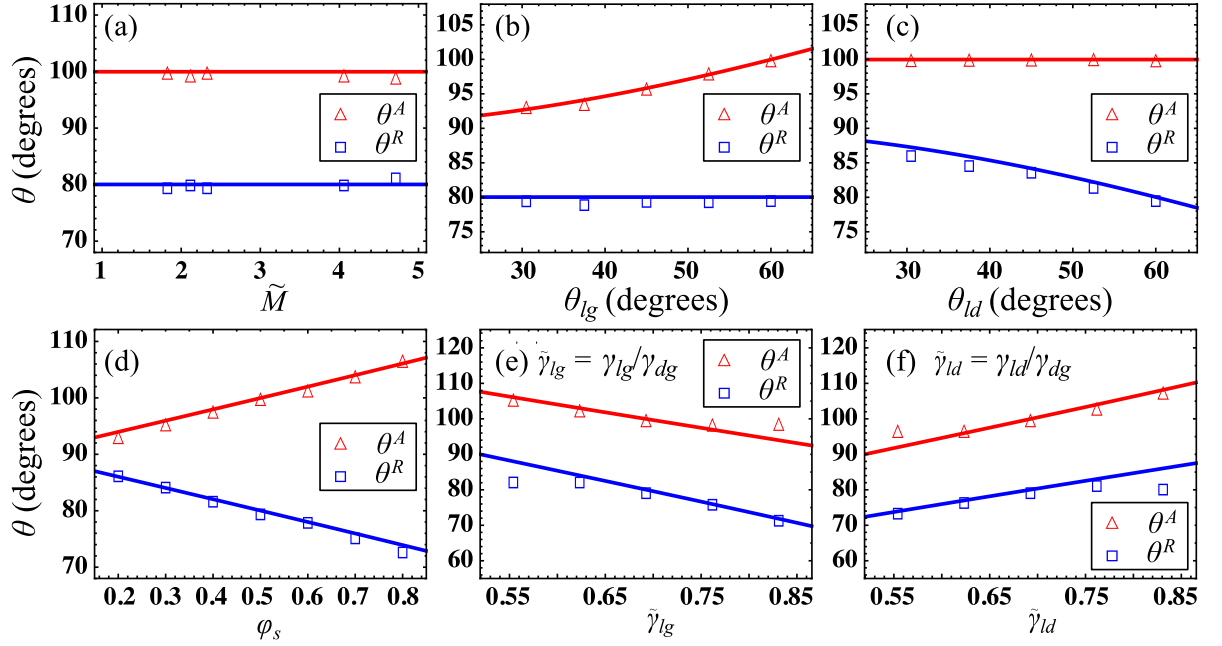


Figure 6.5: Advancing and receding contact angles upon variations in (a) the meniscus size, (b) the lubricant-gas wetting angle, (c) the lubricant-droplet wetting angle, (d) the solid fraction, and the ratios of (e) lubricant-gas and (f) lubricant-droplet surface tensions with the droplet-gas surface tension. In all panels, the red and blue lines are theoretical predictions for θ^A and θ^R given in Eqs. (6.15) and (6.16) respectively. The default values of the parameters are $\theta_{lg} = 60^\circ$; $\theta_{ld} = 60^\circ$; $\varphi_s = 0.5$; and $\gamma_{lg}/\gamma_{dg} = \gamma_{ld}/\gamma_{dg} = 0.69$.

when the droplet is advancing. When the droplet is receding, the lubricant-gas interface moves by bridging the neighbouring post, which is independent of θ_{lg} . Similarly, the bridging mechanism occurs for the lubricant-droplet interface during the advancing motion. As such, θ_{ld} does not affect the advancing angle, as shown in panel (c). In contrast, during the receding process, the lubricant-droplet interface moves by depinning from the post. Hence, the receding angle is affected by θ_{ld} .

The influence of the solid fraction φ_s is shown in panel (d) of Fig. 6.5. It is intuitive to foresee that $\Delta\theta$ increases with φ_s . More specifically, this is because θ^A increases while θ^R decreases with φ_s . This finding is aligned with the experimental results in Ref. [57]. In their work, although θ^A and θ^R were not measured directly, they showed that the pinning force that acts on a droplet on LIS can be reduced by employing surfaces with smaller φ_s [57].

Next, the effect of the lubricant interfacial tensions is demonstrated in Fig. 6.5(e) and (f). Interestingly, increasing γ_{lg} decreases both the advancing and the receding angles, while for γ_{ld} , the effect is reversed. This is due to the fact that increasing γ_{lg} generally makes a droplet on LIS to be more *hydrophilic*-like, while increasing γ_{ld} makes it more *hydrophobic*-like, and

thus the change of the contact angles follow accordingly [64, 122].

Finally, we have argued in Eq. (6.13) that the pinning force of a droplet on LIS does not depend on the droplet-gas interfacial tension γ_{dg} . Indeed, while the magnitudes of the advancing and receding angles are influenced by γ_{dg} , see Fig. 6.6(a), the pinning force per unit length is constant regardless of γ_{dg} , as shown in Fig. 6.6(b).

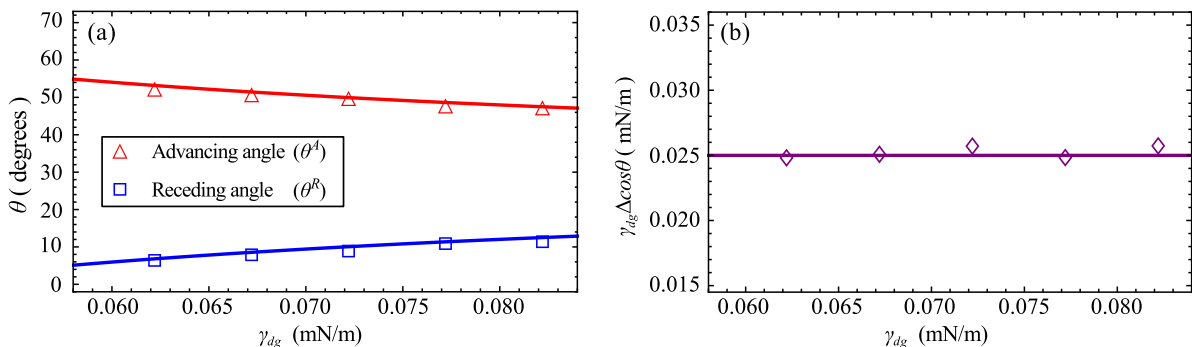


Figure 6.6: (a) The effect of γ_{dg} on θ^A and θ^R . The red and blue lines are the theoretical predictions for θ^A and θ^R as given in Eqs. (6.15) and (6.16) respectively. (b) The pinning force per unit length for a droplet on LIS is independent of γ_{dg} .

By studying each independent variable systematically, we have therefore demonstrated that Eqs. (6.15) and (6.16) are an excellent model to describe the advancing and receding angles, as well as the contact angle hysteresis. All simulation results are in excellent agreement with this model.

6.3 The Relationship Between Contact Angle Hysteresis, Sliding Angle and Pinning Force

It is common practice to measure the sliding angle α to determine the CAH. The droplet starts to slide when the external body force is larger than the pinning force that holds the droplet on the surface. The sliding angle α is related to the external body force via a simple relation

$$F_{ext} = \rho V_{drop} g \sin \alpha. \quad (6.17)$$

Here, ρ and V_{drop} are the density and volume of the droplet, while g is the gravitational acceleration.

To obtain the total pinning force, we need to integrate the pinning force per unit length over the base perimeter of the droplet contact area with the solid. Consider the geometry

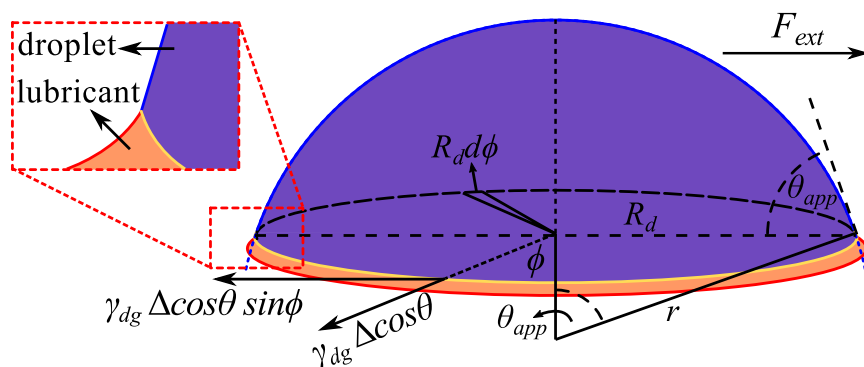


Figure 6.7: A sketch for the derivation of the pinning force of a droplet on LIS.

illustrated in Fig. 6.7, where again we focus on the vanishing meniscus limit. The pinning force per unit length is given by $\gamma_{dg}\Delta \cos \theta$; however, to balance the external force, we only need the vector component in the opposite direction of F_{ext} . Denoting ϕ as the azimuthal angle around the droplet, the vector component corresponds to $\gamma_{dg}\Delta \cos \theta \sin \phi$. Assuming that the droplet base is circular, the total pinning force is then

$$F_{pin} = \int_0^{\pi} \gamma_{dg}\Delta \cos \theta \sin \phi R_d d\phi = 2R_d\gamma_{dg}\Delta \cos \theta, \quad (6.18)$$

where R_d is the droplet base radius. When V_{drop} is known, R_d is linked to the droplet apparent contact angle θ_{app} via

$$R_d = \left(\frac{(12/\pi)V_{drop}}{8 - 9 \cos \theta_{app} + \cos(3\theta_{app})} \right)^{1/3} \sin \theta_{app}, \quad (6.19)$$

and the pinning force can be rewritten as

$$F_{pin} = \sqrt[3]{ \frac{(12/\pi)V_{drop}(2 \sin \theta_{app} \gamma_{dg}\Delta \cos \theta)^3}{8 - 9 \cos \theta_{app} + \cos(3\theta_{app})} }. \quad (6.20)$$

We can now balance the external body force Eq. (6.17) with the pinning force Eq. (6.18) to obtain the theoretical prediction of the sliding angle α , which is given by

$$\alpha = \sin^{-1} \left(\frac{2\gamma_{dg} R_d \Delta \cos \theta}{\rho V_{drop} g} \right). \quad (6.21)$$

Using Eq. (6.21), we can compare our theoretical prediction against the available experimental results. For this purpose, we use the experimental data reported in Ref. [57] for a water droplet on BMIm (an ionic liquid) infused surface. The comparisons are given in Table 6.1. The predicted sliding angles are consistent with the experimental values α_e .

Table 6.1: Comparisons between the experimental data from Ref. [57] and the theoretical predictions using Eq. (6.21) for the sliding angles of droplets on LIS.

φ_s	$\Delta\theta$ ($^\circ$)	α ($^\circ$)	α_e ($^\circ$)	$ \alpha - \alpha_e $ ($^\circ$)
0.25	8	28	30	2
0.33	11	37	45	8
0.44	14	53	60	7

In Table 6.1 we have also used our theory to calculate $\Delta\theta$ for each of φ_s provided in Ref. [57]. We find that, on LIS, a relatively low $\Delta\theta$ can still lead to a significant critical sliding angle α . This is different compared to superhydrophobic surfaces where α usually has the same magnitude as $\Delta\theta$. It also suggests that we should be cautious when using $\Delta\theta$ to characterise the mobility (and more generally, liquid repellency) of a liquid droplet on LIS.

There are two possibilities why a droplet on LIS may suffer from a large pinning force. First, the apparent contact angle θ_{app} is relatively low such that the droplet base perimeter is large, in direct contrast to the large θ_{app} and small base perimeter of drops on classical superhydrophobic surfaces. This large droplet base perimeter can potentially magnify the pinning force, since $F_{pin} \propto R_d$. Second, the pinning force is proportional to $\Delta \cos \theta$. Even for the same value of $\Delta\theta$, $\Delta \cos \theta$ is greater when $\theta_{app} \approx 90^\circ$ than when $\theta_{app} \approx 180^\circ$ or $\theta_{app} \approx 0^\circ$. Therefore, droplets on LIS are prone to large pinning forces when $\Delta\theta$ is large since most LIS systems reported in the literature have $\theta_{app} \approx 90^\circ$.

It is useful to express the pinning force in a non-dimensionalised form, given by

$$\tilde{F}_{pin} = \frac{F_{pin}}{\gamma_{dg} \sqrt[3]{V_{drop}}}, \quad (6.22)$$

$$\tilde{F}_{pin} \simeq \sqrt[3]{\frac{(12/\pi)(2 \sin^2 \theta_{app} \Delta\theta)^3}{8 - 9 \cos \theta_{app} + \cos(3\theta_{app})}} \quad (6.23)$$

for small $\Delta\theta$. This non-dimensionalised form of the pinning force depends only on $\Delta\theta$ and θ_{app} , which respectively represent the CAH and the shape of the droplet.

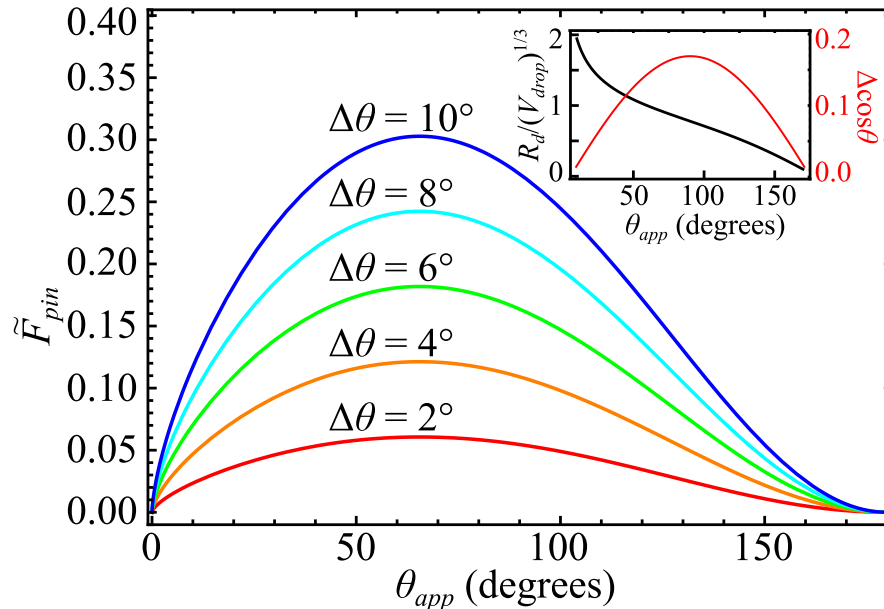


Figure 6.8: Visualisation of the effects of CAH and the droplet shape on the pinning force. The inset shows the non-dimensionalised droplet base radius $R_d/\sqrt[3]{V_{drop}}$ and $\Delta \cos \theta$ against θ_{app} .

The effects of $\Delta\theta$ and θ_{app} on the pinning force are visualised in Fig. 6.8. Interestingly, we find that the pinning force reaches its maximum at $\theta_{app} = 65.5^\circ$, regardless of $\Delta\theta$. Therefore, it is advisable to avoid the droplet-lubricant combinations which result in $\theta_{app} \approx 65.5^\circ$. The $\Delta \cos \theta$ itself reaches its maximum at $\theta_{app} = 90^\circ$ for any given value of $\Delta\theta$, as shown as the red plot in the inset of Fig. 6.8. This is an indication that $\Delta \cos \theta$ is not the only factor that controls the pinning force. The shift in the maximum of \tilde{F}_{pin} to the lower θ_{app} is due to the contribution from the droplet base perimeter. As shown in the inset (black plot), the non-dimensionalised droplet base radius $R_d/(V_{drop})^{1/3}$ is larger for smaller θ_{app} .

Fig. 6.8 also rationalises why pinning force is small for superhydrophobic surfaces. This is because both $\Delta \cos \theta$ and $R_d/(V_{drop})^{1/3}$ go to zero as $\theta \rightarrow 180^\circ$.

6.4 Discussion

In this work, we have considered CAH and pinning force of a droplet on LIS. We have derived the expressions for the advancing and receding angles as well as the pinning force using a force balance argument, including how they depend on the liquid interfacial tensions, the lubricant

wetting angles, and the solid fraction. Each dependency was systematically tested and verified using numerical simulations based on a diffuse interface approach using the phase field energy minimisation method. We also found that the pinning force does not depend on the droplet-gas interfacial tension, which distinguishes LIS from the other liquid repellent surfaces.

We have also derived an analytical expression for the critical droplet sliding angle, and the predictions from our theory are consistent with experimental data reported by Smith *et al* [57]. Furthermore, using this theory, we assess why liquid droplets on LIS suffer from larger pinning forces compared to superhydrophobic surfaces, even for the same $\Delta\theta$. We conclude this is due to two factors: both the droplet base perimeter and the magnitude of $\Delta \cos \theta$ are typically larger in LIS due to the lower (apparent) contact angle.

This study helps us to carefully design LIS by providing insights into how each relevant parameter influences the pinning force. Although the example shown here is for the square posts, similar derivations of the pinning force, as well as the advancing and the receding angles, can also be done for different surface geometries by following the same approach. Interestingly, the derivations rely on the depinning mechanism of each lubricant interface, which is just a binary fluid case. This shows an example where the complexity of ternary fluids systems can be broken down into their constituting binary fluids problems. It would be therefore interesting for future research to test our theory for more complex geometries. Furthermore, we hope our theory will motivate systematic experimental verifications, harnessing recent advances in surface fabrication techniques for LIS.

CHAPTER 7

Concluding Remarks

7.1 Conclusions

The purpose of this PhD project is to study the behaviour of a liquid droplet on a liquid infused surface (LIS) using computer simulations. To my knowledge, this thesis is the first to exploit lattice Boltzmann and phase field energy minimisation methods for studying LIS systems.

In Chapter 3, we showed that our lattice Boltzmann simulation results are in agreement with theoretical prediction in Ref. [67] for the equilibrium droplet shapes and with experimental results in Ref. [69] on how the droplet velocity depends on the droplet and lubricant viscosity ratio. These benchmarks and validations are important steps to ensure the reliability of the simulation methods.

In Chapter 4, we demonstrated how the lubricant wetting angles may influence droplet mobility via two different mechanisms. First, the wetting angles modulate the strength of contact line pinning which impedes droplet motion. Second, the wetting angles affect the shape of the lubricant ridge, which, in turn, changes the rate of the viscous dissipation during droplet motion. Interestingly, the two mechanisms are prominent in two separate regimes of the apparent contact angle. The former mechanism dominates at high apparent contact angle regime, while the latter dominates at low apparent contact angle regime. This finding complements the results of previous studies which found that the main dissipation channel is at the lubricant ridge [57,69], by highlighting the importance of the meniscus shape.

Another interesting topic we studied was the spontaneous motion of a droplet when placed on a LIS with textural gradient, as discussed in Chapter 5. Curiously, depending on the

droplet-lubricant combination, the droplet can either move to the denser or the sparser solid area. This phenomenon has never been reported elsewhere in the literature. We derived the driving force responsible for this bidirectional motion and verified it using lattice Boltzmann simulations and experiments (carried out by colleagues at Northumbria University). We then demonstrated the possibility of utilising this phenomenon for droplet classification based on its interfacial properties and size.

In Chapter 6, we analysed contact angle hysteresis and the pinning force that acts on a droplet on a LIS. We derived the equation for contact angle hysteresis and pinning force from an argument based on force balance. The theory was then validated using computer simulations based on phase field energy minimisation. Our calculation for the sliding angles was also compared against experimental results in Ref. [57], and it is fully consistent with experimental data. Two important observations can be drawn from our theory: (1) the contact line pinning does not depend on the droplet-gas surface tension as such interface does not directly interact with the solid; (2) the critical sliding angle on LIS can be significant even when the contact angle hysteresis is small. These two properties are different compared to the more commonly studied cases such as superhydrophobic surfaces.

7.2 Further Development of the Simulation Methods

In this section I will highlight some method development works that can be done to complement this PhD project.

As explained in Chapter 1, a droplet on LIS can either have an interface with the gas or be encapsulated by the lubricant. Lubricant cloaking happens when the droplet-gas surface tension is larger than the combined sum of droplet-lubricant and lubricant-gas surface tensions. At the current stage, our simulation tools are unable to capture this specific wetting state for two reasons. First, in our free energy model, the droplet encapsulation case requires one of the simulation parameters that control the energy penalty to be negative. This causes the simulation to become unstable. To solve this problem, a different free energy model that can accommodate lubricant encapsulation needs to be implemented. Additionally, the lubricant disjoining pressure must be considered when the droplet is encapsulated. Second, we use the diffuse interface approach where the interface between the two phases can be ~ 5 lattices wide. For the lubricant encapsulation case, it will require at least 10 lattice points to simulate the

compound droplet-lubricant-gas interfaces. Therefore, it will be computationally demanding to simulate the whole system. A possible solution to this problem is to implement adaptive mesh refinement techniques which can allocate more computational power to the more complex region of the simulation system [123], such as at the interface between fluids.

Another important improvement to our simulation tools is to combine the lattice Boltzmann and the phase field energy minimisation methods. The lattice Boltzmann method is powerful for studying the dynamics of fluid systems. However, this method is relatively costly in terms of computational power. When the dynamics of the system are not the main interest, the computational power is wasted to equilibrate the system by solving the hydrodynamic equations. On the other hand, the phase field energy minimisation method is efficient for finding minimum energy configurations. Therefore, it makes sense to build a hybrid simulation tool based on the two methods. In that approach, the phase field energy minimisation method will be used to achieve the thermodynamic equilibrium while the lattice Boltzmann method will be used to simulate the droplet motion.

7.3 Open Questions and Project Outlook

Based on the outcomes of this PhD project, I will now discuss possible directions for future works.

7.3.1 Lubricant Depletion

A major common issue in the design of LIS is their failure due to lubricant depletion which can be caused by numerous factors. For example, when the lubricant is encapsulating the droplet, the lubricant is reduced as the droplet is shedding from the surface [57]. Also, when a volatile lubricant is incorporated, the lubricant can deplete due to evaporation [110]. Lubricant can also deplete due to shearing motion when LIS are subject to a continuous flow [124].

There are two strategies to counter this problem. First, by designing LIS that have a small rate of lubricant depletion. This can be done by optimising the type of surface texturing, the chemical surface treatment, and the type of lubricant used. Second, by designing a lubricant refilling mechanism that can restore the liquid repellency of LIS. An example of this strategy is shown in Fig. 7.1, where lubricant refilling is achieved by injecting a mixture of water and lubricant in a channel flow [125].

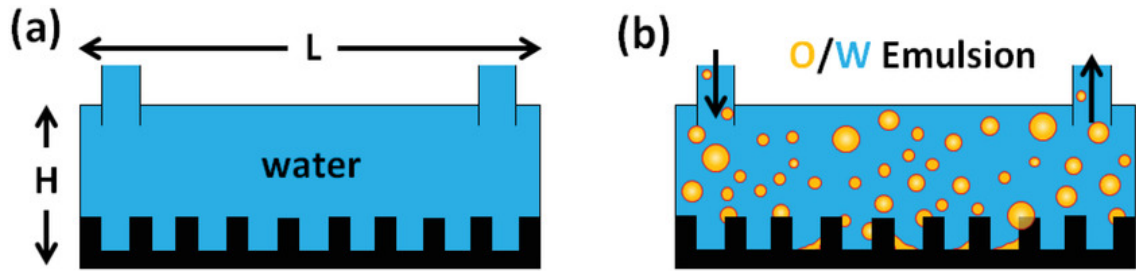


Figure 7.1: Lubricant refilling mechanism. (a) Textured surface without infusing lubricant. (b) Lubricant replenishment from a mixture of water and lubricant.

7.3.2 Lubricant Dynamics

Many studies have been carried out to investigate droplet dynamics on LIS. However, the dynamics of the lubricant itself have received less attention. A better understanding of lubricant dynamics is particularly important because the major dissipation channel is at the lubricant ridge.

A possible starting point for investigating the lubricant dynamics can be found in this thesis. In Chapter 4, we discuss the rotational motion of a droplet on LIS. We found that the data points for the percentage of rolling against the apparent contact angle, for various lubricant wetting angles and Bond numbers, collapse into a single curve as shown in Fig. 4.11. However, the lubricant flow dynamics, both at the wetting ridge and underneath the droplet, as the droplet moves across the surface is still unknown. To study these two aspects, our simulation box needs to be scaled up so that the lubricant motion can be quantified accurately.

The size of lubricant meniscus also influences the contact angle hysteresis, as highlighted by Semprebon *et.al.* In their prediction, there is a minimum in the contact angle hysteresis for a certain value of meniscus size compared to the droplet size (see Fig. 7.2(a)) [67]. However, the explanation for this effect is still unclear. Understanding this effect could lead to an optimal lubricant amount to be incorporated to minimise contact angle hysteresis.

Another interesting avenue for investigation is lubricant reorganisation when the droplet is in motion. In our simulation, we observe that the height of the advancing and receding menisci are different. Interestingly, we found cases where the advancing meniscus is lower than the receding one (Fig. 7.2(b)) and where the opposite is observed (Fig. 7.2(c)). This phenomenon is currently being investigated in collaboration with the experimental group of Prof. Doris Vollmer at the Max Planck Institute for Polymer Research in Mainz.

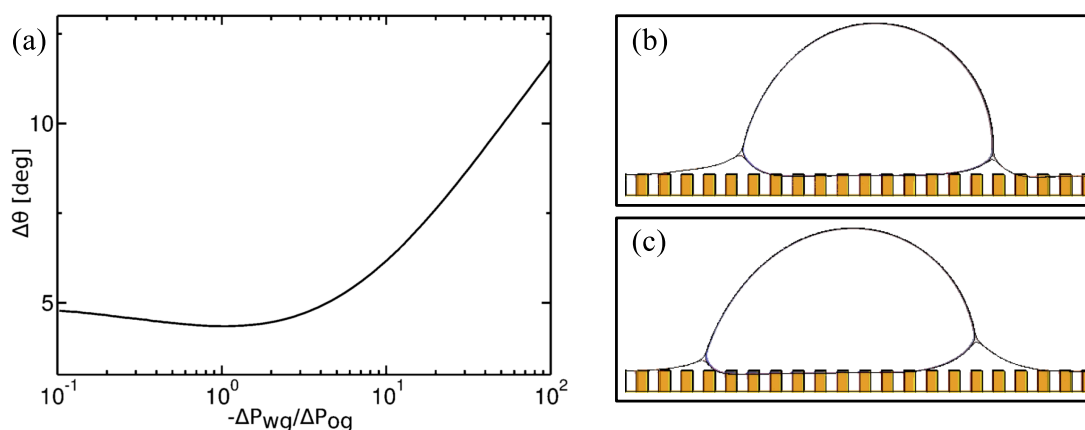


Figure 7.2: (a) The effect of meniscus size on contact angle hysteresis [67]. Here, the size of the meniscus is expressed as the Laplace's pressure ratio of the water-gas to the lubricant-gas interfaces. (b-c) The comparison of the morphology of the moving droplet when (b) the lubricant-gas wetting angle is larger than the lubricant-droplet wetting angle, and (c) the opposite case.

7.3.3 Applications of Liquid Infused Surfaces

Microfluidic devices

The potential application of LIS is not just limited to liquid repellent surfaces. For instance, in Chapter 5, we have demonstrated the possibility of utilising the droplet bidirectional motion for microfluidic applications. Another related topic that is also worth investigating is to test the droplet bidirectional motion on a chemical gradient. The chemical gradient itself is essentially similar to the setup used in our 2D simulations in Chapter 5. Therefore, it would be interesting to test these concepts experimentally.

One advantage of using a chemical gradient is that the sample fabrication is relatively simpler compared to a topographical gradient. For instance, Chaudhury *et al.* has demonstrated the use of chemical vapour deposition to create wetting gradient [96]. Another possibility is to deposit photocatalytic nanoparticles on a flat substrate and cover it with silane molecules. The nanoparticles will create surface roughness to allow lubricant imbibition, while the silane molecules will alter the wettability of the nanoparticles. Upon light exposure, photocatalytic reaction will decompose silane molecules [126]. Thus, the wetting gradient can be rendered by simply exposing the substrate to gradient light exposure.

Fog harvesting surfaces

LIS can also be applied for fog harvesting devices [127, 128]. In a recent development, LIS is designed to have multiscale surface texturing for water harvesting purpose. Fig. 7.3(a) shows the schematic of grooves type surface texturing where another lower scale surface roughness is introduced on top of it. This design can speed up the condensed droplet removal, allowing more area to be ready for more nucleation, as shown in Fig. 7.3(b) [127]. However, there are still open questions on the optimum design and on how the surface texturing influences the rate of condensation.

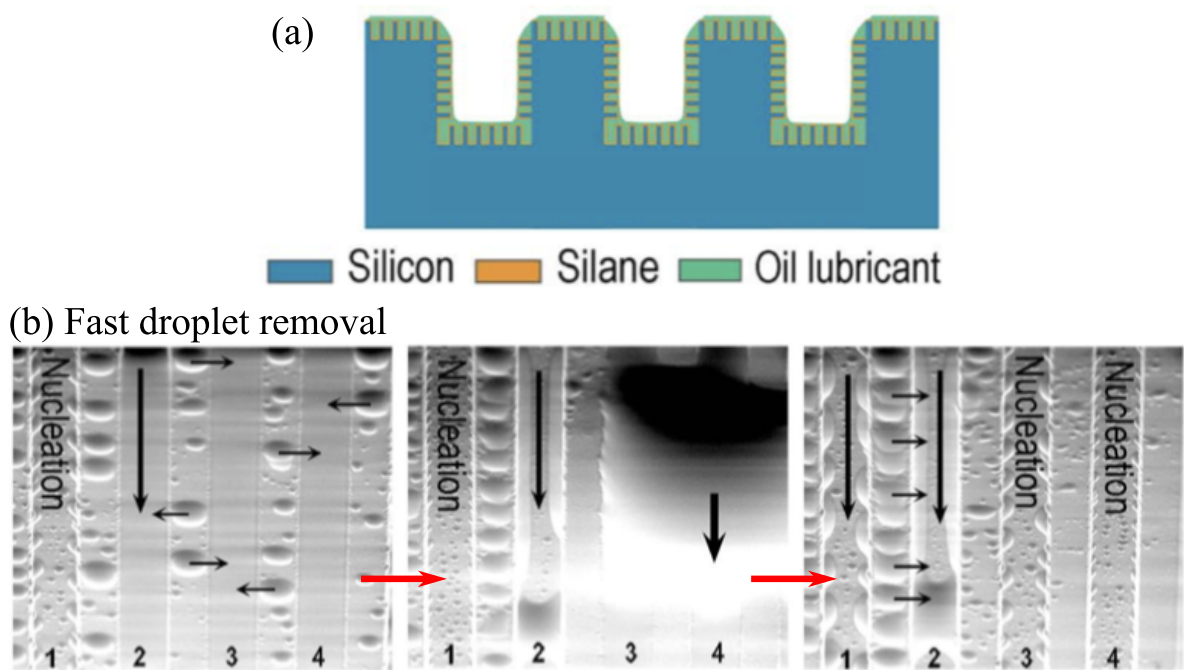


Figure 7.3: Application of LIS as a fog harvesting surface [127]. (a) Schematic of the grooves type LIS with multiscale surface texturing design. It reveals that the lower scale roughness is imbued with oil lubricant, while the higher scale roughness remains unfilled. (b) The fabricated LIS demonstrates fast droplet removal.

There are rich multi-droplets interactions on the surface during fog collection. The droplets may repel, attract, or coalesce [128]. While these interactions have been studied for binary fluid systems, the presence of lubricant on LIS may result in different outcomes. Through the wetting ridge, droplets can experience long-range interactions. There is also an open question on how the nucleation process is influenced by the presence and amount of lubricant.

Oil-water separation membranes

Another application of LIS that is undersold is for oil-water separation [13,14]. This application is useful in petroleum industries where both oil and water are co-produced from the well. The device works by infusing water to the porous membrane in such a way that the membrane only permeates the water while retaining the oil (see Fig. 7.4). For this application, the membrane is desired to have a high intrusion pressure, which is a measure of the amount of oil before the separation fail. The membrane is also desired to be able to pass water with high flow rate. These two aspects have the opposite dependency on the pore size of the membrane. Thus, finding the value of optimum pore size is needed for efficient oil-water separation. Another aspect that needs to be considered is the ability of the membrane to prevent and to heal from oil fouling. This ability depends on the interfacial properties of the membrane such as the wettability and surface texturing.

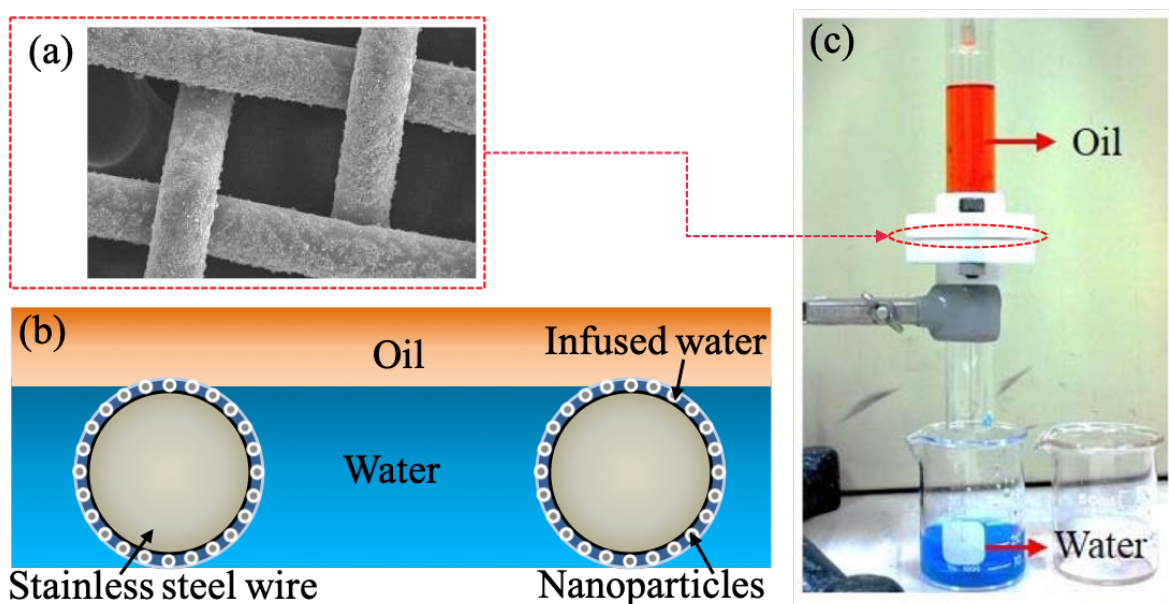


Figure 7.4: Application of LIS as an oil-water separation membrane [13]. (a) The membrane is fabricated from stainless steel mesh coated with nanoparticles. (b) The roughness from nanoparticles allows water infusion and creates water film between the stainless steel wires, which prevent oil from penetrating the membrane. (c) The resulting oil-water separation where water is permeated through the membrane while oil is suspended.

7.4 Epilogue

In this PhD work, I have developed computational tools suitable for studying ternary fluids system. While I have focussed on LIS, the tools are general and can be exploited to study a wide range of problems in wetting phenomena and multiphase flows, including droplet generation in microfluidic devices, enhanced oil recovery, capillary imbibition, fluid phase separation and mixing, and droplet collision dynamics [129–131].

Finally, I hope that this thesis can convince a broad range of audience about the excitement of research in wetting phenomena, especially on LIS.

REFERENCES

- [1] P.-G. de Gennes, F. Brochard-Wyart, and D. Quere. *Capillarity and Wetting Phenomena: Drops, Bubbles, Pearls, and Waves*. Springer-Verlag, New York, (2004).
- [2] P. P. Jadhunandan and N. R. Morrow, “Effect of wettability on waterflood recovery for crude oil/brine/rock systems”, *SPE Reserv. Eng.* **10**, 40–46 (1995).
- [3] G. Hirasaki, C. A. Miller, and M. Puerto, “Recent Advances in Surfactant EOR”, *SPE J.* **16**, 889–907 (2011).
- [4] P. J. Holloway, “Surface factors affecting the wetting of leaves”, *Pestic. Sci.* **1**, 156–163 (1970).
- [5] J. D. Smith, R. Dhiman, A. T. Paxson, C. J. Love, B. Solomon, and K. K. Varanasi. “Self-lubricating surfaces for food packing and food processing equipment”, (2015). US Patent:US8940361B2.
- [6] G. Whyman, E. Bormashenko, and T. Stein, “The rigorous derivation of Young, Cassie–Baxter and Wenzel equations and the analysis of the contact angle hysteresis phenomenon”, *Chem. Phys. Lett.* **450**, 355 – 359 (2008).
- [7] T. Young, “An Essay on the Cohesion of Fluids”, *Philos. Trans. R. Soc. London* **95**, 65 (1805).
- [8] Y. Yuan and T. Lee. “Contact Angle and Wetting Properties”. In *Surface Science Techniques*, G. Bracco and B. Holst, editors, chapter 1, 1–34. Springer-Verlag, Heidelberg (2013).
- [9] A. Amirfazli and A. Neumann, “Status of the three-phase line tension: a review”, *Adv. Colloid Interface Sci.* **110**, 121 – 141 (2004).
- [10] J. F. Lea, H. V. Nickens, and M. R. Wells. *Gas Well Deliquification*. Gulf Professional Publishing, Burlington, (2008).
- [11] J. J. Videler, D. Haydar, R. Snoek, H.-J. T. Hoving, and B. G. Szabo, “Lubricating the swordfish head”, *J. Exp. Biol.* **219**, 1953–1956 (2016).
- [12] R. Mercadé-Prieto and S. Bakalis, “Methodological study on the removal of solid oil and fat stains from cotton fabrics using abrasion”, *Text. Res. J* **84**, 52–65 (2014).
- [13] M. A. Gondal, M. S. Sadullah, M. A. Dastageer, G. H. McKinley, D. Panchanathan, and K. K. Varanasi, “Study of Factors Governing Oil–Water Separation Process Using TiO₂ Films Prepared by Spray Deposition of Nanoparticle Dispersions”, *ACS Appl. Mater. Interfaces* **6**, 13422–13429 (2014).

- [14] M. A. Gondal, M. S. Sadullah, T. F. Qahtan, M. A. Dastageer, U. Baig, and G. H. McKinley, “Fabrication and Wettability Study of WO₃ Coated Photocatalytic Membrane for Oil-Water Separation: A Comparative Study with ZnO Coated Membrane”, *Sci. Rep.* **7**, 1686 (2017).
- [15] L. Girifalco and R. Good, “A theory for the estimation of surface and interfacial energies. I. Derivation and application to interfacial tension”, *J. Phys. Chem.* **61**, 904–909 (1957).
- [16] D. Quéré, “Wetting and Roughness”, *Annu. Rev. Mater. Res.* **38**, 71–99 (2008).
- [17] C. Semprebon, P. Forsberg, C. Priest, and M. Brinkmann, “Pinning and wicking in regular pillar arrays.”, *Soft Matter* **10**, 5739–48 (2014).
- [18] A. Marmur, “Contact-angle hysteresis on heterogeneous smooth surfaces: theoretical comparison of the captive bubble and drop methods”, *Colloids Surf. A Physicochem. Eng. Asp.* **136**, 209 – 215 (1998).
- [19] C. Huh and S. Mason, “Effects of surface roughness on wetting (theoretical)”, *J. Colloid Interface Sci.* **60**, 11 – 38 (1977).
- [20] J. Long, M. Hyder, R. Huang, and P. Chen, “Thermodynamic modeling of contact angles on rough, heterogeneous surfaces”, *Adv. Colloid Interface Sci.* **118**, 173 – 190 (2005).
- [21] H. B. Eral, D. ’t Mannetje, and J. M. Oh, “Contact angle hysteresis: a review of fundamentals and applications”, *Colloid Polym. Sci.* **291**, 247–260 (2013).
- [22] H. Y. Erbil, “The debate on the dependence of apparent contact angles on drop contact area or three-phase contact line: A review”, *Surf. Sci. Rep.* **69**, 325 – 365 (2014).
- [23] F. Wang and H. Wu, “Molecular origin of contact line stick-slip motion during droplet evaporation”, *Sci. Rep.* **5**, 17521 (2015).
- [24] S. Ramos and A. Tanguy, “Pinning-depinning of the contact line on nanorough surfaces”, *Eur. Phys. J. E* **19**, 433–440 (2006).
- [25] W. Xu and C.-H. Choi, “From Sticky to Slippery Droplets: Dynamics of Contact Line Depinning on Superhydrophobic Surfaces”, *Phys. Rev. Lett.* **109**, 024504 (2012).
- [26] R. Wenzel, “Resistance of Solid Surfaces to Wetting by Water”, *Ind. Eng. Chem.* **28**, 988 (1936).
- [27] L. Feng, Y. Zhang, J. Xi, Y. Zhu, N. Wang, F. Xia, and L. Jiang, “Petal Effect: A Superhydrophobic State with High Adhesive Force”, *Langmuir* **24**, 4114–4119 (2008).
- [28] A. Cassie and S. Baxter, “Wettability of Porous Surfaces”, *Trans. Faraday Soc.* **40**, 546 (1944).
- [29] A. Marmur, “The Lotus Effect: Superhydrophobicity and Metastability”, *Langmuir* **20**, 3517–3519 (2004).
- [30] Y. Zheng, H. Bai, Z. Huang, X. Tian, F.-Q. Nie, Y. Zhao, J. Zhai, and L. Jiang, “Directional water collection on wetted spider silk”, *Nature* **463**, 640–643 (2010).
- [31] J. Ju, H. Bai, Y. Zheng, T. Zhao, R. Fang, and L. Jiang, “A multi-structural and multi-functional integrated fog collection system in cactus”, *Nat. Comm.* **3**, 1247 (2012).

- [32] J. Li, Q. H. Qin, A. Shah, R. H. A. Ras, X. Tian, and V. Jokinen, “Oil droplet self-transportation on oleophobic surfaces”, *Sci. Adv.* **2** (2016).
- [33] O. Bliznyuk, J. R. Seddon, V. Veligura, E. S. Kooij, H. J. W. Zandvliet, and B. Poelsema, “Directional Liquid Spreading over Chemically Defined Radial Wettability Gradients”, *ACS Appl. Mater. Interfaces* **4**, 4141–4148 (2012).
- [34] X. Tian, Y. Chen, Y. Zheng, H. Bai, and L. Jiang, “Controlling Water Capture of Bioinspired Fibers with Hump Structures”, *Adv. Mater.* **23**, 5486–5491 (2011).
- [35] J.-T. Yang, Z.-H. Yang, C.-Y. Chen, and D.-J. Yao, “Conversion of Surface Energy and Manipulation of a Single Droplet across Micropatterned Surfaces”, *Langmuir* **24**, 9889–9897 (2008).
- [36] W. Barthlott and C. Neinhuis, “Purity of the sacred lotus, or escape from contamination in biological surfaces”, *Planta* **202**, 1–8 (1997).
- [37] U. Mehmood, F. A. Al-Sulaiman, B. Yilbas, B. Salhi, S. Ahmed, and M. K. Hossain, “Superhydrophobic surfaces with antireflection properties for solar applications: A critical review”, *Sol. Energy Mater. Sol. Cells* **157**, 604 – 623 (2016).
- [38] J. Ou, W. Hu, M. Xue, F. Wang, and W. Li, “Superhydrophobic Surfaces on Light Alloy Substrates Fabricated by a Versatile Process and Their Corrosion Protection”, *ACS Appl. Mater. Interfaces* **5**, 3101–3107 (2013).
- [39] N. J. Shirtcliffe, G. McHale, M. I. Newton, and Y. Zhang, “Superhydrophobic Copper Tubes with Possible Flow Enhancement and Drag Reduction”, *ACS Appl. Mater. Interfaces* **1**, 1316–1323 (2009).
- [40] B. Wu, M. Zhou, J. Li, X. Ye, G. Li, and L. Cai, “Superhydrophobic surfaces fabricated by microstructuring of stainless steel using a femtosecond laser”, *Appl. Surf. Sci.* **256**, 61 – 66 (2009).
- [41] M. Nosonovsky and B. Bhushan, “Patterned Nonadhesive Surfaces Superhydrophobicity and Wetting Regime Transitions”, *Langmuir* **24**, 1525–1533 (2008).
- [42] S. H. Kim, G. C. Lee, J. Y. Kang, K. Moriyama, H. S. Park, and M. H. Kim, “The role of surface energy in heterogeneous bubble growth on ideal surface”, *Int. J. Heat Mass Transf.* **108**, 1901 – 1909 (2017).
- [43] D. Quere, “Leidenfrost Dynamics”, *Annu. Rev. Fluid Mech.* **45**, 197–215 (2013).
- [44] M. Ma and R. M. Hill, “Superhydrophobic surfaces”, *Curr. Opin. Colloid Interface Sci.* **11**, 193–202 (2006).
- [45] X. Deng, L. Mammen, H.-J. Butt, and D. Vollmer, “Candle Soot as a Template for a Transparent Robust Superamphiphobic Coating”, *Science* **335**, 67–70 (2012).
- [46] Y. Si and Z. Guo, “Superhydrophobic nanocoatings: from materials to fabrications and to applications”, *Nanoscale* **7**, 5922–5946 (2015).
- [47] A. Tuteja, W. Choi, G. H. McKinley, R. E. Cohen, and M. F. Rubner, “Design Parameters for Superhydrophobicity and Superoleophobicity”, *MRS Bull.* **33**, 752–758 (2008).
- [48] T. Liu and C. Kim, “Turning a surface superrepellent even to completely wetting liquids”, *Science* **346**, 1800103 (2014).

- [49] X. Liu, H. Gu, M. Wang, X. Du, B. Gao, A. Elbaz, L. Sun, J. Liao, P. Xiao, , and Z. Gu, “3D Printing of Bioinspired Liquid Superrepellent Structures”, *Adv. Mater.* **30**, 1800103 (2018).
- [50] G. J. Puts, P. Crouse, and B. M. Ameduri, “Polytetrafluoroethylene: Synthesis and Characterization of the Original Extreme Polymer”, *Chem. Rev.* **119**, 1763–1805 (2019).
- [51] A. Bouillant, T. Mousterde, P. Bourriane, A. Lagarde, C. Clanet, and D. Quéré, “Leidenfrost wheels”, *Nat. Phys.* **14**, 1188–1192 (2018).
- [52] P. Agrawal, G. G. Wells, R. Ledesma-Aguilar, G. McHale, A. Buchoux, A. Stokes, and K. Sefiane, “Leidenfrost heat engine: Sustained rotation of levitating rotors on turbine-inspired substrates”, *Appl. Energy* **240**, 399 – 408 (2019).
- [53] D. Murakami, H. Jinnai, and A. Takahara, “Wetting Transition from the Cassie–Baxter State to the Wenzel State on Textured Polymer Surfaces”, *Langmuir* **30**, 2061–2067 (2014).
- [54] J. R. Panter, Y. Gizaw, and H. Kusumaatmaja, “Multifaceted design optimization for superomniphobic surfaces”, *Sci. Adv.* **5** (2019).
- [55] D. Quéré, “Non-sticking drops”, *Rep. Prog. Phys.* **68**, 2495 (2005).
- [56] G. Mistura and M. Pierno, “Drop mobility on chemically heterogeneous and lubricant-impregnated surfaces”, *Adv. Phys. X* **2**, 591–607 (2017).
- [57] J. D. Smith, R. Dhiman, S. Anand, E. Reza-Garduno, R. E. Cohen, G. H. McKinley, and K. K. Varanasi, “Droplet mobility on lubricant-impregnated surfaces”, *Soft Matter* **9**, 1772–1780 (2013).
- [58] T.-S. Wong, S. H. Kang, S. K. Y. Tang, E. J. Smythe, B. D. Hatton, A. Grinthal, and J. Aizenberg, “Bioinspired self-repairing slippery surfaces with pressure-stable omniphobicity.”, *Nature* **477**, 443–7 (2011).
- [59] H. F. Bohn and W. Federle, “Insect aquaplaning: *Nepenthes* pitcher plants capture prey with the peristome, a fully wetttable water-lubricated anisotropic surface”, *Proc. Natl. Acad. Sci. U.S.A.* **39**, 14138–14143 (2004).
- [60] A. Lafuma and D. Quéré, “Slippery pre-suffused surfaces”, *Europhys. Lett.* **96**, 56001 (2011).
- [61] Y. Lu, S. Sathasivam, J. Song, C. R. Crick, C. J. Carmalt, and I. P. Parkin, “Robust self-cleaning surfaces that function when exposed to either air or oil”, *Science* **347**, 1132–1135 (2015).
- [62] M. Ferrari, A. Benedetti, E. Santini, F. Ravera, L. Liggieri, E. Guzman, and F. Cirisano, “Biofouling control by superhydrophobic surfaces in shallow euphotic seawater”, *Colloids Surf. A* **480**, 369 – 375 (2015).
- [63] P. Kim, M. J. Kreder, J. Alvarenga, and J. Aizenberg, “Hierarchical or Not ? Effect of the Length Scale and Hierarchy of the Surface Roughness on Omniphobicity of Lubricant-Infused Substrates”, *Nano Lett.* **13**, 1793–1799 (2013).
- [64] F. Schellenberger, J. Xie, N. Encinas, A. Hardy, M. Klapper, P. Papadopoulos, H.-J. Butt, and D. Vollmer, “Direct observation of drops on slippery lubricant-infused surfaces”, *Soft Matter* **11**, 7617–7626 (2015).

- [65] D. Daniel, J. V. I. Timonen, R. Li, S. J. Velling, and J. Aizenberg, “Oleoplaning droplets on lubricated surfaces”, *Nat. Phys.* **13**, 1020 (2017).
- [66] M. J. Kreder, D. Daniel, A. Tetreault, Z. Cao, B. Lemaire, J. V. I. Timonen, and J. Aizenberg, “Film Dynamics and Lubricant Depletion by Droplets Moving on Lubricated Surfaces”, *Phys. Rev. X* **8**, 031053 (2018).
- [67] C. Semperebon, G. McHale, and H. Kusumaatmaja, “Apparent Contact Angle and Contact Angle Hysteresis on Liquid Infused Surfaces”, *Soft Matter* **13**, 101–110 (2017).
- [68] N. Moradi, F. Varnik, and I. Steinbach, “Roughness-gradient-induced spontaneous motion of droplets on hydrophobic surfaces: A lattice Boltzmann study”, *Europhys. Lett.* **89**, 26006 (2010).
- [69] A. Keiser, L. Keiser, C. Clanet, and D. Quéré, “Drop friction on liquid-infused materials”, *Soft Matter* **13**, 6981–6987 (2017).
- [70] J. Y. A. Dupuis, “Modeling droplets on superhydrophobic surfaces: equilibrium states and transitions”, *Langmuir* **21**, 2624 (2005).
- [71] J. Kim, “Phase field computations for ternary fluid flows”, *Comput. Methods Appl. Mech. Eng.* **196**, 4779–4788 (2007).
- [72] C. Semperebon, T. Krüger, and H. Kusumaatmaja, “Ternary free-energy lattice Boltzmann model with tunable surface tensions and contact angles”, *Phys. Rev. E* **93**, 033305 (2016).
- [73] H. Kusumaatmaja and J. M. Yeomans. “Lattice Boltzmann Simulations of Wetting and Drop Dynamics”. In *Simulating Complex Systems by Cellular Automata*, A. G. Hoekstra, J. Kroc, and P. M. A. Sloot, editors, chapter 11, 241–274. Springer-Verlag, Heidelberg (2010).
- [74] N. Wang, C. Semperebon, H. Liu, C. Zhang, and H. Kusumaatmaja, “Modelling double emulsion formation in planar flow-focusing microchannels”, *arXiv*, 1906.01034 (2019).
- [75] J. Cahn, “Critical-point wetting”, *J. Chem. Phys.* **66**, 3667 (1977).
- [76] P.-G. DeGennes, “Wetting: statics and dynamics”, *Rev. Mod. Phys.* **57**, 827 (1985).
- [77] T. Krüger, H. Kusumaatmaja, A. Kuzmin, O. Shardt, G. Silva, and E. M. Viggien. *The Lattice Boltzmann Method*. Springer International Publishing, (2017).
- [78] K. Connington and T. Lee, “Lattice Boltzmann simulations of forced wetting transitions of drops on superhydrophobic surfaces”, *J. Comp. Phys.* **250**, 601–615 (2013).
- [79] D. C. Liu and J. Nocedal, “On the limited memory BFGS method for large scale optimization”, *Math. Program.* **45**, 503–528 (1989).
- [80] H. Kusumaatmaja, “Surveying the free energy landscapes of continuum models: Application to soft matter systems”, *J. Chem. Phys.* **142**, 124112 (2015).
- [81] B. M. Mognetti, H. Kusumaatmaja, and J. M. Yeomans, “Drop dynamics on hydrophobic and superhydrophobic surfaces”, *Faraday Disc.* **146**, 153–165 (2010).

- [82] N. Moradi, F. Varnik, and I. Steinbach, “Roughness-gradient-induced spontaneous motion of droplets on hydrophobic surfaces: A lattice Boltzmann study”, *Europhys. Lett.* **89**, 26006 (2010).
- [83] D. Richard and D. Quéré, “Viscous drops rolling on a tilted non-wettable solid”, *Europhys. Lett.* **48**, 286 (1999).
- [84] L. Mahadevan and Y. Pomeau, “Rolling droplets”, *Phys. Fluids* **11**, 2449–2453 (1999).
- [85] S. R. Hodges, O. E. Jensen, and J. M. Rallison, “Sliding, slipping and rolling: the sedimentation of a viscous drop down a gently inclined plane”, *J. Fluid Mech.* **512**, 95–131 (2004).
- [86] S. P. Thampi, R. Adhikari, and R. Govindarajan, “Do liquid drops roll or slide on inclined surfaces?”, *Langmuir* **29**, 3339–3346 (2013).
- [87] N. Moradi, F. Varnik, and I. Steinbach, “Contact angle dependence of the velocity of sliding cylindrical drop on flat substrates”, *Europhys. Lett.* **95**, 44003 (2011).
- [88] S. Varagnolo, D. Ferraro, P. Fantinel, M. Pierno, G. Mistura, G. Amati, L. Biferale, and M. Sbragaglia, “Stick-Slip Sliding of Water Drops on Chemically Heterogeneous Surfaces”, *Phys. Rev. Lett.* **111**, 066101 (2013).
- [89] B. S. Yilbas, A. Al-Sharafi, H. Ali, and N. Al-Aqeeli, “Dynamics of a water droplet on a hydrophobic inclined surface: influence of droplet size and surface inclination angle on droplet rolling”, *RSC Adv.* **7**, 48806–48818 (2017).
- [90] S. K. Cho, H. Moon, and C.-J. Kim, “Creating, transporting, cutting, and merging liquid droplets by electrowetting-based actuation for digital microfluidic circuits”, *J. Microelectromech. Syst.* **12**, 70–80 (2003).
- [91] X.-M. Li, D. Reinhoudt, and M. Crego-Calama, “What do we need for a superhydrophobic surface? A review on the recent progress in the preparation of superhydrophobic surfaces”, *Chem. Soc. Rev.* **36**, 1350–1368 (2007).
- [92] G. R. Willmott, C. Neto, and S. C. Hendy, “Uptake of water droplets by non-wetting capillaries”, *Soft Matter* **7**, 2357–2363 (2011).
- [93] M. Damak and K. K. Varanasi, “Electrostatically driven fog collection using space charge injection”, *Sci. Adv.* **4**, eaao5323 (2018).
- [94] R. Labbé and C. Duprat, “Capturing aerosol droplets with fibers”, *Soft Matter* **15**, 6946–6951 (2019).
- [95] Q. Sun, D. Wang, Y. Li, J. Zhang, S. Ye, J. Cui, L. Chen, Z. Wang, H.-J. Butt, D. Vollmer, and X. Deng, “Surface charge printing for programmed droplet transport”, *Nat. Mater.* **18**, 936–941 (2019).
- [96] M. K. Chaudhury and G. M. Whitesides, “How to Make Water Run Uphill”, *Science* **256**, 1539–1541 (1992).
- [97] F. Varnik, P. Truman, B. Wu, P. Uhlmann, D. Raabe, and M. Stamm, “Wetting gradient induced separation of emulsions: A combined experimental and lattice Boltzmann computer simulation study”, *Phys. Fluids* **20**, 072104 (2008).

- [98] M. Reyssat, F. Pardo, and D. Quéré, “Drops onto gradients of texture”, *Europhys. Lett.* **87**, 36003 (2009).
- [99] R. W. Style, Y. Che, S. J. Park, B. M. Weon, J. H. Je, C. Hyland, G. K. German, M. P. Power, L. A. Wilen, J. S. Wettlaufer, and E. R. Dufresne, “Patterning droplets with durotaxis”, *Proc. Natl. Acad. Sci. U.S.A.* **110**, 12541–12544 (2013).
- [100] C. Zhang, B. Zhang, H. Ma, Z. Li, X. Xiao, Y. Zhang, X. Cui, C. Yu, M. Cao, and L. Jiang, “Bioinspired Pressure-Tolerant Asymmetric Slippery Surface for Continuous Self-Transport of Gas Bubbles in Aqueous Environment”, *ACS Nano* **12**, 2048–2055 (2018).
- [101] J. McCarthy, D. Vella, and A. A. Castrejón-Pita, “Dynamics of droplets on cones: self-propulsion due to curvature gradients”, *Soft Matter* **15**, 9997–10004 (2019).
- [102] G. Launay, M. S. Sadullah, G. McHale, R. Ledesma-Aguilar, H. Kusumaatmaja, and G. G. Wells, “Self-Propelled Droplet Transport on Shaped-Liquid Surfaces”, *arXiv*, 1908.01305 (2019).
- [103] R. S. Subramanian, N. Moumen, and J. B. McLaughlin, “Motion of a Drop on a Solid Surface Due to a Wettability Gradient”, *Langmuir* **21**, 11844–11849 (2005).
- [104] G. McHale, B. V. Orme, G. G. Wells, and R. Ledesma-Aguilar, “Apparent Contact Angles on Lubricant-Impregnated Surfaces/SLIPS: From Superhydrophobicity to Electrowetting”, *Langmuir* **35**, 4197–4204 (2019).
- [105] L. Wang and T. McCarthy, “Covalently Attached Liquids: Instant Omniphobic Surfaces with Unprecedented Repellency”, *Angew. Chem.* **128**, 252 (2015).
- [106] I. Sotiri, J. C. Overton, A. Waterhouse, and C. Howell, “Immobilized liquid layers: A new approach to anti-adhesion surfaces for medical applications”, *Exp. Biol. Med.* **241**, 909–918 (2016).
- [107] C. S. Ware, T. Smith-Palmer, S. Peppou-Chapman, L. R. Scarratt, E. M. Humphries, D. Balzer, and C. Neto, “Marine Antifouling Behavior of Lubricant-Infused Nanowrinkled Polymeric Surfaces”, *ACS Appl. Mater. Interfaces* **10**, 4173–4182 (2018).
- [108] P. S. Brown and B. Bhushan, “Liquid-impregnated porous polypropylene surfaces for liquid repellency”, *J. Colloid Interface Sci.* **487**, 437–443 (2017).
- [109] H. Geng and S. K. Cho, “Antifouling digital microfluidics using lubricant infused porous film”, *Lab Chip* **19**, 2275–2283 (2019).
- [110] Y. Galvan, K. R. Phillips, M. Haumann, P. Wasserscheid, R. Zarraga, and N. Vogel, “Ionic-Liquid-Infused Nanostructures as Repellent Surfaces”, *Langmuir* **34**, 6894–6902 (2018).
- [111] C. Howell, T. L. Vu, C. P. Johnson, X. Hou, O. Ahanotu, J. Alvarenga, D. C. Leslie, O. Uzun, A. Waterhouse, P. Kim, M. Super, M. Aizenberg, D. E. Ingber, and J. Aizenberg, “Stability of Surface-Immobilized Lubricant Interfaces under Flow”, *Chem. Mater.* **27**, 1792–1800 (2015).
- [112] Y. Liu, J. S. Wexler, C. Schönecker, and H. A. Stone, “Effect of viscosity ratio on the shear-driven failure of liquid-infused surfaces”, *Phys. Rev. Fluids* **1**, 074003 (2016).

- [113] S. Sett, X. Yan, G. Barac, L. W. Bolton, and N. Miljkovic, “Lubricant-Infused Surfaces for Low-Surface-Tension Fluids: Promise versus Reality”, *ACS Appl. Mater. Interfaces* **9**, 36400–36408 (2017).
- [114] S. Peppou-Chapman and C. Neto, “Mapping Depletion of Lubricant Films on Antibiofouling Wrinkled Slippery Surfaces”, *ACS Appl. Mater. Interfaces* **10**, 33669–33677 (2018).
- [115] M. J. Kreder, D. Daniel, A. Tetreault, Z. Cao, B. Lemaire, J. V. Timonen, and J. Aizenberg, “Film Dynamics and Lubricant Depletion by Droplets Moving on Lubricated Surfaces”, *Phys. Rev. X* **8**, 031053 (2018).
- [116] X. Lou, Y. Huang, X. Yang, H. Zhu, L. Heng, and F. Xia, “External Stimuli Responsive Liquid-Infused Surfaces Switching between Slippery and Nonslippery States: Fabrications and Applications”, *Adv. Funct. Mater.* **30**, 1901130 (2020).
- [117] Y. Wang, B. Qian, C. Lai, X. Wang, K. Ma, Y. Guo, X. Zhu, B. Fei, and J. H. Xin, “Flexible Slippery Surface to Manipulate Droplet Coalescence and Sliding, and Its Practicability in Wind-Resistant Water Collection”, *ACS Appl. Mater. Interfaces* **9**, 24428–24432 (2017).
- [118] M. S. Sadullah, G. Launay, J. Parle, R. Ledesma-Aguilar, Y. Gizaw, G. McHale, G. G. Wells, and H. Kusumaatmaja, “Bidirectional motion of droplets on gradient liquid infused surfaces”, *arXiv*, 2004.10408 (2020).
- [119] W. Wang, J. V. I. Timonen, A. Carlson, D.-M. Drotlef, C. T. Zhang, S. Kolle, A. Grinthal, T.-S. Wong, B. Hatton, S. H. Kang, S. Kennedy, J. Chi, R. T. Blough, M. Sitti, L. Mahadevan, and J. Aizenberg, “Multifunctional ferrofluid-infused surfaces with reconfigurable multiscale topography”, *Nature* **559**, 77–82 (2018).
- [120] F. Schellenberger, N. Encinas, D. Vollmer, and H.-J. Butt, “How Water Advances on Superhydrophobic Surfaces”, *Phys. Rev. Lett.* **116**, 096101 (2016).
- [121] C. Priest, R. Sedev, and J. Ralston, “Asymmetric Wetting Hysteresis on Chemical Defects”, *Phys. Rev. Lett.* **99**, 026103 (2007).
- [122] M. S. Sadullah, C. Semperebon, and H. Kusumaatmaja, “Drop Dynamics on Liquid-Infused Surfaces: The Role of the Lubricant Ridge”, *Langmuir* **34**, 8112–8118 (2018).
- [123] A. Fakhari and T. Lee, “Finite-Difference Lattice Boltzmann Method with A Block-Structured Adaptive-Mesh-Refinement Technique”, *Phys. Rev. E* **89**, 033310 (2014).
- [124] J. S. Wexler, I. Jacobi, and H. A. Stone, “Shear-Driven Failure of Liquid-Infused Surfaces”, *Phys. Rev. Lett.* **114**, 168301 (2015).
- [125] P. Baumli, H. Teisala, H. Bauer, D. Garcia-Gonzalez, V. Damle, F. Geyer, M. D’Acunzi, A. Kaltbeitzel, H.-J. Butt, and D. Vollmer, “Flow-Induced Long-Term Stable Slippery Surfaces”, *Adv. Sci.* **6**, 1900019 (2019).
- [126] S. Movafaghi, W. Wang, A. Metzger, D. D. Williams, J. D. Williams, and A. K. Kota, “Tunable superomniphobic surfaces for sorting droplets by surface tension”, *Lab Chip* **16**, 3204–3209 (2016).
- [127] X. Dai, N. Sun, S. O. Nielsen, B. B. Stogin, J. Wang, S. Yang, and T.-S. Wong, “Hydrophilic directional slippery rough surfaces for water harvesting”, *Sci. Adv.* **4** (2018).

- [128] J. Sun and P. B. Weisensee, “Microdroplet self-propulsion during dropwise condensation on lubricant-infused surfaces”, *Soft Matter* **15**, 4808–4817 (2019).
- [129] V. A. Lifton, “Microfluidics: an enabling screening technology for enhanced oil recovery (EOR)”, *Lab Chip* **16**, 1777–1796 (2016).
- [130] T. Yu, J. Zhou, and M. Doi, “Capillary imbibition in a square tube”, *Soft Matter* **14**, 9263–9270 (2018).
- [131] T. V. Vinay and S. N. Varanakkottu, “Separation of Floating Oil Drops Based on Drop-Liquid Substrate Interfacial Tension”, *Langmuir* **35**, 10596–10600 (2019).